# The Development and Applications of a Numerical Method for Compressible Vorticity Confinement in Vortex-Dominant Flows

Guangchu Hu

Dissertation submitted to the faculty of the
Virginia Polytechnic Institute and State University
in partial fulfillment of the requirements for the degree of

Doctor of Philosophy
in
Aerospace Engineering

Bernard Grossman, Chairman

John Steinhoff

Robert W. Walters

William H. Mason

William Devenport

June 2001
Blacksburg, Virginia

Keywords: Vorticity Confinement, CFD, Vortex-dominant flows

# The Development and Applications of a Numerical Method for Compressible Vorticity Confinement (CVC) in Vortex- Dominant Flows

by

Guangchu Hu

Committee Chairman: Bernard Grossman
Aerospace Engineering

## (ABSTRACT)

An accurate and efficient numerical method for Compressible Vorticity Confinement (CVC) was developed. The methodology follows from Steinhoff's vorticity confinement approach that was developed for incompressible flows. In this research, the extension of this approach to compressible flows has been developed by adding a vorticity confinement term as a "body force" into the governing compressible flow equations. This vorticity confinement term tends to cancel the numerical dissipative errors inherently related to the numerical discretization in regions of strong vorticity gradients.

The accuracy, reliability, efficiency and robustness of this method were investigated using two methods. One approach is directly applying the CVC method to several real engineering problems involving complex vortex structures and assessing the accuracy by comparison with existing experimental data and with other computational techniques. Examples considered include supersonic conical flows over delta wings, shock-bubble and shock-vortex interactions, the turbulent flow around a square cylinder and the turbulent flow past a surface-mounted 3D cube in a channel floor. A second approach for evaluating the effectiveness of the CVC method is by solving simplified "model problems" and comparing with exact solutions. Problems that we have considered are a two-dimensional supersonic shear layer, flow over a flat plate and a two-dimensional vortex moving in a uniform stream.

The effectiveness of the compressible confinement method for flows with shock waves and vortices was evaluated on several complex flow applications. The supersonic flow over a delta wing at high angle of attack produces a leeward vortex separated from the wing and cross flow, as well as bow shock waves.

The vorticity confinement solutions compare very favorably with experimental data and with other calculations performed on dense, locally refined grids. Other cases evaluated include isolated shock-bubble and shock-vortex interactions. The resulting complex, unsteady flow structures compare very favorably with experimental data and computations using higher-order methods and highly adaptive meshes.

Two cases involving massive flow separation were considered. First the two-dimensional flow over a square cylinder was considered. The CVC method was applied to this problem using the confinement term added to the inviscid formulation, but with the no-slip condition enforced. This produced an unsteady separated flow that agreed well with experimental data and existing LES and RANS calculations. The next case described is the flow over a cubic protuberance on the floor of a channel. This flow field has a very complex flow structure involving a horseshoe vortex, a primary separation vortex and secondary corner vortices. The computational flow structures and velocity profiles were in good agreement with time-averaged values of the experimental data and with LES simulations, even though the confinement approach utilized more than a factor of 50 fewer cells (about 20,000 compared to over 1 million).

In order to better understand the applicability and limitations of the vorticity confinement, particularly the compressible formulation, we have considered several simple model problems. Classical accuracy has been evaluated using a supersonic shear layer problem computed on several grids and over a range of values of confinement parameter. The flow over a flat plate was utilized to study how vorticity confinement can serve as a crude turbulent boundary layer model. Then we utilized numerical experiments with a single vortex in order to evaluate a number of consistency issues related to the numerical implementation of compressible confinement.

# Dedication

In Memoriam

Shengying Yang 1920-1984
Youcai Yang 1930-1998

In hope of their children and grandchildren will live in great happiness

To the most important people in my life:

my father, Sigao Hu,

and my wife, Xulian Yang

# Acknowledgements

The author is greatly indebted to Dr. Bernard Grossman for his guidance and financial support over the last four years. I have to thank Dr. John Steinhoff for his excellent ideas that inspired my thinking of the essential mechanisms of vorticity confinement. I appreciate Dr. Mason who always had a friendly attitude towards me when I asked questions; he taught me configuration aerodynamics and made me clearly understand the differences between the leading-edge separation of the traditional wings and delta wings. I would like to acknowledge the useful advice of Dr. Walters for accuracy analysis of vorticity confinement method despite his busy schedule. I have enjoyed interacting with Dr. Devenport whose cheerful attitude and good advice for the comparison of the present numerical solutions with analytical solutions deserves a lot of thanks.

I owe a lot to Dr. Yonghu Wenren from Flow Analysis Inc. for his help and many useful discussions about vorticity confinement. This work would not have been possible without the financial support from Flow Analysis Inc. over the last one and half years. I wish to acknowledge my good teacher Dr. Kyle Anderson from NASA Langley. He taught me CFD and gave me a lot of CFD knowledge. He always treated me like a friend and answered what I asked both in class and after class through emails. I have to thank Dr. Ribbens, Dr. Watson and Dr. Santos in the Computer Science Department at Virginia Tech for teaching me parallel algorithms and parallel implementations. I received many benefits from their courses.

I would like to thank my family for always supporting me through good and difficult times in the past years. My father Sigao Hu, my mother Shengying Yang and my brother Guangyi Hu constantly urged me on to study hard. My sisters Guangrong Hu and Shuhua Hu, my brother-in-law Zihe Cheng and Xinglen Qiao gave me a lot of financial support during difficult times. My wife Xulian Yang encouraged me to finish my Ph.D. despite the obstacles on my road. My 13 year old son Zongyang Hu helped me a lot by typing the draft and drawing a part of the plots for this dissertation; he always kept me smiling when I faced difficulties.

I have to thank my good friend *Dr. Philippe-Andre Tetrault* in Pratt & Whitney and my good friend *Mr. Hongman Kim* (hoping to be a Doctor soon) for their help and good discussions over the years. And big thanks go to *Ms. Foushee*, *Ms. Williams* and *Ms. Coe* in the AOE Department. Many thanks go to *Ms. Ghaderi* and *Mr. Brizee* in the Virginia Tech Writing Center. They read and corrected the first draft of this dissertation and gave me many tips of scientific writing. Without their help I would not have finished this dissertation.

# Contents

# List of Figures

# Chapter 1

# Introduction

In this chapter, the background of the present study will be stated, the difficulties will be described from the viewpoint of CFD and the significance will be noted in the design and analysis for fluid dynamics and aerodynamics. This will be followed with a prentation of the current status of CFD in complex vortex-dominant flows along with a discussion of the present proposed Compressible Vorticity Confinement (CVC) method. Finally, the organization of the dissertation will be given.

## 1.1 The Background of the Present Study

In the last three decades, CFD has been developed as a standard design and analysis tool in fluid dynamics and aerodynamics. CFD can shorten the time and lower the cost required to obtain aerodynamic flow simulations necessary for the design of new structures or aerospace vehicles. According to Paul E. Rubbert [1], Boeing completed upgrading its 737 family of airplanes in response to changing customer needs with the aid of fast, CFD-based design processes. It is well known that CFD can predict the behavior of attached flows, and as the speed and memory capability of the computer are increased, CFD researchers can perform flow simulations that are either impractical or impossible to obtain in wind tunnels or other ground based experimental test facilities. However, despite many recent advances, it is difficult for CFD researchers to simulate complex separated (vortex-dominant) flows, which may occur at high angles of attack or with bluff bodies. In those situations, the flows are turbulent, and may involve complicated multiple separations, shock-vortex interactions, vortex shedding, vortex-vortex interaction, vortex merging, impingement, reattachment, recirculation and bimodal behavior.

Figure 1.1 shows the flow patterns in an experiment [2] when a supersonic flow with free stream Mach number 1.7 passes a flat delta wing at angle of attack 13 degrees. Flow separation occurs at the leading

edges, resulting in large primary vortices on the lee-side with small viscous-induced secondary ones beneath them; cross-flow shocks are formed and interact with vortices to yield very complex vortical motions. Figure 1.2 presents a flow pattern formed by a flow over a 2D square cylinder at a high Reynolds number, according to the experiment done by Duaro *et al.* [3]. The separation occurs at the frontal corner with steep streamline curvature, forming recirculation behind the model and periodic vortex shedding. Figure 1.3 shows the flow patterns formed by a flow passing a surface-mounted cube in a plate channel according to the experiment done by Larousse, Martinuzzi and Tropea [4,5]. Line A in Figure1.3b corresponds to the primary separation caused by the strong adverse pressure gradient imposed by the cube in this region; the horseshoe vortex is clearly recognized in the velocity vector field shown in Figure 1.3c, which corresponds to the line B in Figure 1.3b. The bimodal behavior is shown in the region between the primary separation and the horseshoe vortex. In addition to the primary and secondary separation in front of the cube, the flow separates at the upper leading edge as well. Figure 1.3d shows two mean recirculation regions: one is over the top; the other is behind the cube. Two corner vortices are formed behind the cube on the floor of the channel and indicated in Figure1.3e. The overall flow pattern was sketched and shown in Figure1.3f [4,5].

Understanding the mechanism of complex vortex-dominant flows is of great importance for designing good and safe vehicles and structures. Many fighter aircraft incorporate a delta-wing lifting surface. When they fly at high angles of attack and supersonic speeds, the flow will be separated at the leading edge of the wings, leading to leading-edge vortices with inboard cross-flow shock waves. This flow environment may be unsteady and introduces many interesting nonlinear aerodynamic behaviors that may be beneficial or detrimental to the aircraft performance. A flow over a bluff body such as a building, a bridge, an automobile, etc., occasionally will produce periodic vortex shedding. Generally speaking, periodic vortex shedding will cause dynamic loading on the bodies, which, in extreme cases, may cause catastrophic failures.

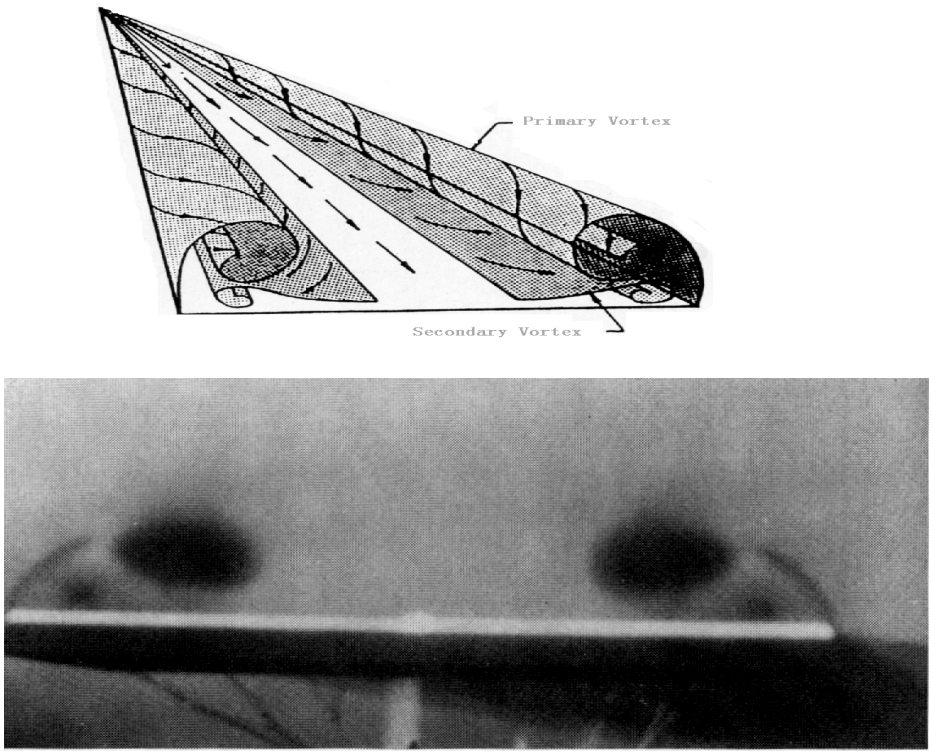


Figure 1.1: Flow pattern obtained in experiment by Miller and Wood [2].

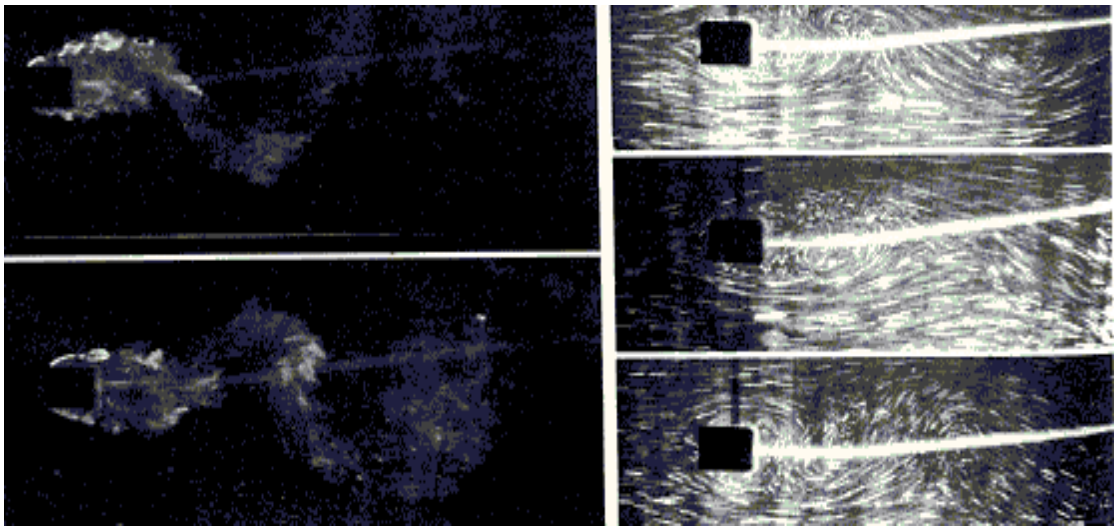

Figure 1.2: Periodic vortex shedding formed by a flow past a 2D square cylinder. The experiment was done by Duaro [3].

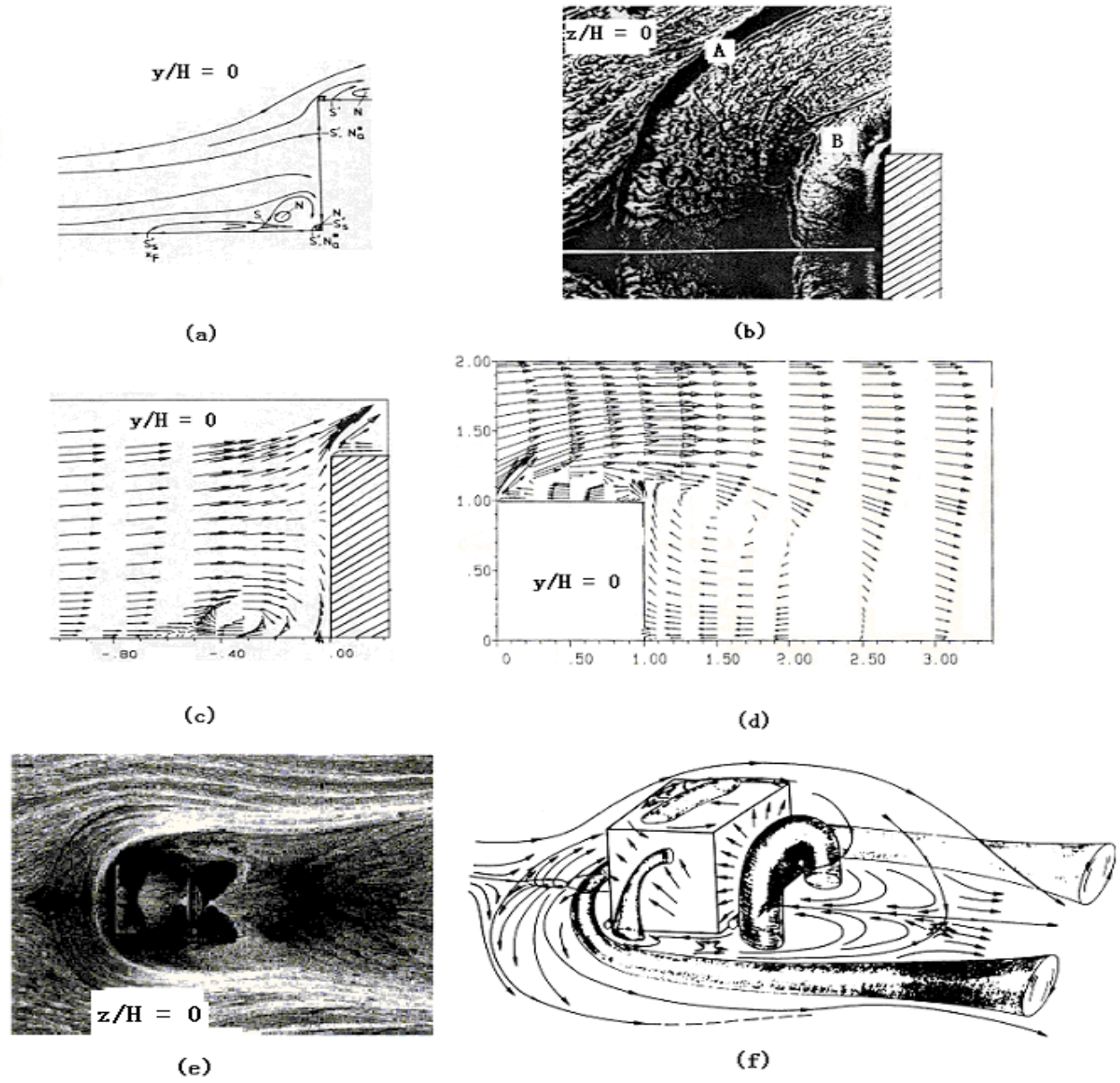


Figure 1.3: Flow past a surface-mounted cube in a plate channel. (a) Flow pattern for upstream of the cube on the symmetry plane; (b) oil visualization upstream of the cube on the floor of the channel; (c) measured time-averaged velocity vectors upstream of the cube on the symmetry plane; (d) measured time-averaged velocity vectors downstream of the cube on the symmetry plane; (e) oil visualization on the floor of the channel; (f) the overall sketch of the flow pattern.

Legend: S --- saddle; N --- node; ’ --- half saddle or node; * --- point viewed perpendicularly to the wall.

Subscripts: s --- separation; a --- attachment.

The experiment was done by Larousse, Martinuzzi and Tropea [4,5].

## 1.2 Current Status of CFD in Calculation of Complex Vortex-Dominant Flows

In general, vortex-dominant flows may be solved using two CFD approaches. One approach directly solves the Navier-Stokes (NS) equations plus the continuity equation without adding any model such as the Direct Numerical Simulation (DNS); the other approach solves Euler or NS equations plus the continuity equation with some models such as solving RANS equations with various turbulence models or LES models. The current status of CFD in the calculations of complex vortex-dominant flows can be summarized as follows:

**1.2.1 Solving Euler or NS Equations with the Continuity Equation Using Higher Order Discretization, a Fine Grid or an Adaptive Grid (Structured or Unstructured)**. Euler equations are used when viscous effects can be ignored; NS equations are used when viscous effects are considered. As we know, higher order discretization increases CPU loading, fine grid wastes memory storage, and adaptive procedures have a lot of complex logic controls. All these procedures are used for one objective, that is, to decrease the dissipation/dispersion errors inherently related to the numerical discretization.

Some example of complex discretization include a fifth order discretization of NS equations with a fine regular grids which was used to solve the problem involving vortices impinging on an airfoil by Rai *et al.* [6]. A steady vortex shed at the tip of a straight wing was studied by Strawn [7] using an unstructured adaptive grid. Interaction between a vortex and a propagating shock wave was calculated by Povitsky and Ofengeim with an adaptive unstructured scheme [8]. Yang *et al.* simulated the interaction between a moving shock wave with a circular light gas bubble in a channel with a finite width using a higher-order Flux-Corrected-Transport (FCT) scheme [9], but seemed not to get good agreement with the experiment [10]. Powell [11] embedded extra grid points in the vortical regions in the calculation of flows over plate delta wings, but still had difficulty in capturing the primary vortices without having them spread over a larger region than those measured in experiments. Furthermore, generally speaking, in current CFD methods, the calculated peak of the vorticity in the core region of the vortex is typically smaller than that measured in the experiment.

Shu [12] used fifth order finite difference WENO scheme to simulate a vortex periodically moving along one of the diagonals of a square domain with dimension of 10 units along with a uniform mesh of 80x80 points. In addition, the same problem was simulated using a second order finite difference MUSCL type TVD scheme. At time $t$ = 10, both schemes obtained good agreement with the "exact" solution; but at time $t$ = 100, the solution with the second order scheme shows too much dissipation in the core region of the vortex, the solution with the fifth order scheme still has good agreement with the "exact" solution. However, Shu reported in Ref. [12]: "the CPU time of a fifth order finite difference WENO scheme is roughly 3 to 8 times more than that of a second order TVD scheme (depending on the specific forms of the schemes and time discretization)".

**1.2.2 Solving RANS Equations with Various Turbulence Models Which Include Algebraic Models, One-Equation Models, Two-Equation Models and Second-Order Closure Models**. Until now there has been no universally acceptable turbulence model that can provide uniformly good results for engineering problems with separated flows. Algebraic models are simple to use, but are quite unreliable for separation flows because of the Boussinesq and "equilibrium" approximations implicit in these models. One-equation models have achieved closer agreement with experimental measurements for a limited number of separated flows than is possible with algebraic models, but the length scale for each new application needs to be specified. The $k-\varepsilon$ model is the most widely used in the family of two-equation models; unfortunately, it is inaccurate for flows with adverse pressure gradients, separation and recirculation. Sometimes modified $k-\varepsilon$ models yield better results for limited classes of problems, such as the Low-Reynold-Number modification, Two-Layer (TL) modification and Kato-Launder (KL) modification. Generally speaking, the Reynold-Stress-Model (RSM) predicts better results than the standard $k-\varepsilon$ model does, but it seems not to be promising when used in massively separated flows over bluff bodies. The $k-\omega$ model is very accurate for 2D boundary layers with variable pressure gradients (both adverse and favorable), but this model is very sensitive to the free stream boundary conditions for free shear flows. Rodi *et al.* [13-15] simulated the flows over a 2D square cylinder and a 3D surface-mounted cube in a channel by solving RANS with various turbulence models. They claimed that the standard $k-\varepsilon$ model completely failed to predict the flows over bluff bodies because it produced very large turbulent energy in the front stagnation regions and very large recirculation regions behind the bodies. The $k-\varepsilon$ model with KL modification $(KL-k-\varepsilon)$ and the wall function solved the problem with very large turbulent energy in the front stagnation regions, but still overestimated the length of the reverse flow regions. RSM with TL modification $(TL-RSM)$ predicted too short separation

zones behind the bodies. It appears that all two-equation models are inaccurate for the flows around surfaces with large curvatures, separations, sudden change in mean strain rate, rotation, vortex shedding, and 3D unsteady motions.

**1.2.3 Direct Numerical Simulation (DNS)**. Solves the exact time-dependent NS equations with the continuity equation under the assumption of no significant numerical and other form of errors. In principle, the grid must be fine enough to resolve the smallest eddies whose size is of the order of the Kolmogorov length scale, and the computational time step should be of the same order of the Kolmogorov time scale. Kim *et al.* [16] performed a DNS for a channel flow with Reynolds number 6,000 (based on H, the height of the channel) with grid points 2 and 4 million. The CPU time on Cray X/MP for the finer grid is 40 seconds per time step. 250 CPU hours was required in a run for a total time $t = 5H / u_\tau$, where $u_\tau$ is the friction velocity at the wall of the channel, $u_\tau = \sqrt{\tau_w / \rho}$. Speziale [17] noted that a DNS of turbulent pipe flow at Reynolds number 500,000 would require a computer 10 million times faster than a Cray Y/MP. In conclusion, there is a very long way to go for DNS to be a practical tool in the CFD community.

**1.2.4 Large Eddy Simulation (LES)**. Similar to DNS, solves the complete time-dependent NS equations with the continuity equation, but on a grid whose size is much larger than that used in DNS. The large-scale eddies whose size is larger than the order of grid size are resolved; the small eddies whose size is smaller than the order of grid size are filtered out and are modeled, usually using a Smagrorinsky or a Dynamic model. Rodi reported in Ref. [13] the LES calculations for a flow past a 2D square cylinder and a flow over a surface-mounted cube in a plate channel using CPU time 73 hours and 160 hours, respectively, on the SNI S600/20 vector computer. Although LES is more economical than DNS (typically, requiring 5-10 percent of the CPU time required for DNS), it still requires very large computer resources. Rodi reviewed the LES calculations for the flow past a 2D square cylinder and concluded in his paper [13]: "it was found that none of the LES results are uniformly good and entirely satisfactory and there were large differences between the individual calculations which are difficult to explain."

**1.2.5 Lagrangian Methods**. These methods treat flows with vortical motions by assigning vorticity or circulation to individual markers that are fixed in the flow field or convect with fluids. Leonard reviewed vortex methods with Lagrangian approaches for flow simulations in Ref. [18]. Methods that were

described included the point vortex method, the vortex blob method, and the contour dynamics method for two-dimensional flows, and the vortex filament method and its application to the aircraft-trailing vortices in three-dimensional flows. Furthermore, Leonard discussed the details of the vortex-in-cell methods in which the Lagrangian treatment of the vorticity field is retained, but the velocity field is solved on a fixed Eulerian mesh. As a result, the very high cost of the Biot - Savart integration is avoided when many vortex elements are used. In addition, "vortex lattice" or "vortex blob" techniques [19] and the "vortex embedding" technique [20] were employed to entail representation of vortex sheets or vortex filaments over surfaces or lines defined by markers in vortex dominated flows. Unfortunately, the Largrangian approach lacks the generality of being used to solve complex vortex–dominant flow problems, because in realistic engineering flows, vortex filaments may merge and reconnect, or boundary layers may abruptly separate, shedding a convecting vortex. Sometimes, multiple sheets may be shed from different places on the same surfaces and some may reattach. These complicated phenomena make the specification of markers very difficult.

## 1.3 Incompressible Vorticity Confinement (IVC)

IVC solves the incompressible Euler/NS equations plus the continuity equation with vorticity confinement terms to try to remove the numerical dissipation inherently related to the numerical discretization in vortical regions. For vortex dominated flows, because the vorticity confinement terms take care of the numerical dissipation errors, very simple schemes can be used to discretize the governing equations in order to save computing time. Vorticity confinement was proposed by Steinhoff and his coworkers in Refs.[21-24] for computing flows with concentrated vorticity. This method was originally applied to incompressible flows. Steinhoff and coworkers applied a velocity correction to the momentum conservation equations and solved the incompressible NS equations for two- and three-dimension vortex dominated flows [21,22]. The correction term is limited to the vortical regions and does not affect nonvortical regions. Similar to shock capturing techniques, vorticity confinement treats vortical layers without a detailed resolution of their internal structure. The confinement procedure is constructed in such a way that it preserves certain conservation laws outside and integrated over the vortical regions. This method can easily be incorporated into a standard Euler method on a fixed grid [23]. Applied to various flows involving a concentrated vorticity, the vorticity confinement approach has proved capable of treating thin vortical structures in complicated flows with massive separation using relatively coarse grids

[21-24]. Following the same anti-diffusive convection idea as in vorticity confinement, Steinhoff *et al.* [25] have developed a new confinement procedure for short acoustic pulses. A "Pressure Confinement" convects the pressure wave back towards the center of a propagating pulse and balances a numerical diffusion of a basic traditional solver.

## 1.4 Present Proposed Method for Compressible Vorticity Confinement (CVC) for Complex Vortex-Dominant Flows

CVC solves the exact time-dependent Euler equations with simple viscous boundary layer model equations (Euler/BC) plus the continuity equation with vorticity confinement terms as a "body force" on regular Cartesian grid. The governing equations are mass, momentum and energy conservation laws, so it can handle compressible phenomena like shock-vortex interactions in supersonic and hypersonic flows. IVC cannot do this because it solves incompressible Euler/BC equations with the continuity equation. This method is called Compressible Vorticity Confinement (CVC), because it is constructed from the compressible formulation. The viscosity effect is ignored in the rest of the dissertation, because most of the real engineering problems have very large Reynolds numbers; the extension to NS equations is straightforward. CVC can resolve the large-scale unsteady vortical motions like LES, but without considering viscosity effect and subgrid-scale model. The problem is considered in another way by adding the "body force" to try to remove the dissipation inherently related to numerical discretization in vortical regions, decreasing numerical errors in the solution procedure, so that the weak and small-scale vortical motions are not damped out by numerical dissipation. Furthermore, a very coarse grid can be used for 3D complicated turbulent flows with massive separations; so only very small CPU time is required compared to LES calculation. With the preliminary results of conical vortical flows on plate delta wings, interaction of a moving shock wave with a light gas bubble and a light gas circular vortex, flows past a 2D square cylinder and a 3D surface-mounted cube in a plate channel, we have almost achieved our objective. The dissertation will be organized as follows:

Chapter 2 describes the CVC method constructed by using conservation laws and finite-volume cell-centered discretization. Chapter 3 applies CVC to conical vortical flows over flat delta wings. We chose conical vortical flows over flat delta wings as one of our applications because leading-edge vortex flows in particular are of great interest to aerodynamicists. The lee-side vortices, when symmetry and stable, can

lead to beneficial high-lift situations; otherwise, they may lead to disaster. This kind of problem has a very simple geometry with a flat plate delta wing at angles of attack, but can lead to extremely intricate and intriguing flow topologies, producing a rich variety of leading-edge vortices and shock-vortex interaction patterns; moreover, these complicated flow situations cannot be adequately handled by current CFD methods.

Chapter 4 applies CVC to the interaction of a moving shock wave with a density inhomogeneity. We will investigate a two-dimensional moving shock wave over a circular light-gas inhomogeneity both in the form of a bubble and a circular vortex in a channel with a finite width. The pressure gradient formed by a moving shock wave interacts with the density gradient at the edge of the inhomogeneity to produce vorticity around the perimeter, and the structure rolls up into a pair of counter-rotating vortices. A practical application of the shock-induced vortices is the rapid and efficient mixing of fuel and oxidizer in a SCRAMJET combustion chamber.

Chapter 5 applies CVC to complex vortex-dominant flows over bluff bodies. We will study the flows over a 2D square cylinder and a 3D surface-mounted cube in a plate channel. We chose these applications to test CVC because the flows over bluff bodies involve impingement, multiple separations at different places, recirculations, bimodal behaviors, corner and arch vortices, periodic vortex shedding and 3D unsteady vortical motions. These flow phenomena are the most challenging in current CFD; no method can provide uniformly good results for these flows.

In Chapter 6, we present the parallel computing implementation for the calculation of the flow past a 3D surface-mounted cube and present the performance of this parallel calculation. Then in Chapter 7, we present the fundamental properties of CVC, which includes the accuracy analysis and limitation discussion for the CVC method. The dissertation ends with the summary and conclusions in Chapter 8.

# Chapter 2

# Formulation for Compressible Vorticity Confinement (CVC)

In this chapter we will first present the previous studies of vorticity confinement by Steinhoff and his coworkers in the last decade. This is followed by the formulation for the CVC method, and finally we will describe the numerical methods used in the present study.

## 2.1 Incompressible Vorticity Confinement (IVC)

The original vorticity confinement approach was designated for incompressible flows with thin concentrated vorticity structures by Steinhoff and his coworkers [21-24]. This method is somewhat similar to the shock capturing method. Thin vortical layers are treated without detailed resolution of their internal structure in a way similar to shock capturing algorithms in which a shock is captured in 2-3 grid cells without resolving the internal structure. The vorticity confinement term is built in such a way that conservation laws are preserved outside and integrated over the vortical regions; it is non-zero only within the vortical regions, and does not change the total vorticity or mass within those regions. This method can be easily incorporated with standard Euler / "Navier-Stokes" solvers (Euler with turbulence models) on a fixed grid. The core of the method is a velocity correction, applied locally, which prevents the vorticity from degrading during its propagation due to the numerical diffusion.

Numerical implementation of the vorticity confinement for an incompressible flow includes 3 main steps [26-28]:

1. Velocity convection based on momentum equations;

2. Velocity correction according to the vorticity confinement;
3. Solution of the pressure to mass conservation, as a conventional "split velocity" method [29].

Applied to incompressible flows, vorticity confinement has proven to be an efficient method. Some of the details of the basic method are presented in Refs. [21-24]. The method involves adding a term to the momentum equations. When these equations are discretized by finite difference methods, the modified equations include truncation error, so we actually solve the modified equations. For incompressible flow the original formulation of the vorticity confinement method of Steinhoff can be written as follows:

$$\nabla \cdot \vec{q} = 0\,, \tag{2.1}$$

$$\frac{\partial \vec{q}}{\partial t} = -(\vec{q} \cdot \nabla)\vec{q} - \nabla(p/\rho) + \mu \nabla^2 \vec{q} + \varepsilon \vec{k}\,, \tag{2.2}$$

where $\vec{q}$ is the velocity vector, $\rho$ is density, $p$ is pressure, and $\mu$ is a diffusion coefficient. In Steinhoff's formulation, the diffusion term is an artificial dissipation. The additional term $\varepsilon \vec{k}$ is a vorticity confinement term; $\varepsilon$ is a numerical coefficient that controls the size of the convecting vortical regions. The confinement term has the form:

$$\vec{k} = -\hat{n}_c \times \vec{\omega}\,, \tag{2.3}$$

$$\hat{n}_c = -\frac{\nabla(|\vec{\omega}|)}{|\nabla(|\vec{\omega}|)|}\,, \tag{2.4}$$

$$\vec{\omega} = \nabla \times \vec{q}\,, \tag{2.5}$$

where $\hat{n}_c$ is a unit vector pointing away from the centroid of the vortical region and the term $\varepsilon \vec{k}$ serves to convect $\vec{\omega}$ back towards the centroid as it diffuses away. This term is added to correct the diffusive error in the momentum equations. A non-diffusive solution will be obtained when the vorticity confinement and the numerical diffusion become balanced. Under this circumstance, the vorticity confinement conserves momentum.

## 2.2 The Formulation for Compressible Vorticity Confinement (CVC)

Vorticity confinement has been proved to be an efficient method in conjunction with finite difference schemes as a basic solver in incompressible flow. However, attempting to extend ICV to compressible flows turns out to be not straightforward. A partial explanation of this could be that vorticity confinement acts only on the velocity field and implicitly balances the diffusive error only in momentum equations. At the same time, the velocity correction term works as an unbalanced source for the energy equation and mass continuity equation for compressible flows. Traditional compressible solvers do not include a mass/energy conservation step similar to the one in the "split-velocity" method used in incompressible flows. As a result, there is no steady-state solution for the modified system of equations. For the time-dependent problems, this error is practically negligible for low subsonic flow. But if we extend this method directly to transonic and supersonic vortex-dominant flows, this error for time-dependent problem will be large, and cannot be neglected, so we need a more consistent way to construct vorticity confinement for compressible flows.

There have been several attempts to extend the vorticity confinement to compressible flows. Pevchin [30] *et al.* developed a very complicated formulation based on flux splitting which was dependent upon the grid orientation. Yee and Lee [31] attempted to use the incompressible vorticity confinement term directly in the compressible momentum equations, and that produced an inconsistent formulation. In the present work, we added the confinement term in a consistent way within a conservation law framework. We have noted that the confinement term added to momentum equations in Steinhoff's formulation may be interpreted as a "body force". We can then extend the approach to compressible conservation laws by adding this "body force" to the integral momentum equations and rate of work done by the "body force" to energy conservation law. This eliminates the inconsistencies due to directly extending the original vorticity confinement just in momentum equations in incompressible flow to compressible flow; a non-diffusion solution can be achieved even for time-dependent supersonic problems. A finite-volume scheme with CVC then can be developed directly.

The integral conservation laws for mass, momentum and energy may be written for a control volume fixed in space as follows:

$$\frac{d}{dt}\iiint_V \rho d\tau + \iint_S \rho \vec{V}\cdot\hat{n}_s d\sigma = 0\,, \tag{2.6}$$

$$\frac{d}{dt}\iiint_V \rho \vec{V} d\tau + \iint_S \rho \vec{V}(\vec{V}\cdot\hat{n}_s) d\sigma = -\iint_S p\hat{n}_s d\sigma + \iiint_V \rho \vec{f}_b d\tau\,, \tag{2.7}$$

$$\frac{d}{dt}\iiint_V \rho e_O d\tau + \iint_S \rho e_O \vec{V}\cdot\hat{n}_s d\sigma = -\iint_S p\vec{V}\cdot\hat{n}_s d\sigma + \iiint_V \rho \vec{V}\cdot\vec{f}_b d\tau\,, \tag{2.8}$$

where $\vec{f}_b$ is a "body force" per unit mass (acceleration), which serves to try to balance the numerical diffusion inherently related to numerical discretization and conserve momentum in vortical regions. We have presented the form of the equations for inviscid flows here, but the extension to viscous flows is straightforward.

Now, we define the "body force" term $\vec{f}_b$ as follows:

$$\vec{f}_b = -E_c \hat{n}_c \times \vec{\omega}\,, \tag{2.9}$$

where $\hat{n}_c$ has the definition in Eq. (2.4), and $\vec{\omega}$ is the vorticity vector defined in Eq. (2.5). $E_c$ is a positive vorticity confinement parameter. Eqs. (2.6)-(2.8) are used directly to develop a finite-volume scheme. After manipulating Eqs. (2.6)-(2.8) by using Gauss's divergence theorem, we can rewrite Eqs. (2.6)-(2.8) in Cartesian coordinates as follows:

$$\frac{\partial Q}{\partial t} + \frac{\partial F}{\partial x} + \frac{\partial G}{\partial y} + \frac{\partial H}{\partial z} = S\ , \tag{2.10}$$

where

$$Q = \begin{pmatrix} \rho \\ \rho u \\ \rho v \\ \rho w \\ \rho e_O \end{pmatrix}, F = \begin{pmatrix} \rho u \\ \rho u^2 + p \\ \rho uv \\ \rho uw \\ \rho uh_0 \end{pmatrix}, G = \begin{pmatrix} \rho v \\ \rho vu \\ \rho v^2 + p \\ \rho vw \\ \rho vh_0 \end{pmatrix}, H = \begin{pmatrix} \rho w \\ \rho uw \\ \rho vw \\ \rho w^2 + p \\ \rho wh_0 \end{pmatrix}, \tag{2.11}$$

where e $_0$ is the total energy in unit mass, $h_0$ is the stagnation enthalpy, p is the pressure, S is the vorticity confinement term. They are defined as follows:

$$\left.\begin{aligned} h_0 &= e_0 + p/\rho, \\ p &= (\gamma-1)\rho[e_0 - (u^2+v^2+w^2)/2], \\ S &= \begin{pmatrix} 0 \\ \rho\vec{f}_b \cdot \hat{i} \\ \rho\vec{f}_b \cdot \hat{j} \\ \rho\vec{f}_b \cdot \hat{k} \\ \rho\vec{f}_b \cdot \vec{V} \end{pmatrix}, \end{aligned}\right\} \tag{2.12}$$

where $\rho$ is density, $p$ is pressure, (u, v, w) is the velocity component in (x, y, z) direction respectively, and $(\hat{i}, \hat{j}, \hat{k})$ is the unit vector in (x, y, z) direction respectively. For convenience, let's define a scalar variable $\phi$ as the magnitude of the vorticity vector $\vec{\omega}$ as follows:

$$\phi = |\vec{\omega}| = \sqrt{\omega_x^2 + \omega_y^2 + \omega_z^2}\ . \tag{2.13}$$

So, in Cartesian coordinates

$$\hat{n}_c = -\frac{\nabla\phi}{|\nabla\phi|} = \phi_{xs}\hat{i} + \phi_{ys}\hat{j} + \phi_{zs}\hat{k}, \tag{2.14}$$

where

$$\left.\begin{aligned} \phi_{xs} &= \frac{\phi_x}{\sqrt{\phi_x^2 + \phi_y^2 + \phi_z^2}}, \\ \phi_{ys} &= \frac{\phi_y}{\sqrt{\phi_x^2 + \phi_y^2 + \phi_z^2}}, \\ \phi_{zs} &= \frac{\phi_z}{\sqrt{\phi_x^2 + \phi_y^2 + \phi_z^2}}. \end{aligned}\right\} \tag{2.15}$$

Now we get the expression of $\vec{f}_b$

$$\vec{f}_b = -E_c \hat{n}_c \times \vec{\omega} = -E_c \begin{pmatrix} \hat{i} & \hat{j} & \hat{k} \\ \phi_{xs} & \phi_{ys} & \phi_{zs} \\ \omega_x & \omega_y & \omega_z \end{pmatrix} = f_{bx}\hat{i} + f_{by}\hat{j} + f_{bz}\hat{k}, \tag{2.16}$$

where

$$\left.\begin{aligned} f_{bx} &= -E_c(\omega_z \phi_{ys} - \omega_y \phi_{zs}), \\ f_{by} &= -E_c(\omega_x \phi_{zs} - \omega_z \phi_{xs}), \\ f_{bz} &= -E_c(\omega_y \phi_{xs} - \omega_x \phi_{ys}), \end{aligned}\right\} \tag{2.17}$$

and

$$\left.\begin{aligned} \omega_x &= \frac{\partial w}{\partial y} - \frac{\partial v}{\partial z}, \\ \omega_y &= \frac{\partial u}{\partial z} - \frac{\partial w}{\partial x}, \\ \omega_z &= \frac{\partial v}{\partial x} - \frac{\partial u}{\partial y}. \end{aligned}\right\} \tag{2.18}$$

Finally, the vorticity confinement term in a compressible flow can be expressed as follows:

$$S = \begin{pmatrix} 0 \\ \rho f_{bx} \\ \rho f_{by} \\ \rho f_{bz} \\ \rho(u f_{bx} + v f_{by} + w f_{bz}) \end{pmatrix} = \begin{pmatrix} 0 \\ -\rho E_c(\omega_z \phi_{ys} - \omega_y \phi_{zs}) \\ -\rho E_c(\omega_x \phi_{zs} - \omega_z \phi_{xs}) \\ -\rho E_c(\omega_y \phi_{xs} - \omega_x \phi_{ys}) \\ -\rho E_c[u(\omega_z \phi_{ys} - \omega_y \phi_{zs}) + v(\omega_x \phi_{zs} - \omega_z \phi_{xs}) + w(\omega_y \phi_{xs} - \omega_x \phi_{ys})] \end{pmatrix}. \tag{2.19}$$

Setting $w = 0, \omega_x = \omega_y = 0, f_{bz} = 0, H = 0$ in Eqs. (2.10)-(2.13) and Eq. (2.19) and removing the fourth equation in Eq.(2.19), we obtain the formulation for two-dimensional flows.

## 2.3 Numerical Formulation

Using a finite volume, explicit multi-stage Runge-Kutta time integration scheme we discretize Eq.(2-10) as follows:

$$Q^{(l)} = Q^{(0)} + \alpha_l \Delta t R(Q^{(l-1)}) . \tag{2.20}$$

A two-stage Runge-Kutta time-stepping scheme is obtained by setting coefficient $\alpha_1 = 1/2$ and $\alpha_2 = 1.0$ ; A three-stage Runge-Kutta time-stepping scheme is obtained by setting coefficient $\alpha_1 = 1/3, \alpha_2 = 1/2$ and $\alpha_3 = 1.0$ ; a four-stage Runge-Kutta time-stepping scheme is obtained by setting the coefficient $\alpha_1 = 1/4, \alpha_2 = 1/3, \alpha_3 = 1/2$ and $\alpha_4 = 1.0$ . The residual is defined as follows:

$$R(Q^{(l-1)}) = S(Q^{(l-1)}) - \frac{1}{\Delta V} \sum_{k=1}^{N} \hat{F}_k (Q^{(l-1)}) \Delta A_k , \tag{2.21}$$

where $\Delta V$ is the grid cell volume, $\hat{F}_k$ is the flux on cell side k, $\Delta A_k$ is the surface area of cell side k, and $\hat{F}_k$ is defined as follows:

$$\hat{F}_k = \hat{n}_x F + \hat{n}_y G + \hat{n}_z H , \tag{2.22}$$

where F, G and H are defined in Eq. (2.11) and $(\hat{n}_x, \hat{n}_y, \hat{n}_z)$ are the three components of the unit normal vector perpendicular to the surface of the cell side k. A fourth-order difference and a second-order difference based artificial dissipation are added to the central-difference scheme to suppress odd-even decoupling oscillations in the steep gradient regions. The artificial viscosity models under the consideration will be discussed in the next section.

## 2.4 Artificial Dissipation Models

### 2.4.1 Scalar Dissipation Model (SDM) with Second-order and Fourth-order Difference

The basic dissipation model employed in the present work is a non-isotropic model in which the dissipative terms are functions of the spectral radii of the Jacobian matrices associated with the appropriate coordinate directions [32]. For clarity, a detailed description of modified convective numerical flux at typical cell face $(i+1/2, j, k)$ can be expressed as follows:

$$\hat{F}_{i+1/2,j,k} = \frac{1}{2}(\hat{F}_{i,j,k} + \hat{F}_{i+1,j,k}) - D_{i+1/2,j,k}, \tag{2.23}$$

where term $D_{i+1/2,j,k}$ represents the dissipative term for index $i$. Here for simplicity, the dissipation terms for index *j* and *k* are ignored, because they can be treated in the same way as that for index *i*.

The dissipation term $D_{i+1/2,j,k}$ can be written as follows:

$$D_{i+1/2,j,k} = \lambda_{i+1/2,j,k}[\varepsilon^{(2)}_{i+1/2,j,k}(Q_{i+1,j,k} - Q_{i,j,k}) - \varepsilon^{(4)}_{i+1/2,j,k}(Q_{i+2,j,k} - 3Q_{i+1,j,k} + 3Q_{i,j,k} - Q_{i-1,j,k})], \tag{2.24}$$

where $\lambda_{i+1/2.j,k}$ is the spectral radius of the flux Jacobian matrix $\hat{A} \equiv \frac{\partial \hat{F}}{\partial Q}$; $\varepsilon^{(2)}$, $\varepsilon^{(4)}$ and $\lambda_{i+1/2,j,k}$ can be written as follows:

$$\varepsilon^{(2)}_{i+1/2,j,k} = k^{(2)} \max(\gamma_{i+1,}\gamma_i), \tag{2.25}$$

$$\varepsilon^{(4)}_{i+1/2,j,k} = \max(0, k^{(4)} - \varepsilon^{(2)}_{i+1/2,j,k}), \tag{2.26}$$

$$\left.\begin{aligned} \lambda_{i+1/2,j,k} &= \left|\hat{V}\right| + c, \\ \left|\hat{V}\right| &= \hat{n}_x u + \hat{n}_y v + \hat{n}_z w, \end{aligned}\right\} \tag{2.27}$$

where $k^{(2)}$ and $k^{(4)}$ are small positive numbers which vary case by case, and $\gamma_i$ is given by:

$$\gamma_i = \frac{\left|p_{i+1,j,k} - p_{i,j,k}\right| - \left|p_{i,j,k} - p_{i-1.j.k}\right|}{\left|p_{i+1,j,k} - p_{i,j,k}\right| + \left|p_{i,j,k} - p_{i-1.j.k}\right| + \varepsilon}, \tag{2.28}$$

where $p$ is the pressure, and $\varepsilon$ is a very small positive number to be used to avoid zero denominators in the smooth region.

### 2.4.2 Matrix Dissipation Model (MDM $^{(1)}$) with Second-order and Fourth-order Differences

The dissipation model just described in 2.4.1 is not optimal in the sense that the same dissipation scaling is used for all the governing equations. The reduced artificial dissipation can be obtained by individually scaling the dissipation contribution to each equation [33-36], as is done implicitly in upwind schemes. This can be implemented by replacing the scalar coefficients used in the scalar artificial dissipation model by the modulus (absolute values) of flux Jacobian matrices, then $\lambda_{i+1/2,j,k}$ in Eq. (2.24) is replaced by $\left|\hat{A}\right|$.

The matrix $\hat{A}$ can be rewritten as follows:

$$\hat{A} = R^{-1}\Lambda R, \tag{2.29}$$

where $\Lambda$ is a diagonal matrix with the eigenvalues of $\hat{A}$ as its entries, $R$ is a matrix composed of the eigenvectors of $\hat{A}$, then $\left|\hat{A}\right|$ can be defined as follows:

$$\left|\hat{A}\right| = R^{-1}\left|\Lambda\right|R, \tag{2.30}$$

where $\left|\Lambda\right| = diag[\left|\lambda_1\right|,\left|\lambda_1\right|,\left|\lambda_1\right|,\left|\lambda_2\right|,\left|\lambda_3\right|]$ and $\lambda_1 = \hat{V}, \lambda_2 = \hat{V} + c, \lambda_3 = \hat{V} - c$. Here, c is the local speed of sound. Eq. (2.24) can be rewritten as follows:

$$D_{i+1/2,j,k} = \left|\hat{A}\right| \cdot d \,, \tag{2.31}$$

and

$$d = \varepsilon^{(2)}_{i+1/2,j,k}(Q_{i+1,j,k} - Q_{i,j,k}) - \varepsilon^{(4)}_{i+1/2,j,k}(Q_{i+2,j,k} - 3Q_{i+1,j,k} + 3Q_{i,j,k} - Q_{i-1,j,k}) \,. \tag{2.32}$$

Here, $d$ contains five components $d_1, d_2, d_3, d_4, d_5$. After some manipulation of matrix multiplication (see Appendix A), we have the expression of the matrix dissipation model as follows:

$$D_{i+1/2,j,k} = |\lambda_1| d + \frac{(|\lambda_2| - |\lambda_1|)}{2} l_1 \begin{pmatrix} 1 \\ \frac{u}{c} + \hat{n}_x \\ \frac{v}{c} + \hat{n}_y \\ \frac{w}{c} + \hat{n}_z \\ \frac{h_0}{c} + \hat{V} \end{pmatrix} + \frac{(|\lambda_3| - |\lambda_1|)}{2} l_2 \begin{pmatrix} 1 \\ \frac{u}{c} - \hat{n}_x \\ \frac{v}{c} - \hat{n}_y \\ \frac{w}{c} - \hat{n}_z \\ \frac{h_0}{c} - \hat{V} \end{pmatrix}, \tag{2.33}$$

and

$$h_0 = q^2 + \frac{c^2}{\gamma - 1}, \tag{2.34}$$

$$q^2 = \frac{u^2 + v^2 + w^2}{2}, \tag{2.35}$$

$$\hat{V} = \hat{n}_x u + \hat{n}_y v + \hat{n}_z w, \tag{2.36}$$

$$l_1 = (\frac{\gamma - 1}{c} q^2 - \hat{V}) d_1 + (-\frac{\gamma - 1}{c} u + \hat{n}_x) d_2 + (-\frac{\gamma - 1}{c} v + \hat{n}_y) d_3 + (-\frac{\gamma - 1}{c} w + \hat{n}_z) d_4 + \frac{\gamma - 1}{c} d_5, \tag{2.37}$$

$$l_2 = (\frac{\gamma-1}{c}q^2 + \hat{V})d_1 + (-\frac{\gamma-1}{c}u - \hat{n}_x)d_2 + (-\frac{\gamma-1}{c}v - \hat{n}_y)d_3 + (-\frac{\gamma-1}{c}w - \hat{n}_z)d_4 + \frac{\gamma-1}{c}d_5, \tag{2.38}$$

where $(\hat{n}_x, \hat{n}_y, \hat{n}_z)$ is the unit normal vector at a cell face. The formulation for 2-D problems can be obtained setting $w = 0$ and removing the fourth component in $D_{i+1/2,j,k}$. There is no matrix-vector and vector-vector multiplication in the present formulation. This simplifies the matrix dissipation model suggested by Turkel *et al.* [33-36], yet gives more efficient computation than that given by Turkel *et al.*

In practical calculation, we cannot choose $\lambda_1 = \hat{V}, \lambda_2 = \hat{V} + c, \lambda_3 = \hat{V} - c$ in Eq. (2-32), because $\lambda_1$ approaches to zero near stagnation points, $\lambda_2$ and $\lambda_3$ go to zero near sonic points. At these points, the artificial viscosity will be zero, creating numerical difficulties for the calculation. By limiting these values using the following procedure, the difficulties will be eliminated.

$$\left.\begin{aligned} |\lambda_1| &= \max(|\lambda_1|, v_l\lambda_{i+1/2,j,k}), \\ |\lambda_2| &= \max(|\lambda_2|, v_n\lambda_{i+1/2,j,k}), \\ |\lambda_3| &= \max(|\lambda_3|, v_n\lambda_{i+1/2,j,k}), \end{aligned}\right\} \tag{2.39}$$

where $v_n$ limits the eigenvalues associated with the nonlinear characteristic fields to a minimum value that is a fraction of the spectral radius and $v_l$ limits the eigenvalues associated with linear characteristic field. The values for the limiting coefficients $v_n$ and $v_l$ are determined through numerical experiment so that sharper shocks and suction peaks are captured without introducing spurious oscillations in the calculation and still maintaining good convergence properties. For steady-state problems, firstly the values of $k^{(2)}, k^{(4)}$ and $v_n, v_l$ are set to larger values to get faster convergence, after the solution gets convergent, the values of $k^{(2)}, k^{(4)}$ and $v_n, v_l$ are set to smaller values to get sharper shocks and discontinuities. Also, a more accurate solution can be obtained. It should be noted that by setting $v_l = 1, v_n = 1$ we recover the scalar form of the artificial dissipation, whereas setting $v_l = 0, v_n = 0$ corresponds to the use of actual eigenvalues without any limiters. This method has good performance for transonic flows. However, the boundary condition handling procedure has a small difficulty. Section 2.4.4 will be devoted to the boundary handling procedure.

### 2.4.3 Matrix Dissipation Model (MDM $^{(2)}$) with Second-order Difference and Linear or Parabolic Interpolation for Primitive Variables

MDM $^{(2)}$ is very similar to MDM $^{(1)}$. The numerical flux at cell face is constructed by the following way:

$$\hat{F}_{i+1/2,j,k} = \frac{1}{2}(\hat{F}(Q^L) + \hat{F}(Q^R)) - E_d (R^{-1}|\Lambda|R)_{i+1/2,j,k}(Q^R - Q^L), \tag{2.40}$$

where $E_d$ is the dissipation coefficient, the standard value is 0.5, but it can be adjustable. The definitions of $R, \Lambda, R^{-1}$ are the same as MDM $^{(1)}$, but the values of primitive variables $(\rho, u, v, w, p)$ at cell faces are obtained using linear or parabolic interpolation of the values at cell centers because the cell-centered finite volume scheme is used in the present study. This method is more convenient to handle the boundary conditions than MDM $^{(1)}$, because we can use the same order interpolation as inner points for boundary points by using the inner points on one side of the corresponding boundary. So the calculation at boundary points is consistent with the calculation of the inner points, resulting in the over all good performance for the whole domain. In addition to this advantage, this method can obtain higher accuracy by using parabola or higher order interpolations for primitive variables. Furthermore, in a practical calculation, a limiter must be used to prevent numerical oscillation. In the present study, the following limiter is chosen:

$$\frac{4\Delta\nabla + \varepsilon}{3(\Delta - \nabla)^2 + 4\Delta\nabla + \varepsilon}, \Delta = f_{i+1} - f_i, \nabla = f_i - f_{i-1}, \tag{2.41}$$

where $\varepsilon$ is a very small positive parameter to use to avoid a zero denominator in smooth region, $f$ is a any primitive variable, $i$ is the index of a grid cell in one of the coordinates.

## 2.4.4 Boundary Conditions for MDM [(1)]

This section is devoted to the boundary handling procedure for MDM [(1)]. Near the far-field and downstream boundaries, information on the flow variables at the "ghost" cells that surround these boundaries is used to construct the dissipation term. Near the solid boundaries, the linearly distributed flow variables are implied in forming the derivatives needed for the dissipation term, which results in zero dissipative flux at the solid boundaries at $j = 3/2$. The grid stencil near the solid wall is presented in Figure 2.1. In our dissipation model, the fourth-difference is included. The standard five-point difference stencil must be replaced at the first two interior mesh cells.

Let $d_j$ denote the actual dissipation for a mesh cell $j = 2,3$ in the direction represented by index j and assume $\lambda^{(2)}\varepsilon^{(2)} = \lambda^{(4)}\varepsilon^{(4)} = 1.0$, we have

$$\left.\begin{aligned} D_2 &= D_{5/2} - D_{3/2} = D_{5/2} = D_{5/2}^{(2)} + D_{5/2}^{(4)}, \\ D_3 &= D_{7/2} - D_{5/2} = (D_{7/2}^{(2)} - D_{5/2}^{(2)}) + (D_{7/2}^{(4)} - D_{5/2}^{(4)}), \\ D_{5/2}^{(2)} &= Q_3 - Q_2, \\ D_{7/2}^{(2)} &= Q_4 - Q_3. \end{aligned}\right\} \tag{2.42}$$

The second-order dissipation term is calculated straightforward, by setting $D_{3/2}$ equal zero. This implies that the dissipation terms do not impair the no-flux boundary condition imposed at $j = 3/2$. When the solution at cell $j = 2$ is processed, the dissipation at interface $j = 5/2$ is only considered.

$$\left.\begin{aligned} D_{5/2}^{(4)} &= -\Delta Q_{7/2} + 2\Delta Q_{5/2} - \Delta Q_{3/2}, \\ D_{7/2}^{(4)} &= -\Delta Q_{9/2} + 2\Delta Q_{7/2} - \Delta Q_{5/2}. \end{aligned}\right\} \tag{2.43}$$

The calculation for $D_{7/2}$ is straightforward, whereas the calculation for $D_{5/2}^{(4)}$ has a little trouble because $\Delta Q_{3/2}$ is unknown, but from linearly distributed variables we have

$$\Delta Q_{3/2} = \Delta Q_{5/2}. \tag{2.44}$$

Now we have

$$D_{5/2}^{(4)} = -\Delta Q_{7/2} + \Delta Q_{5/2}. \tag{2.45}$$

From the discussion above, no "ghost" point at the solid boundary is needed, so the "ghost" point $j = 1$ can be removed from our calculated domain.

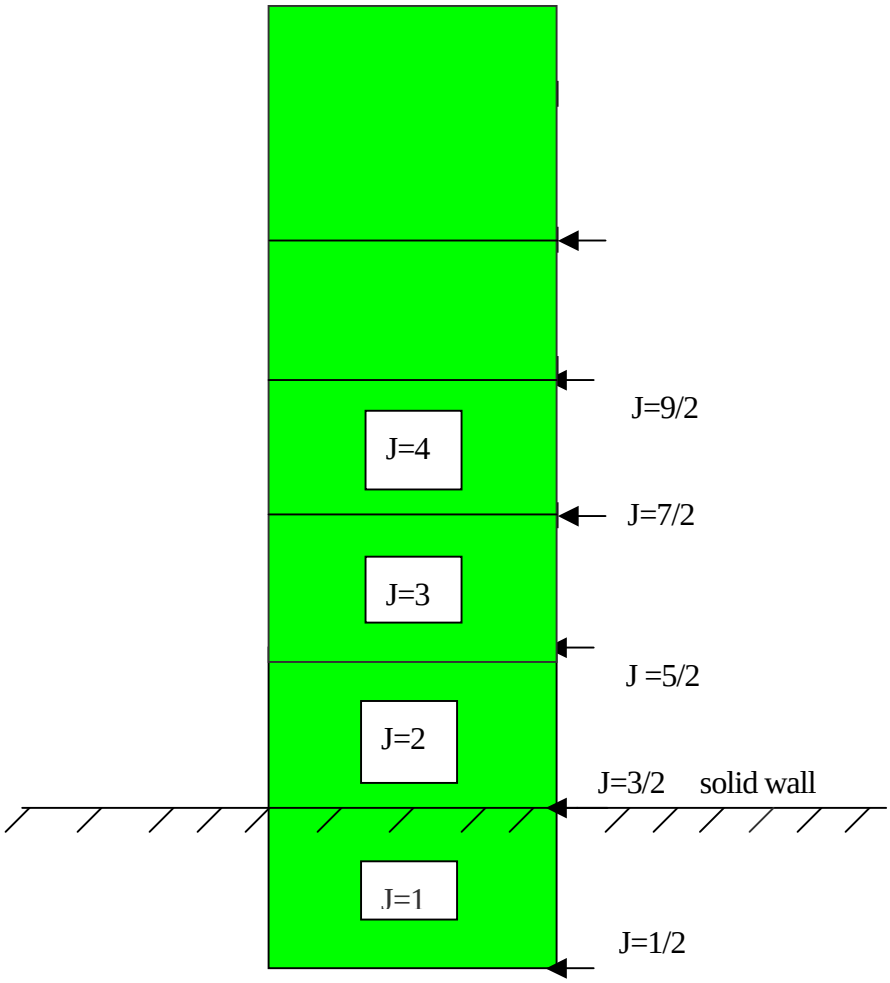


Figure 2.1: The grid stencil near the solid wall.

The physical boundary condition at the solid wall is enforced by no penetration condition with

$$\hat{V} = \hat{n}_x u + \hat{n}_y v + \hat{n}_z w = 0 . \tag{2.46}$$

The only contribution to the numerical flux at the solid wall is the pressure *p*, so the numerical flux at the solid wall can be written as follows:

$$\hat{F}_{3/2} = \begin{pmatrix} \int \rho \hat{V} d\sigma \\ \int [\rho u \hat{V} + \hat{n}_x p] d\sigma \\ \int [\rho v \hat{V} + \hat{n}_y p] d\sigma \\ \int [\rho w \hat{V} + \hat{n}_z p] d\sigma \\ \int \rho h_0 \hat{V} d\sigma \end{pmatrix} = \begin{pmatrix} 0 \\ \int \hat{n}_x p d\sigma \\ \int \hat{n}_y p d\sigma \\ \int \hat{n}_z p d\sigma \\ 0 \end{pmatrix} . \tag{2.47}$$

## 2.5 Matrix Compressible Vorticity Confinement Model (MCVC)

According to Turkel *et al.* [33-36], the matrix dissipation model works better than the scalar dissipation model. There is a counterpart of matrix dissipation model for CVC, which is called Matrix Compressible Vorticity Confinement (MCVC). Matrix confinement scales the scalar confinement according to the egenvalues of the flux Jacobians $\frac{\partial \hat{F}}{\partial Q}, \frac{\partial \hat{G}}{\partial Q}$ and $\frac{\partial \hat{H}}{\partial Q}$. We take

$$S = \hat{S}_x + \hat{S}_y + \hat{S}_z \tag{2.48}$$

with

$$\hat{S}_x = \left|\hat{A}\right| \begin{pmatrix} 0 \\ -E_c^{'}\rho(\hat{n}_c \times \vec{\omega}).\hat{i} \\ 0 \\ 0 \\ -E_c^{'}\rho(\hat{n}_c \times \vec{\omega}).u\hat{i} \end{pmatrix}, \tag{2-49}$$

and

$$\hat{S}_y = \left|\hat{B}\right| \begin{pmatrix} 0 \\ 0 \\ -E_c^{'}\rho(\hat{n}_c \times \vec{\omega}).\hat{j} \\ 0 \\ -E_c^{'}\rho(\hat{n}_c \times \vec{\omega}).v\hat{j} \end{pmatrix}, \tag{2.50}$$

$$\hat{S}_z = \left|\hat{C}\right| \begin{pmatrix} 0 \\ 0 \\ 0 \\ -E_c^{'}\rho(\hat{n}_c \times \vec{\omega}).\hat{k} \\ -E_c^{'}\rho(\hat{n}_c \times \vec{\omega}).w\hat{k} \end{pmatrix}, \tag{2.51}$$

where $\hat{A} \equiv \frac{\partial \hat{F}}{\partial Q}, \hat{B} \equiv \frac{\partial \hat{G}}{\partial Q}$ and $\hat{C} \equiv \frac{\partial \hat{H}}{\partial Q}$, $\hat{n}_c$ is defined in Eq. ( 2.4) and $\vec{\omega}$ is defined in Eq. ( 2.5), and $E_c^{'}$ is the confinement parameter for MCVC. The detailed formulation of matrix-vector multiplication is defined in Eqs. (2.33-2.39). However, they are evaluated at the cell center instead of at cell faces because S is the source term, and the eigenvalues are replaced by

$$\left.\begin{array}{l} \lambda_1 = \tilde{U}, \lambda_2 = \tilde{U} + c\sqrt{n_x^2 + n_y^2 + n_z^2}, \lambda_3 = \tilde{U} - c\sqrt{n_x^2 + n_y^2 + n_z^2} \\ U = n_x u + n_y v + n_z w \end{array}\right\}, \tag{2.52}$$

where $(n_x, n_y, n_y)$ is the averaged of the normal vectors at the two cell faces across a same coordinate . Therefore, matrix confinement implicitly contains the grid size as a scaling factor. This is because numerical discretization errors are related to the grid size and the confinement is constructed to try to

cancel the numerical disretization errors in vortical regions. Therefore, the confinement term should be related to the grid size, and the grid size is a reasonable scaling factor.

## 2.6 The Choice of the Values of the Free Parameters

In the present study, the dissipation parameters $k^{(2)}, k^{(4)}$ and $E_d$, and the confinement parameter $E_c$ or $E_c^{'}$ all are free parameters, which are chosen by the researcher. Generally speaking, the values of $k^{(2)}$ and $k^{(4)}$ are in the range of 0.01-0.5, and the typical value for $E_d$ is in the range of 0.1-0.6. They are chosen in such a way the numerical solution is stable. In my opinion, standard values do not exist for all problems; the researcher should try different values for the same problem and choose the smallest one which achieves stability. In addition, the value of the confinement parameter must be chosen by the experience of the researcher and it depends on the problem solved. By my experience, generally speaking, the value of the scalar confinement parameter $E_c$ ranges from $O(\frac{1}{1000})$ to $O(\frac{1}{10})$. When matrix confinement is used, the parameter $E_c^{'}$ is larger than the equivalent value of the scalar confinement parameter because the matrix confinement implicitly contains the grid size as a scaling factor.

If the problem solved has analytical solution, or other computational results, or the experimental results available, then the value of the confinement parameter may be tuned by comparison with these results. Otherwise, the value of the confinement parameter may be tuned based on experience with similar flow problems. In extreme cases, when very large values of confinement parameter are used, the solution with confinement may appear to become chaotic. In other cases, too large a value of confinement will produce non-physical flows. In some instances, flows which would be expected to separate, will not with very large values of confinement are used. More details bout this will be discussed in Chapter 3 - Chapter 7.

# Chapter 3

# Vortical Solutions of the Conical Euler Equations

In this chapter we will first discuss the previous studies for conical flows over the last two decades, then describe the detailed formulations for Conical Euler Equations (CEE) and the special procedures of Compressible Vorticity Confinement (CVC) for conical flows; secondly, we will present the details about grid generation, finite-volume formulation and boundary handling procedures; and finally we will give some of our computational results and analysis for conical flows past flat delta wings.

## 3.1 Introduction

Leading-edge vortex flows in particular are of great interest in modern CFD because leeward vortices are very important for lift and stability of flight. We take them as our application because a flat plate delta wing of very simple geometry in high speed and high angle of attack flight can produce a rich variety of shock/vortex interaction patterns. In the general situation, flow separates at the leading edge of the wing, resulting in large primary vortices on the leeward of the wing with smaller viscous-induced secondary vortices beneath them. Most of the researchers model the vortex using a set of governing equations: potential equation, Euler equations and NS equations. Here we only consider the Euler equations in the remainder of this chapter.

The numerical method consists of discretizing the Euler equations on a grid and solving the resulting set of algebraic equations numerically. The Euler equations are more attractive as a solution for conical vortex flows, because they admit distributed vorticity as a solution and cost less than NS equations. They can model the primary vortex and shock wave with the secondary separation or viscous effects ignored. Solutions of Euler equations with central-difference conservation schemes have been carried out by Powell [11], Rizzi [37], Rizzi and Eriksson [38], Murman *et al.* [39], Newsome [40], Kandil and Chuang [41] and others. Upwind-difference conservation schemes have been used by Newsome and Thomas [42], Chakravarthy and Ota [43]. A characteristic-based non-conservative scheme has been used by Marconi [44]. Grossman used the transonic numerical techniques to solve the conical flow equation and made remarkable progress in developing this methodology [45]. All of these references gave reasonable estimates for the pressure coefficient on the wing. However, some of them over-predicted the suction peak and predicted more outboard position of the primary vortex than the experiments.

Hu and Grossman used the CVC method to calculate the flows over flat delta wings [46] and eliminated the over-prediction of the suction peak of the pressure coefficient due to the primary vortex, obtaining good agreement with experimental results. This may be explained by the fact by using vorticity confinement the location of the primary vortex is closer to the experiments and the velocity distribution near the primary vortex matches better to actual flow pattern than the other calculations. As a result, the Mach numbers of the flows on both side of the cross flow shocks located near the wall of the flat plate and the primary vortex are more closer to the measured values, as well as the positions of the primary vortex and the cross flow shocks. Furthermore, in this complex supersonic vortex dominated flow, the pressure coefficient not only depends on the primary vortex, but also depends on the cross-flow shocks and their interaction. Vorticity confinement appears to play an important role in obtaining good agreement with the experiments.

The purpose for this calculation was to test how the CVC method works with complex supersonic vortex dominated flows. In this calculation, the CVC method reduced the diffusion of the vorticity of the primary vortex, compared to the traditional methods.

## 3.2 Governing Equations

The governing equations used in the present study are the Conical Euler Equations (CEE). In order that these equations are held, there are three assumptions:

1. The flow field is conically self-similar;
2. Reynolds number goes to infinity;
3. The fluid is an inviscid, non-conducting, ideal gas.

The supersonic inviscid flow over a conically self-similar geometry belongs to this class of problems limited by these assumptions. The Reynolds number will not truly go to infinity in practical flow situations, but must be large enough so that the viscous and thermal boundary layers on the wing can be ignored.

The transformation from Cartesian coordinates $(x, y, z)$ to conical coordinates $(r, \xi, \eta)$ is defined as follows:

$$\left.\begin{aligned} r &= \sqrt{x^2 + y^2 + z^2}, \\ \xi &= y / x, \\ \eta &= z / x. \end{aligned}\right\} \tag{3.1}$$

After transforming from Cartesian coordinates to conical coordinates Eqs. (2.10) –(2.11) can be rewritten as follows:

$$\frac{r}{k}\frac{\partial}{\partial t}\begin{pmatrix} \rho \\ \rho u \\ \rho v \\ \rho w \\ \rho e_O \end{pmatrix} + \frac{r}{k^2}\frac{\partial}{\partial r}\begin{pmatrix} \rho\tilde{U} \\ \rho u\tilde{U} + p \\ \rho v\tilde{U} + \xi p \\ \rho w\tilde{U} + \eta p \\ \rho\tilde{U}h_0 \end{pmatrix} + \frac{\partial}{\partial \xi}\begin{pmatrix} \rho\tilde{V} \\ \rho u\tilde{V} - \xi p \\ \rho v\tilde{V} + p \\ \rho w\tilde{V} \\ \rho\tilde{V}h_0 \end{pmatrix} + \frac{\partial}{\partial \eta}\begin{pmatrix} \rho\tilde{W} \\ \rho u\tilde{W} - \eta p \\ \rho v\tilde{W} \\ \rho w\tilde{W} + p \\ \rho\tilde{W}h_0 \end{pmatrix} + 2\begin{pmatrix} \rho u \\ \rho u^2 + p \\ \rho uv \\ \rho uw \\ \rho uh_0 \end{pmatrix} = \frac{r}{k}S\,, \tag{3.2}$$

where

$$\left.\begin{aligned} k &= \sqrt{1+\xi^2+\eta^2}, \\ \tilde{U} &= u+\xi v+\eta w, \\ \tilde{V} &= v-\xi u, \\ \tilde{W} &= w-\eta u. \end{aligned}\right\} \tag{3.3}$$

The details about how to get Eq. (3.2) are presented in Appendix B. As we know that the boundary conditions and the vorticity confinement must satisfy the conical assumption $\frac{\partial}{\partial r}=0$. In order to make the boundary conditions conical, the boundaries of the computational domain must coincide with specify "rays"; for example, the grid corresponding to bow shock, the wing wall and leading edges of the wing must be generated by rays emanating from the apex. The class of inviscid supersonic flows with shocks attached at the wing apex will satisfy these conical boundary conditions. For vorticity confinement term S, the component in ray direction of "body force" $\vec{f}_b$ must be zero so that vorticity confinement is consistent with the conical assumptions. Otherwise, there will be acceleration in the ray direction, and as a result, $\frac{\partial Q}{\partial r}$ will not be zero (Q is the state variables). The details of vorticity confinement term S will be discussed in the next section.

According to conical assumptions, the second term on left side of Eq. (3-2) can be removed. Hence we have

$$\frac{r}{k}\frac{\partial}{\partial t}\begin{pmatrix}\rho\\ \rho u\\ \rho v\\ \rho w\\ \rho e_O\end{pmatrix}+\frac{\partial}{\partial\xi}\begin{pmatrix}\rho\tilde{V}\\ \rho u\tilde{V}-\xi p\\ \rho v\tilde{V}+p\\ \rho w\tilde{V}\\ \rho\tilde{V}h_0\end{pmatrix}+\frac{\partial}{\partial\eta}\begin{pmatrix}\rho\tilde{W}\\ \rho u\tilde{W}-\eta p\\ \rho v\tilde{W}\\ \rho w\tilde{W}+p\\ \rho\tilde{W}h_0\end{pmatrix}+2\begin{pmatrix}\rho u\\ \rho u^2+p\\ \rho uv\\ \rho uw\\ \rho uh_0\end{pmatrix}=\frac{r}{k}S. \tag{3.4}$$

Eq. (3.4) is called CEE.

## 3.3 Vorticity Confinement Procedure

The construction of vorticity confinement for CEE is the essential issue in this chapter. How do we build the vorticity confinement term S so that it is consistent with the conical assumptions as mentioned in section 3.2? The component of "body force" $\vec{f}_b$ in r direction in conical coordinates must be zero. Otherwise, $\vec{f}_b$ will give the fluid "particles" acceleration in ray direction. If we take cross-flow vorticity $\vec{\omega}_r$ (Appendix B) that is perpendicular to cross-flow plane $\xi - \eta$ as the vorticity vector in the vorticity confinement procedure, then the unit vector $\hat{n}_c$ defined as

$$\hat{n}_c = -\frac{\nabla(|\vec{\omega}_r|)}{|\nabla(|\vec{\omega}_r|)|} \tag{3.5}$$

will lie on cross-flow plane $\xi - \eta$, hence "body force" $\vec{f}_b$ defined as

$$\vec{f}_b = -E_c \hat{n}_c \times \vec{\omega}_r \tag{3.6}$$

must lie on cross-flow plane $\xi - \eta$ also.

After some algebraic manipulation (the details can be found in Appendix B), we found the relationships between the unit Cartesian coordinate vector $(\hat{i}, \hat{j}, \hat{k})$ and unit conical coordinate vector $(\hat{i}_r, \hat{i}_\xi, \hat{i}_\eta)$, and the expression of cross-flow vorticity vector $\vec{\omega}_r$ as follows:

$$\left.\begin{aligned}
\hat{i}_r &= \frac{1}{\sqrt{1+\xi^2+\eta^2}}(\hat{i} + \xi\hat{j} + \eta\hat{k}), \\
\hat{i}_\xi &= \frac{1}{\sqrt{1+\eta^2}\sqrt{1+\xi^2+\eta^2}}(-\xi\hat{i} + (1+\eta^2)\hat{j} - \xi\eta\hat{k}), \\
\hat{i}_\eta &= \frac{1}{\sqrt{1+\xi^2}\sqrt{1+\xi^2+\eta^2}}(-\eta\hat{i} - \xi\eta\hat{j} + (1+\xi^2)\hat{k}),
\end{aligned}\right\} \tag{3.7}$$

and

$$\vec{\omega}_r = \frac{\omega_0}{r}\hat{i}_r = \omega_r \hat{i}_r, \tag{3.8}$$

where

$$\omega_r = \frac{\omega_0}{r}, \tag{3.9}$$

$$\omega_0 = w_\xi - v_\eta + \xi(u_\eta + \xi w_\xi + \eta w_\eta) - \eta(u_\xi + \xi v_\xi + \eta v_\eta). \tag{3.10}$$

From Appendix B we can obtain three conical coordinate coefficients $h_r, h_\xi, h_\eta$

$$\left.\begin{aligned} h_r &= 1, \\ h_\xi &= \frac{r\sqrt{1+\eta^2}}{1+\xi^2+\eta^2}, \\ h_\eta &= \frac{r\sqrt{1+\xi^2}}{1+\xi^2+\eta^2}. \end{aligned}\right\} \tag{3.11}$$

Now we can calculate the "body force" $\vec{f}_b$ as follows:

$$\vec{f}_b = -E_c \hat{n}_c \times \vec{\omega}_r = -E_c \hat{n}_c \times (\omega_r \hat{i}_r), \tag{3.12}$$

where $\hat{n}_c$ is calculated using Eq. (3.5).

For convenience, let us define a scalar variable $\phi$ as

$$\phi = |\vec{\omega}_r| = |\omega_r \hat{i}_r| = |\omega_r|, \tag{3.13}$$

so

$$\left.\begin{aligned} \nabla|\vec{\omega}_r| &= \nabla\phi, \\ \hat{n}_c &= -\frac{\nabla\phi}{|\nabla\phi|}. \end{aligned}\right\} \tag{3.14}$$

The gradient in conical coordinates is given by

$$\left.\begin{aligned} \nabla\phi &= \frac{1}{h_r}\frac{\partial\phi}{\partial r}\hat{i}_r + \frac{1}{h_\xi}\frac{\partial\phi}{\partial\xi}\hat{i}_\xi + \frac{1}{h_\eta}\frac{\partial\phi}{\partial\eta}\hat{i}_\eta = \frac{\partial\phi}{\partial r}\hat{i}_r + \frac{1+\xi^2+\eta^2}{r\sqrt{1+\eta^2}}\frac{\partial\phi}{\partial\xi}\hat{i}_\xi + \frac{1+\xi^2+\eta^2}{r\sqrt{1+\xi^2}}\frac{\partial\phi}{\partial\eta}\hat{i}_\eta, \\ \phi &= |\omega_r| = \left|\frac{\omega_0}{r}\right| = \frac{|\omega_0|}{r}, \\ \frac{\partial\phi}{\partial r} &= \frac{\partial}{\partial r}\left(\frac{|\omega_0|}{r}\right) = -\frac{|\omega_0|}{r^2} + \frac{1}{r}\frac{\partial}{\partial r}|\omega_0|, \end{aligned}\right\} \tag{3.15}$$

where $\frac{\partial|\omega_0|}{\partial r}$ is zero because of the conical assumption. So with Eq. (3.15) we have

$$\nabla\phi = -\frac{|\omega_0|}{r^2}\hat{i}_r + \frac{1+\xi^2+\eta^2}{r\sqrt{1+\eta^2}}\frac{\partial\phi}{\partial\xi}\hat{i}_\xi + \frac{1+\xi^2+\eta^2}{r\sqrt{1+\xi^2}}\frac{\partial\phi}{\partial\eta}\hat{i}_\eta. \tag{3.16}$$

Substituting Eq. (3.7) into Eq. (3.16) and using $r = x\sqrt{1+\xi^2+\eta^2} = \sqrt{1+\xi^2+\eta^2}$ at $x = 1$ we get

$$\left.\begin{aligned} \nabla\phi &= \left(-\frac{|\omega_0|}{r^3} - \frac{\xi}{1+\eta^2}\frac{\partial\phi}{\partial\xi} - \frac{\eta}{1+\xi^2}\frac{\partial\phi}{\partial\eta}\right)\hat{i} + \left(-\frac{|\omega_0|\xi}{r^3} + \frac{\partial\phi}{\partial\xi} - \frac{\xi\eta}{1+\xi^2}\frac{\partial\phi}{\partial\eta}\right)\hat{j}, \\ &+ \left(-\frac{|\omega_0|\eta}{r^3} - \frac{\xi\eta}{1+\eta^2}\frac{\partial\phi}{\partial\xi} + \frac{\partial\phi}{\partial\eta}\right)\hat{k} = \phi_x\hat{i} + \phi_y\hat{j} + \phi_z\hat{k}, \\ \hat{n}_c &= \frac{-\nabla\phi}{|\nabla\phi|} = \phi_{xs}\hat{i} + \phi_{ys}\hat{j} + \phi_{zs}\hat{k}, \end{aligned}\right\} \tag{3.17}$$

where

$$\left.\begin{aligned}\phi_{xs} &= \frac{-\phi_x}{\sqrt{\phi_x^2+\phi_y^2+\phi_z^2}},\\ \phi_{ys} &= \frac{-\phi_y}{\sqrt{\phi_x^2+\phi_y^2+\phi_z^2}},\\ \phi_{zs} &= \frac{-\phi_z}{\sqrt{\phi_x^2+\phi_y^2+\phi_z^2}}.\end{aligned}\right\} \tag{3.18}$$

Also, $\vec{\omega}_r = \omega_r \vec{i}_r$ is known. So we have

$$\vec{\omega}_r = \frac{\omega_0}{r}\hat{i}_r = \frac{\omega_0}{1+\xi^2+\eta^2}(\hat{i}+\xi\hat{j}+\eta\hat{k}). \tag{3.19}$$

Now we can build $\vec{f}_b$ as

$$\vec{f}_b = -E_c\hat{n}_c \times \vec{\omega}_r = -E_c \begin{pmatrix} \hat{i} & \hat{j} & \hat{k} \\ \phi_{xs} & \phi_{ys} & \phi_{zs} \\ \dfrac{\omega_0}{1+\xi^2+\eta^2} & \dfrac{\omega_0\xi}{1+\xi^2+\eta^2} & \dfrac{\omega_0\eta}{1+\xi^2+\eta^2} \end{pmatrix} = f_{bx}\hat{i} + f_{by}\hat{j} + f_{bz}\hat{k}, \tag{3.20}$$

with the three components in Cartesian coordinates given by

$$\left.\begin{aligned} f_{bx} &= -\frac{E_c\omega_0}{1+\xi^2+\eta^2}(\eta\phi_{ys}-\xi\phi_{zs}), \\ f_{by} &= -\frac{E_c\omega_0}{1+\xi^2+\eta^2}(\phi_{zs}-\eta\phi_{xs}), \\ f_{bz} &= -\frac{E_c\omega_0}{1+\xi^2+\eta^2}(\xi\phi_{xs}-\phi_{ys}). \end{aligned}\right\} \tag{3.21}$$

Finally we get the expression of the vorticity confinement term as follows:

$$S=\begin{pmatrix} 0 \\ \rho f_{bx} \\ \rho f_{by} \\ \rho f_{bz} \\ \rho(uf_{bx}+vf_{by}+wf_{bz}) \end{pmatrix} = \begin{pmatrix} 0 \\ -\frac{E_c\rho\omega_0}{1+\xi^2+\eta^2}(\eta\phi_{ys}-\xi\phi_{zs}) \\ -\frac{E_c\rho\omega_0}{1+\xi^2+\eta^2}(\phi_{zs}-\eta\phi_{xs}) \\ -\frac{E_c\rho\omega_0}{1+\xi^2+\eta^2}(\xi\phi_{xs}-\phi_{ys}) \\ -\frac{E_c\rho\omega_0}{1+\xi^2+\eta^2}[u(\eta\phi_{ys}-\xi\phi_{zs})+v(\phi_{zs}-\eta\phi_{xs})+w(\xi\phi_{xs}-\phi_{ys})] \end{pmatrix}. \tag{3.22}$$

The CVC procedure for supersonic conical flows was also described in the paper of Hu and Grossman [46].

## 3.4 Solution Procedure

In the present study the scheme used to solve conical equations Eq. (3.4) is a finite-volume, cell-centered, multi-stage time-stepping Runge-Kutta scheme that is described in Chapter 2. The state variables are stored at the cell-center. The grid generation, finite volume formulation, flux integration, vorticity confinement implementation, and boundary conditions will be discussed in this section.

### 3.4.1 Grid Generation

A modified Joukowski transformation is used to generate grid with flat plate geometries. The grid on cross-flow plane $\xi - \eta$ is generated from the complex plane $\hat{\zeta}$. The transformation is given by

$$\xi + i\eta = \hat{\zeta} + a^2 / \hat{\zeta}, \tag{3.23}$$

where

$$\left.\begin{aligned} &i = \sqrt{-1}, \\ &a^2 = [\tan^2(\pi/2 - \Lambda) - \tan^2\delta]/4, \\ &\left|\hat{\zeta}_b\right| = [\tan(\pi/2 - \Lambda) + \tan\delta]/2, \end{aligned}\right\} \tag{3.24}$$

where $\Lambda$ is the leading-edge sweep angle of the wing, $\delta$ is the half of the vertex angle of the elliptic cone; and the radius of the circle in complex plane $\hat{\zeta}$ corresponding to the wing elliptic section in $\xi - \eta$ plane is $\left|\hat{\zeta}_b\right|$. The flat plate wing is simply obtained by setting $\delta = 0$. The grid points at $(j,k)$ are generated by

$$\left.\begin{aligned} \xi_{j,k} &= (\left|\hat{\zeta}_{j,k}\right| + \frac{a^2}{\left|\hat{\zeta}_{j,k}\right|})\cos\theta_{j,} \\ \eta_{j,k} &= (\left|\hat{\zeta}_{j,k}\right| - \frac{a^2}{\left|\hat{\zeta}_{j,k}\right|})\sin\theta_j, \end{aligned}\right\} \tag{3.25}$$

where

$$\left.\begin{aligned} \left|\hat{\zeta}_{j,k}\right| &= \left|\hat{\zeta}_{b,k}\right| - \frac{\left|\hat{\zeta}_{b,k}\right| - \left|\hat{\zeta}_{o,k}\right|}{\sigma}\ln[1-(1-e^{-\sigma})(\frac{k-1}{k\max-1})], \\ \theta_j &= \frac{\pi}{2}(1-2\frac{j-1}{j\max-1}), \end{aligned}\right\} \tag{3.26}$$

where $\left|\hat{\zeta}_{o,k}\right|$ is the outer boundary position, (*j*, *k*) is the index of grid cell, *jmax* and *kmax* are the maximum indices in $\xi, \eta$ directions. $\sigma$ is a grid stretching parameter. $\sigma$ is 2.0 in the present calculation. Grid is set to $64 \times 64$. This method was originally proposed by Marconi [45], yielding near-conformal grids with good resolution near the surface of the wing. A sample grid generated by this method is shown in Figure 3.1

### 3.4.2 Finite Volume Formulation

The factor $\frac{r}{\kappa}$ in conical Euler Eq. (3-4) can be simplified as follows:

$$\frac{r}{\kappa} = \frac{\sqrt{x^2 + y^2 + z^2}}{\sqrt{1 + \xi^2 + \eta^2}} = x \frac{\sqrt{1 + \xi^2 + \eta^2}}{\sqrt{1 + \xi^2 + \eta^2}} = x \,. \tag{3.27}$$

Solved at $x = 1$, Eq. (3-4) can be rewritten as follows:

$$\frac{\partial Q}{\partial t} + \frac{\partial \tilde{G}}{\partial \xi} + \frac{\partial \tilde{H}}{\partial \eta} + 2F = S \,, \tag{3.28}$$

where

$$Q = \begin{pmatrix} \rho \\ \rho u \\ \rho v \\ \rho w \\ \rho e_O \end{pmatrix}, \tilde{G} = \begin{pmatrix} \rho \tilde{V} \\ \rho u \tilde{V} - \xi p \\ \rho v \tilde{V} + p \\ \rho w \tilde{V} \\ \rho \tilde{V} h_0 \end{pmatrix}, \tilde{H} = \begin{pmatrix} \rho \tilde{W} \\ \rho u \tilde{W} - \eta p \\ \rho v \tilde{W} \\ \rho w \tilde{W} + p \\ \rho \tilde{W} h_0 \end{pmatrix}, F = \begin{pmatrix} \rho u \\ \rho u^2 + p \\ \rho uv \\ \rho uw \\ \rho u h_0 \end{pmatrix}. \tag{3.29}$$

S is calculated using Eqs. (3.12)-(3.22). The discretization of the CEE (3.28) is formulated over a cell on the cross-flow plane $\xi - \eta$. This gives the following:

$$\iint_{\Omega}\frac{\partial Q}{\partial t}d\xi d\eta+\iint_{\Omega}(\frac{\partial \tilde{G}}{\partial \xi}+\frac{\partial \tilde{H}}{\partial \eta})d\xi d\eta+\iint_{\Omega}2Fd\xi d\eta=\iint_{\Omega}Sd\xi d\eta\,. \tag{3.30}$$

Using Gauss's divergence theorem, Eq. (3-30) can be rewritten as follows:

$$A_c\frac{\partial \overline{Q}}{\partial t}+\oint_{\partial\Omega}(\overline{G}d\eta-\overline{H}d\xi)+2A_c\overline{F}=A_c\overline{S}\,, \tag{3.31}$$

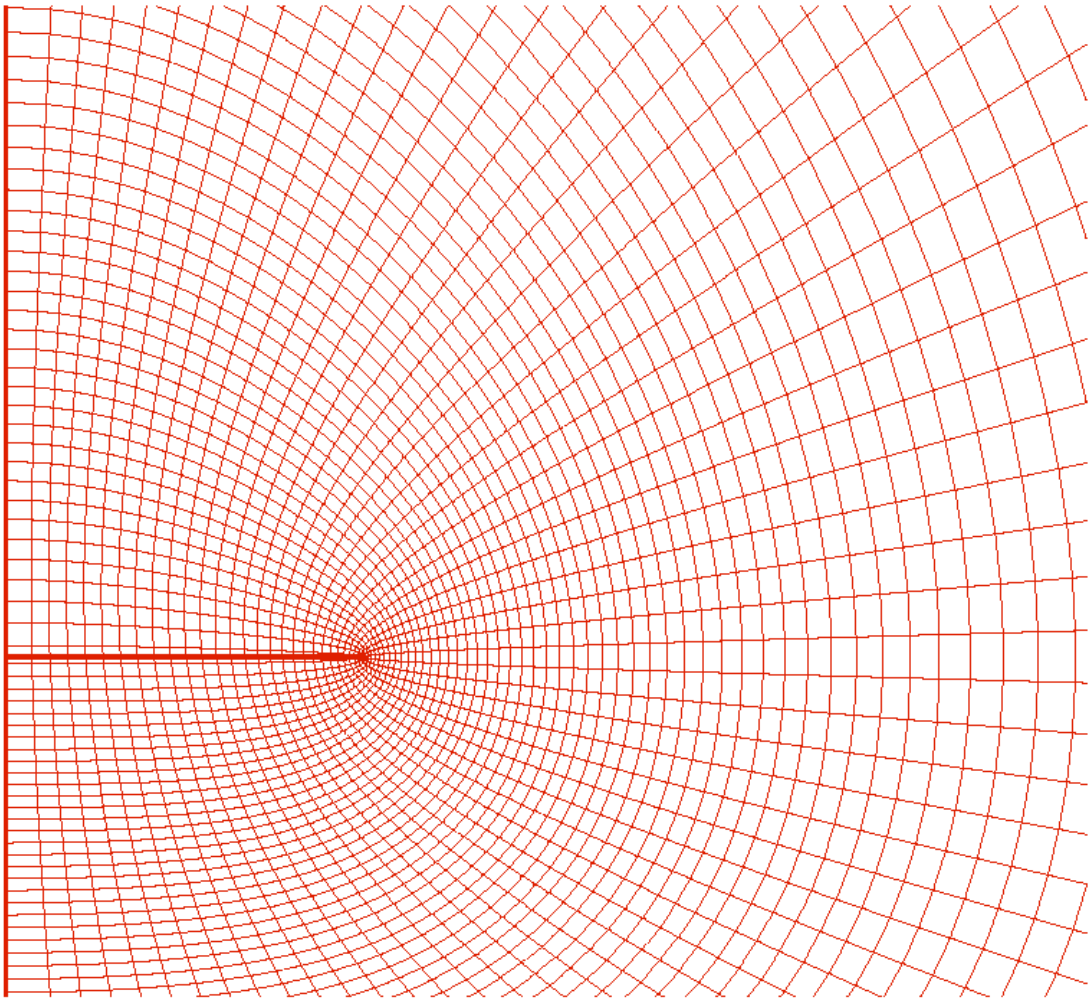

Figure3.1: The sample grid for a flat plate delta wing.

where $A_c$ is the area of the cell, the overbar denotes an average value over the cell. Solving $\frac{\partial \overline{Q}}{\partial t}$, the time average rate of change of the state vector Q within a cell, gives the following:

$$\frac{\partial \overline{Q}}{\partial t} = -\frac{1}{A_c}\oint_{\partial\Omega}(\overline{G}d\eta - \overline{H}d\xi) - (2\overline{F} - \overline{S}) . \tag{3.32}$$

The flux integration $\oint_{\partial\Omega}(\overline{G}d\eta - \overline{H}d\xi)$ is calculated by a trapezoidal integration around the cell. This gives the following:

$$\oint_{\partial\Omega}(\overline{G}d\eta - \overline{H}d\xi) = \sum_{faces}[\frac{1}{2}(\overline{G}_1 + \overline{G}_2)(\eta_2 - \eta_1) - \frac{1}{2}(\overline{H}_1 + \overline{H}_2)(\xi_2 - \xi_1)] . \tag{3.33}$$

where the subscripts for $\overline{G}$ and $\overline{H}$ denote the two cells that define the face, the subscripts for $\xi$ and $\eta$ denote the two end points of the grid cell face (see Figure 3.2) , ordered so that the integral is carried out in a counter-clockwise direction. This is usually second-order accurate, regardless of the stretching of the grid [33]. The cell-average of the source term is calculated by the cell average variables, because our scheme is cell-centered scheme, so the calculation of $\overline{F}, \overline{S}$ is straightforward.

The cell area $A_c$ is calculated by the following formula according the grid stencil shown in Figure 3.2.

$$A_c = \frac{1}{2}[(\eta_3 - \eta_1)(\xi_2 - \xi_4) - (\xi_3 - \xi_1)(\eta_2 - \eta_4)] . \tag{3.34}$$

The artificial matrix dissipation model MDM [(1)] described in Chapter 2 and a 3-stage Runge-Kutta time integration scheme is used.

To enhance the convergence to steady-state solution, local time-stepping is used. The time-step is calculated by

$$\Delta t = CFL.\frac{A_c}{\oint_{\partial\Omega}(|\hat{V}|+c)dl}, \tag{3.35}$$

where c is the local speed of sound, and $\hat{V}$ is evaluated at cell face that is calculated by averaging the values of the two cells that define that face.

### 3.4.3 Boundary Conditions

There are 4 boundary conditions that must satisfy with the Euler equations:

1. No penetration condition enforced at the solid wall that has been discussed in Chapter 2;
2. Free-stream conditions upstream of the bow shock;
3. The Kutta conditions at the leading-edges;
1. The symmetry condition at the symmetry plane.

The free-stream condition is implemented numerically by placing the outer boundary of the computational plane outside the bow shock and setting the state vector at each point on the outer boundary

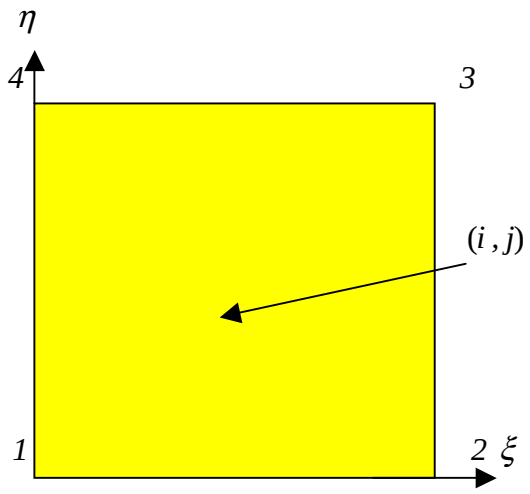


Figure 3.2: The grid stencil on a cross-flow plane.

to the free stream state vector. The outer boundary chosen is an expanded Mach cone, shifted to lee-side to account for the angle of attack. This gives the following:

$$\left.\begin{aligned}\xi &= r_s \sin\phi, \\ \eta &= r_s \cos\phi + z_s \cos^2\phi,\end{aligned}\right\} \tag{3.36}$$

where

$$\left.\begin{aligned}r_s &= 3\sin^{-1}(\frac{1}{M_\infty}), \\ z_s &= \max(3\sin\alpha, 3\sin 10^0),\end{aligned}\right\} \tag{3.37}$$

where $\phi$ is the angle between the ray in the domain and the ray at boundary. The Kutta condition physically implies that the cross-flow leaves the leading edge smoothly. This rules out the possibility of infinite velocity at the leading edge. In the real flows, the viscosity sets the Kutta condition. Similarly, in numerical simulation the artificial viscosity in the region of leading edge enforces the Kutta condition. In the present calculation, the coefficients of second-order dissipation term for MDM [(1)] at several cells in the vicinity of the leading edge are set to the maximum value in the whole domain to enforce the Kutta condition.

The symmetry plane is introduced so that the flow past a wing at zero yaw angle can be solved on a half plane. The condition to be enforced at the symmetry plane is that the velocity component v, through symmetry plane, is zero. In the present study this was implemented by initially setting v to zero and zeroing out the distributed flux in the y-direction in the continuing calculation.

## 3.5 Numerical Results for the Conical Euler Equations

In this section we will present the numerical results for CEE using the numerical method MDM [(1)] along with the MCVC method described in Chapter 2 and the procedures described in sections 3.1- 3.4. Representative plots of some flow variables will be presented and discussed. A part of the results that will

be presented here was also discussed by Hu and Grossman in Ref. [46]. Two cases will be used to illustrate the capability of CVC procedure in the calculations of complex supersonic vortex dominated flows. One case is the calculation for the flow over a flat delta wing with a moderate supersonic Mach number and an angle of attack ($M_\infty = 1.7, \alpha = 12^0, \Lambda = 75^0$) and the other case is with a higher Mach number and angle of attack ($M_\infty = 2.8, \alpha = 20^0, \Lambda = 75^0$). The calculations for these two cases were performed on the $64 \times 64$ stretched grid on the cross-flow plane $\xi - \eta$ (see Figure 3.1) with dissipation parameters set to $k^{(2)} = 0.1, k^{(4)} = 0.005$ and the confinement parameter $E_c^{'} = 15.0$. Note here that we are using matrix confinement which effectively scales the confinement parameter by the grid size. Elsewhere in this dissertation, scalar confinement is used with correspondingly small values of the confinement parameter ($E_c : 0.001 - 0.1$). Several set of values of dissipation parameters were tested at the beginning of the calculations so that the added artificial dissipation term was small as much as possible. When the values of the dissipation parameters were too small, the numerical solution showed oscillation. The current ones were the right ones that were found so that the numerical solutions were stable. It was time-consuming to choose the value of the confinement parameter in these cases. First, several small values were tested. By the observation of the scope of the vortex we saw that the vorticity was still be diffused from the center of the vortex. Under these circumstances the computed vortex region was larger than the measured one in the experiment. Next, several larger values of confinement parameters were tested, until the size of the primary vortex closed to the experimental one. The current one was the right one used in the present calculation to prevent the vorticity from diffusing away by the numerical dissipation and keep the right size of the primary vortex.

All of the plots in this section are on the cross-flow plane $\xi - \eta$. The coordinate axes are scaled by local half span of the wing and denoted by $\xi / b$ and $\eta / b$ respectively. The wing is at $\eta / b = 0$ and extends from $\xi / b = -1$ to $\xi / b = 1$. Because the flow is with zero yaw angle flight, the flow is symmetry about $\xi / b = 0$, so only positive $\xi$ plane is shown. The contour plots only show the qualitative information such as shock, vortex, and vortex/shock interactions, while the pressure coefficient profile on the surface of the wing and the comparison with experimental and other computational results will give the quantitative information.

In order to evaluate the accuracy of the basic code, we performed a calculation of a $15^0$ half-angle circular cone at zero angle of attack. The computation is done without confinement. The dissipation parameters in MDM [1] $k^{(2)}$ was set to 0.5, and $k^{(4)}$ was set to 0.01. The calculation was performed on a

grid with 64 mesh points in circumferential direction (half cone) and 51 mesh points in the azimuthally direction. The pressure coefficient distribution in the shock layer is presented in Figure 3.3. The agreement with the accurate Taylor-Maccoll analytical solution [47] is excellent. The bow shock is accurately captured within two mesh points.

### 3.5.1 Topology of the Conical Flows

The topological information about the conical flow is presented through cross-flow velocity vector plots and cross-flow streamline plots. Both the velocity vector and streamline plots are based on the cross-flow velocity $\tilde{v} = v - \xi u$ and $\tilde{w} = w - \eta u$. The cross-flow velocity vector plots are generated by drawing at each cell center, an arrow whose vector component are proportional to the local values of $\tilde{v}$ and $\tilde{w}$.

#### 3.5.1.1 Case 1 --- $M_\infty = 1.7, \alpha = 12^0, \Lambda = 75^0$

Figure 3.4 presents the velocity vectors. The primary vortex and the feeding sheet are clearly seen in this Figure. The cross-flow streamlines are presented in Figure 3.5 that shows the primary vortex, the node at the windward symmetry point, and saddle points at the leeward symmetry point and on the windward side of the wing near the leading edge. The underside of the vortex shows a reverse curvature that is the evidence of a cross-flow shock underneath the primary vortex. Figure 3.5 shows the good qualitative agreement between the present calculation and the experiment, including the shape and position of the primary vortex and the leading edge vortex sheet.

#### 3.5.1.2 Case 2 --- $M_\infty = 2.8, \alpha = 20^0, \Lambda = 75^0$

Figure 3.6 presents the cross-flow velocity vectors. The feeding sheet and primary vortex is shown clearly, as well as three cross-flow shocks: a shock above the vortex, where the flow direction is inboard, a shock inboard of the vortex, where the flow direction is towards the wing, and a shock under the vortex, where the flow is outboard, this reverse cross-flow shock is under the vortex. The shocks above and inboard of the vortex are representative of high angle of attack cases. Figure 3.6 also shows the blowups of the vortex core, the feeding sheet and the reverse cross-flow shock. The feeding sheet shows a large change in the magnitude of the cross-flow velocity across a very small region, with the vector remaining parallel

through the sheet. The cross-flow shock is characterized by a change in both magnitude and the direction of the vectors. The cross-flow streamlines are presented in Figure 3.7 that shows a node at the windward symmetry point and saddle points at the leeward symmetry point, the leading edge and the outboard portion of the windward side of the wing. The vortex has a high degree of reverse curvature, suggesting a strong cross-flow shock underneath the vortex. The comparison with the experiment in Figure 3.7 shows that a good qualitative agreement was obtained in the present calculation, including the shape and the position of the primary vortex and the leading edge vortex sheet.

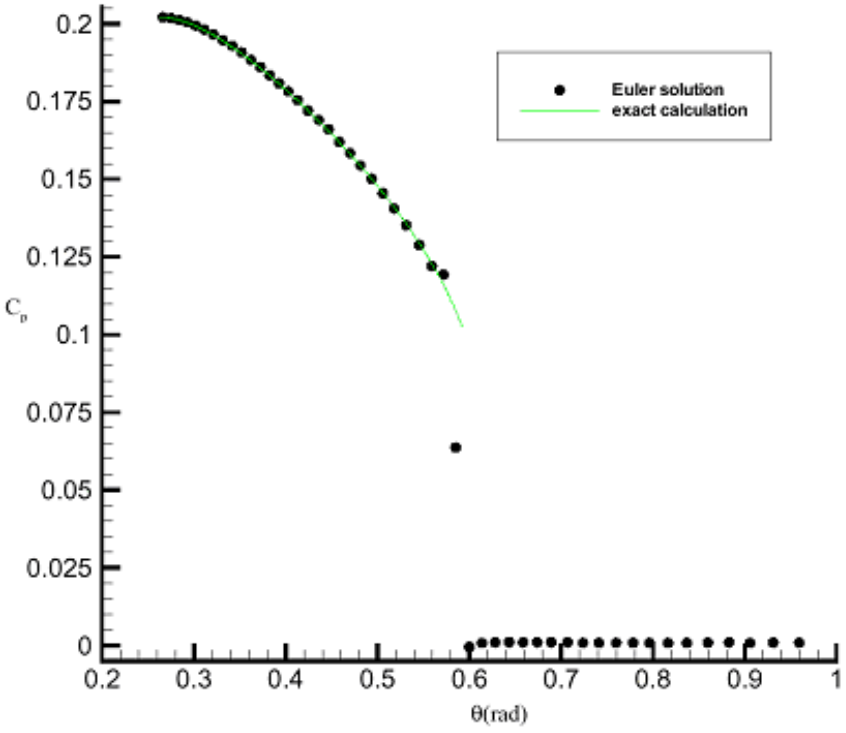


Figure 3.3: Pressure distributions in the shock layer of a circular cone with $15^0$ half angle at zero angle of attack and $M_\infty = 2.0$.

## 3.5.2 Pressure Coefficient Profile

The variable considered here is the static pressure coefficient distributed on the surface of the wing.

$$c_p = \frac{p - p_\infty}{\frac{\gamma}{2} p_\infty M_\infty^2}. \tag{3.38}$$

Figure 3.8 presents the pressure coefficient profile on a flat delta wing with $M_\infty = 1.7, \alpha = 12^0, \Lambda = 75^0$ and Figure 3.9 shows the pressure coefficient profile on a flat delta wing with $M_\infty = 2.8, \alpha = 20^0, \Lambda = 75^0$. In the same figure we presented the results calculated both with confinement and without confinement, experiment data of Miller and Wood [2] as discussed in Ref. [11], and the solution of Euler equations of Powell [11] performed on an equivalent $128 \times 128$ grid with local grid refinement in the vicinity of the vortex and the leading edge. From Figure 3.8 we see that even though the solution with vorticity confinement was not completed with locally refined grid and was performed with a quarter number of grid points of that used by Powell, the agreement with the experiment data appear to be better in the inboard and the core region of the vortex; the over-prediction suction peak under the primary vortex was eliminated. The reason has been discussed previously in the introduction of this chapter. We note that our solution without confinement shows a reduced suction peak. However, this solution shows larger size of the primary vortex than the measured one in the experiment because it was diffused by the numerical dissipation inherently related to the numerical discretization. Figure 3.9 shows that the leeward pressure is nearly constant for the flight at a higher angle of attack and higher Mach number, the present computed solution agrees well with the measured data and the computational result of Powell. Figure 3.10 presents the contours of the cross-flow Mach numbers for the case with $M_\infty = 1.7, \alpha = 12^0, \Lambda = 75^0$. Figure 3.11 shows the contours of the cross-flow Mach numbers for the case with $M_\infty = 2.8, \alpha = 20^0, \Lambda = 75^0$. From the theoretical analysis we can conclude that the Mach number is nearly constant on the windward side, increasing through the expansion at the leading edge, reaching to its maximum values above and below the vortex. The deceleration occurs through the cross-flow shock. The gradients are highest at the cross-flow shock, the sheet, and the core region where the cross-flow Mach number reaches zero. The pressure coefficient contours for the two cases are presented in Figure 3.13 and Figure 3.14. The pressure coefficient reaches the minimum in the core of the vortex. It is nearly constant on the windward and on the leeward side inboard of the vortex. The expansion fan is located at the leading edge and the expansion and recompression occurs under the vortex. Comparing these two figures we can conclude that the case with higher Mach number and an angle of attack shows stronger windward bow shock than the case with lower Mach number and angle of attack.

From the analyses above, we see that CVC works well in the calculations of the complex supersonic vortex dominated flows over flat delta wings. It appears that the confinement procedure eliminates the overshoot of the suction peak of the pressure coefficient in the primary vortex computed in Ref. [11]. In addition, it appears that the CVC method shrinks the over - predicted size of the primary vortex that may be caused by the numerical dissipation. However, the bow shock does not appear to be strongly affected by the confinement, because the conical shock has relatively small vorticity gradients. On the other hand, the cross-flow shock looks to be strongly affected by confinement, especially the position of the cross-flow shock, because of the strong vorticity that has strong vorticity gradients. Therefore, It should be noted that CVC works and only works in the vortical regions in which there exists strong vorticity gradients.

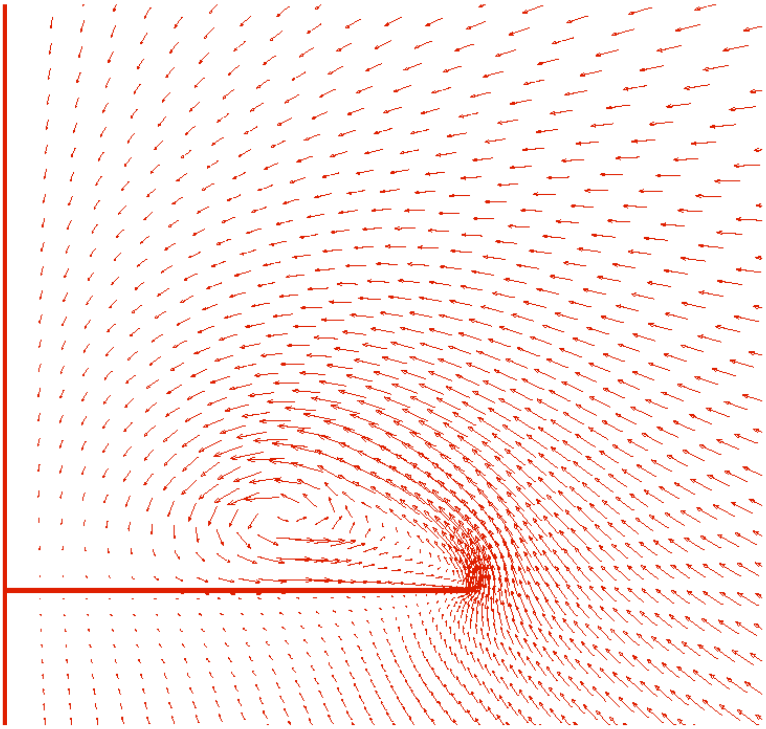

Figure 3.4: The cross-flow velocity vector distributions for a flat plate delta wing at $M_\infty = 1.7, \alpha = 12^0, \Lambda = 75^0$.

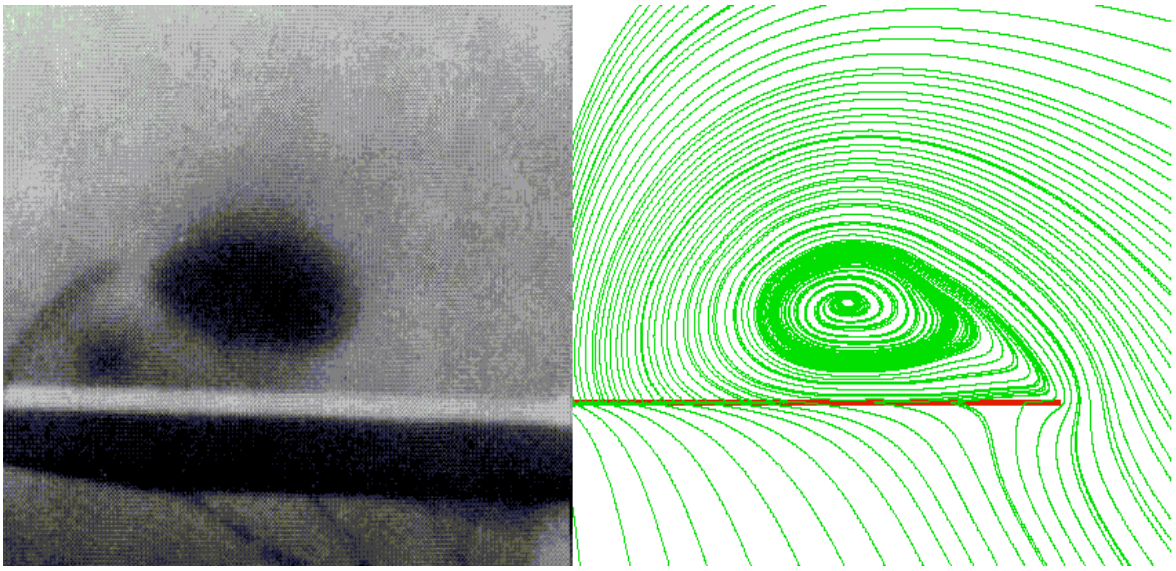

Figure 3.5: The experimental result and the present computed streamline distributions on the cross-flow plane for a flat plate delta wing at $M_\infty = 1.7, \alpha = 12^0, \Lambda = 75^0$. Left --- Experimental vapor screen [2]. Right --- the streamline distributions of the present calculation.

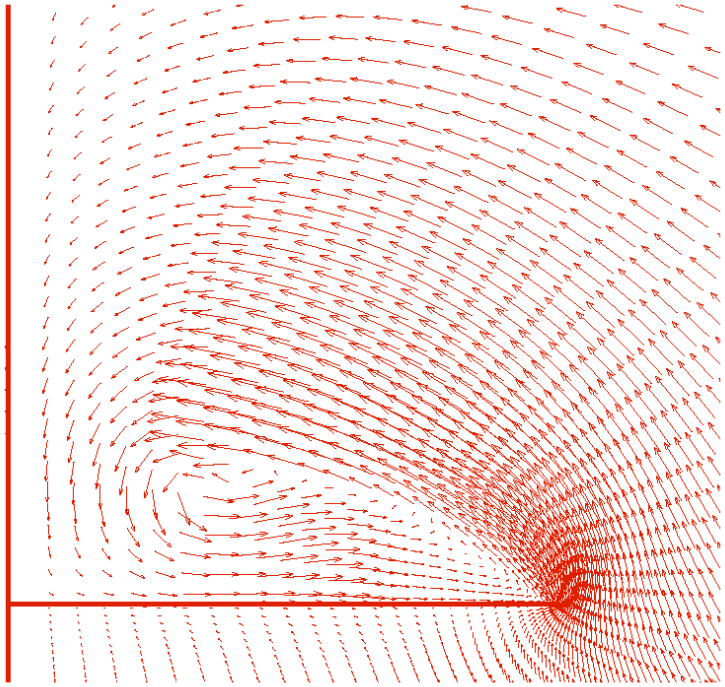

Figure 3.6: The cross-flow velocity vector distributions on a flat delta wing at $M_\infty = 2.8, \alpha = 20^0, \Lambda = 75^0$.

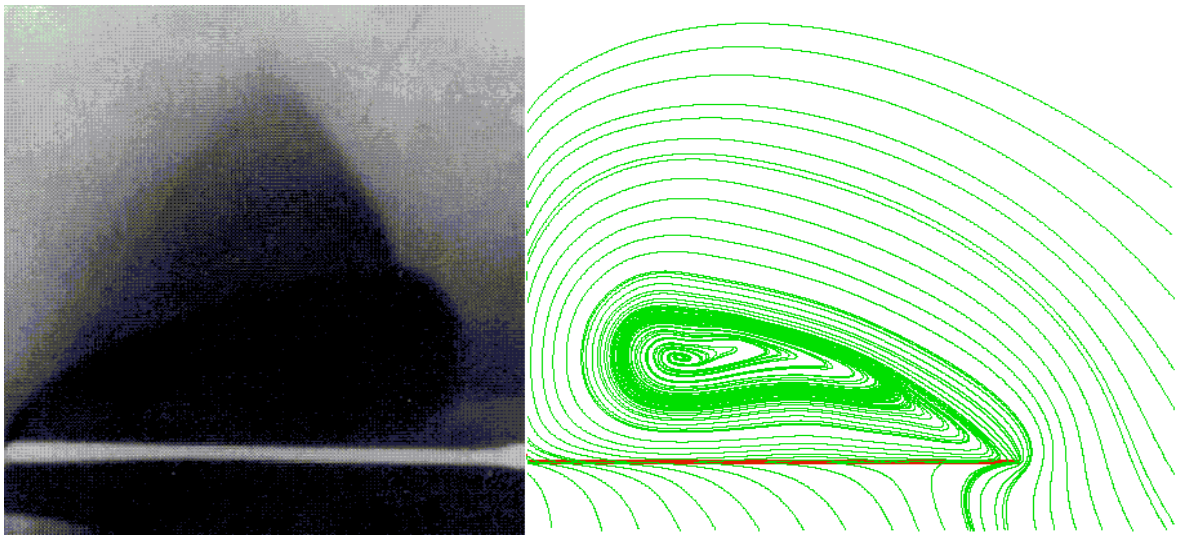

Figure 3.7: The experimental result and the present computed streamline distributions on the cross-flow plane for a flat plate delta wing at $M_\infty = 2.8, \alpha = 20^0, \Lambda = 75^0$. Left --- Experimental vapor screen [2]. Right --- the streamline distributions of the present calculation.

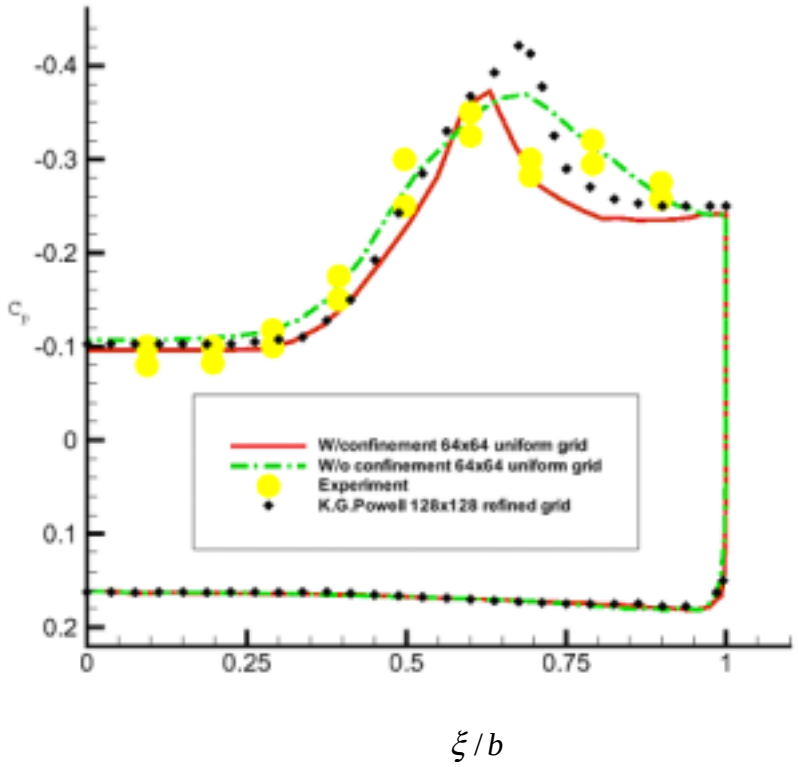


Figure 3.8: The pressure coefficient distributions on a flat delta wing at $M_\infty = 1.7, \alpha = 12^0, \Lambda = 75^0$.

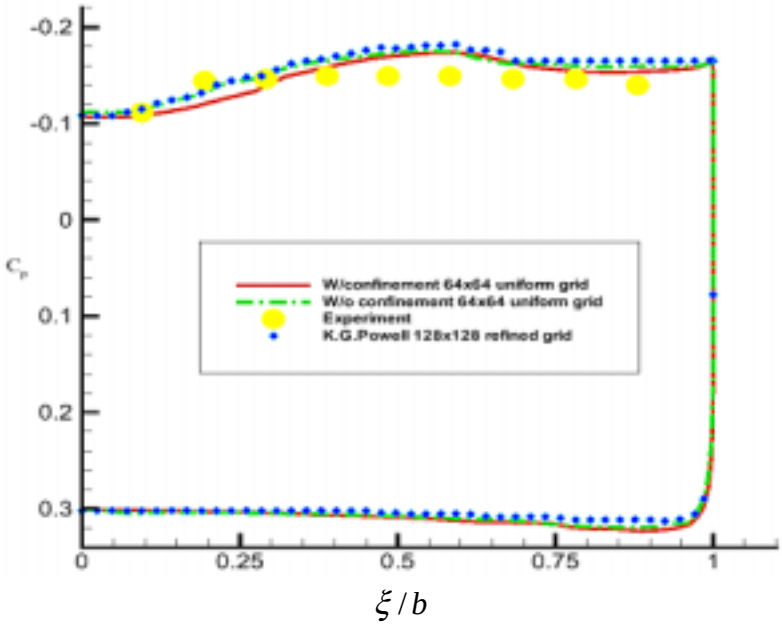


Figure 3.9: The pressure coefficient distributions on a flat delta wing at $M_\infty = 2.8, \alpha = 20^0, \Lambda = 75^0$.

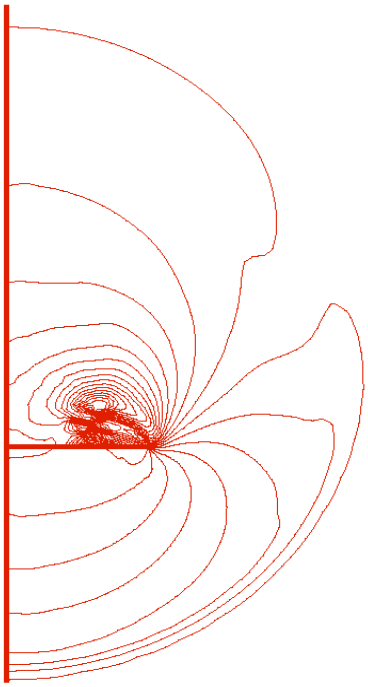

Figure 3.10: The Mach number contours for a flat delta wing at $M_\infty = 1.7, \alpha = 12^0, \Lambda = 75^0$.

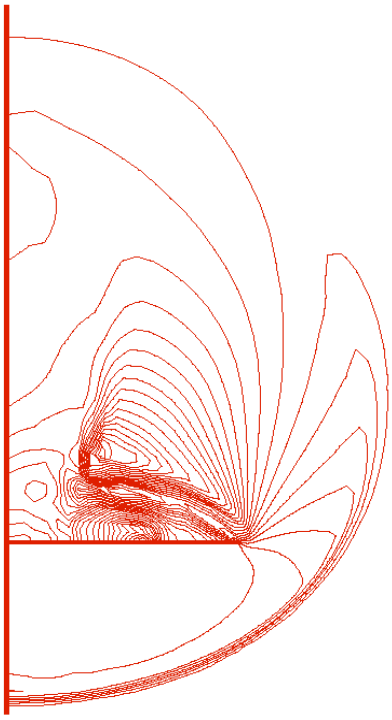

Figure 3.11: The Mach number contours for a flat delta wing at $M_\infty = 2.8, \alpha = 20^0, \Lambda = 75^0$.

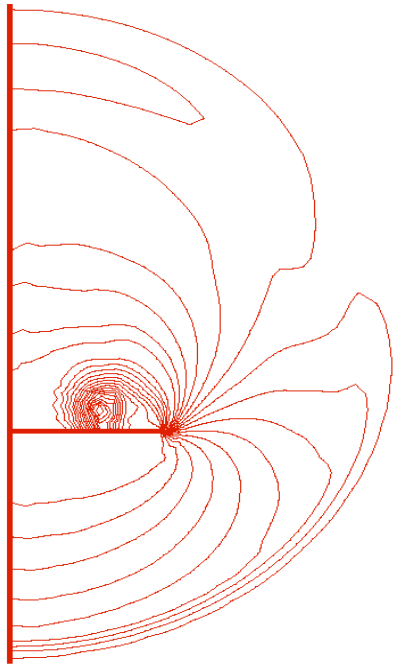

Figure 3.12: The pressure coefficient contours for a flat delta wing at $M_\infty = 1.7, \alpha = 12^0, \Lambda = 75^0$.

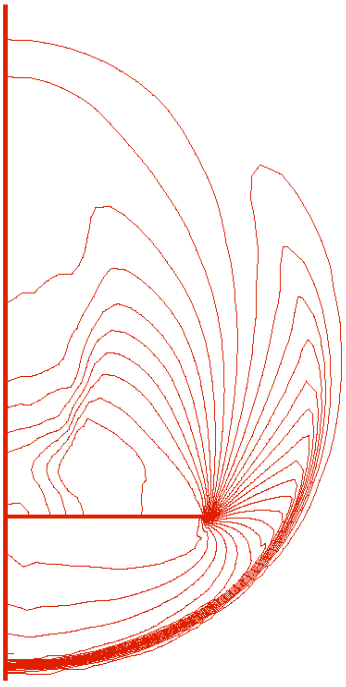

Figure 3.13: The pressure coefficient contours for a flat delta wing at $M_\infty = 2.8, \alpha = 20^0, \Lambda = 75^0$.

# Chapter 4

# Numerical Simulation of Shock-Bubble and Shock-Vortex Interaction

In this chapter we will investigate the vortex structures formed by a moving shock over a circular light-gas inhomogeneity (both a stationary bubble and a circular vortex) in a channel with a finite width. The pressure gradient from the shock wave interacts with the density gradient at the edge of the inhomogeneity to form a vortical layer around the perimeter, and the structure rolls up into a complex vortex structures.

The purpose for which we did these calculations is to see how CVC works with the vortical layer formed by the interaction between a moving shock wave and a circular light gas inhomogeneity. We will qualitatively compare the patterns of the vortical layer with the measured ones in the experiment and quantitatively compare the pressure, the density and vorticity in the centers of the vortices with the computed results obtained by using other computational techniques.

## 4.1 Overview for Previous Studies in Shock-Bubble and Shock-Vortex Interaction

James *et al.* performed a detailed numerical study for a weak shock wave passing through an isolated stationary cylindrical gas inhomogeneity [48]. They utilized a novel shock-capturing scheme in conjunction with a sophisticated mesh refinement algorithm to solve the two-dimensional compressible Euler equations for a two-component fluid (air-helium or air-refrigerant 22). They numerically reproduced the intricate mechanisms that were observed in the experiment. Yang *et al.* simulated the

vortex pair formed by shock-bubble interaction by solving two-dimensional Euler equations with a finite-difference Flux-Corrected-Transport algorithm (FCT) [9]. Using the numerical results they developed a relatively simple algebraic model that characterizes the dynamics of the vortex pair and that allows extrapolation of the numerical results to conditions of more interest in real engineering problems. Utilizing an adaptive unstructured scheme, Povitsky and Ofengeim studied the interaction between a vortical density inhomogeneity (VDI) (both stationary light gas bubble and a circular vortex) with a shock and expansion wave [8].

## 4.2 Present Studies for Shock-Bubble Interaction

To compare to the computational results of Yang *et al.* [9] and Povitsky and Ofengeim [8], we used the finite-volume scheme with MDM $^{(2)}$ and the scalar CVC described in Chapter 2 to perform the calculation of the same problem that was calculated by Yang and Povitsky *et al.* The dissipation parameter $E_d$ was set to 0.3. The confinement parameter $E_c$ was set to 0.005. In the process of calculation, several values of the dissipation parameter $E_d$ were tested, and the smallest one was used so that no oscillation occurred in the calculation. After the dissipation parameter was chosen, we fixed the value of $E_d$ and tuned the value of the confinement parameter $E_c$. We chose the value of $E_c$ in such a way so that we kept the edge of the vortical layer sharp as much as possible. The computation was performed with a $600 \times 200$ Cartesian grid. The initial conditions for the calculation were chosen to match the conditions present in the experiment of Jacobs [10] who studied the flow formed by a plane shock wave impinged on a laminar jet of helium injected into air at ambient pressure. The Mach number of the moving shock is 1.1. The density ratio of light/heavy gas is 0.138.

Figure 4.1 presents the density contours and comparison with the experimental PLIF images [10] that give the cross-section view of the evolving helium inhomogeneity. The density contours conveyed the information about organization and stabilization of the vorticity into a stable core. It also provided us the information about the straining of the vortex pairs and the motion of the light/heavy gas interface. In the time interval $t = 123 - 373\mu s$ the fluid that did not become part of the vortex core is pinched off as a pair of upstream tails. At the downstream end, a well-defined thin filament connected the two cores. This filament stretched and thinned in the vertical direction due to a strong straining motion from the high vorticity cores. In the time interval $t = 373 - 573\mu s$, the vortex gradually stabilized and the circulation of

the vortex core was obviously noted. In the time interval $t = 573 - 773\mu s$ , the core induced in each other a strong, horizontal velocity, thus moving downstream more rapidly than the tails, which stretched upstream as they trailed behind the core. These tails also experienced strong induced velocities that caused them to rotate towards the centerline. Figure 4.2 presents the comparison of the present results and the computed results of Yang *et al.* [9] using FCT scheme. The present results show much less numerical diffusion and better agreement with the experiment results. Figure 4.3 shows the comparison of present results and the results of Povitsky and Ofengeim [8] using an adaptive unstructured scheme; a good agreement was obtained.

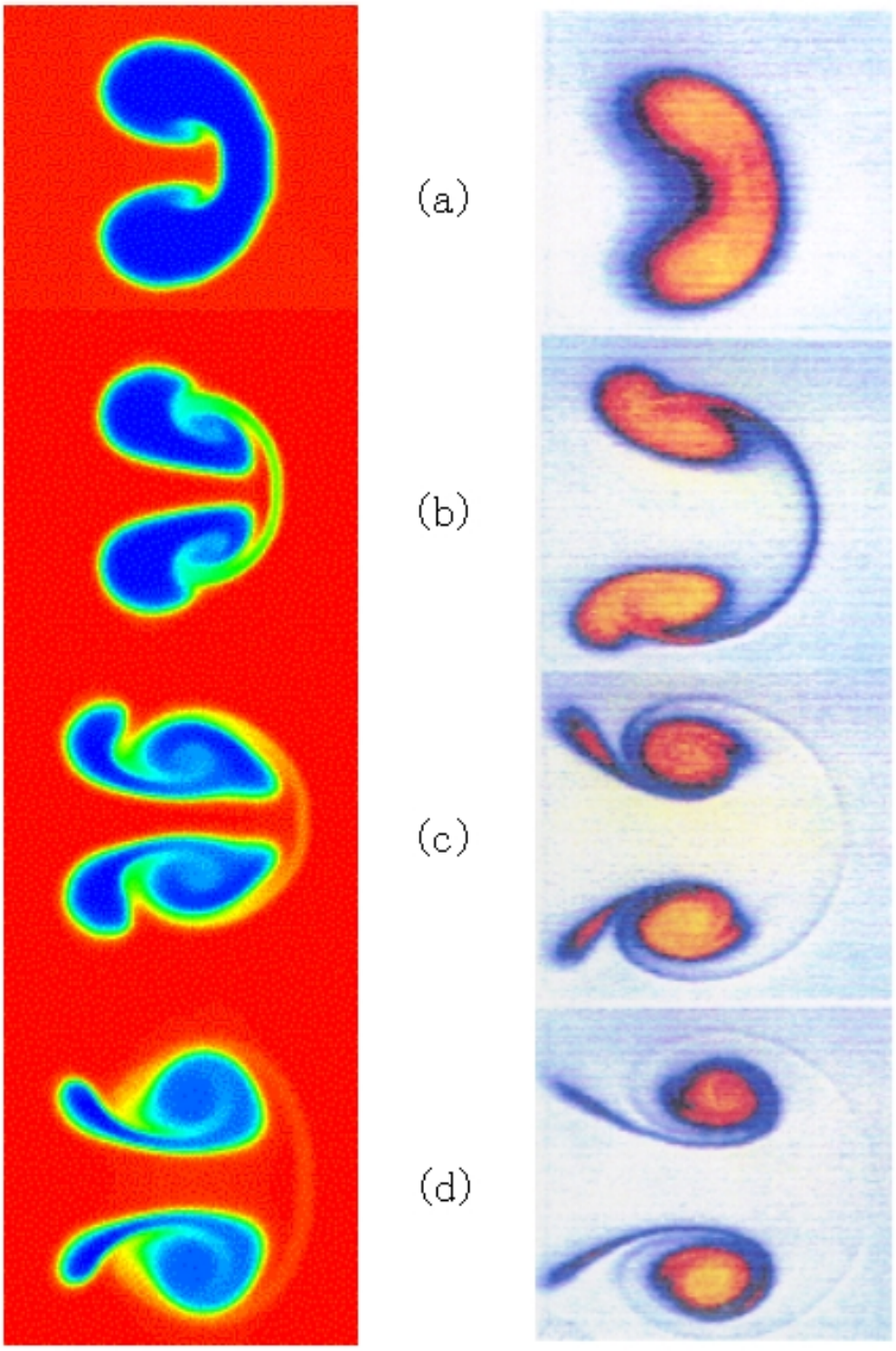


Figure 4.1: The comparisons of density contours at (a) $t = 123\mu s$, (b) $t = 373\mu s$, (c) $t = 573\mu s$, (d) $t = 773\mu s$. Left side --- CVC. Right side --- Experiment [10].

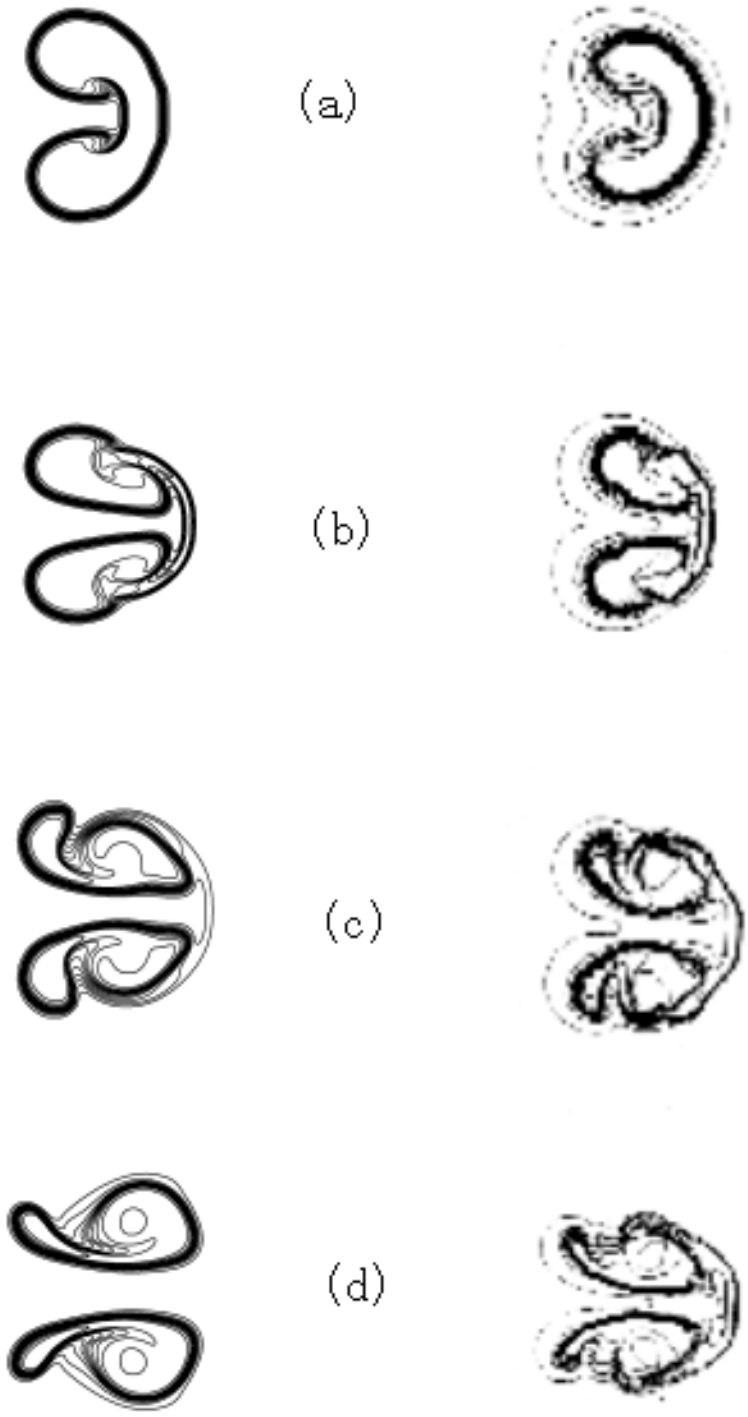


Figure 4.2: The comparisons of density contours at (a) $t = 123\mu s$, (b) $t = 373\mu s$, (c) $t = 573\mu s$, (d) $t = 773\mu s$. Left side --- CVC. Right side --- FCT [9].

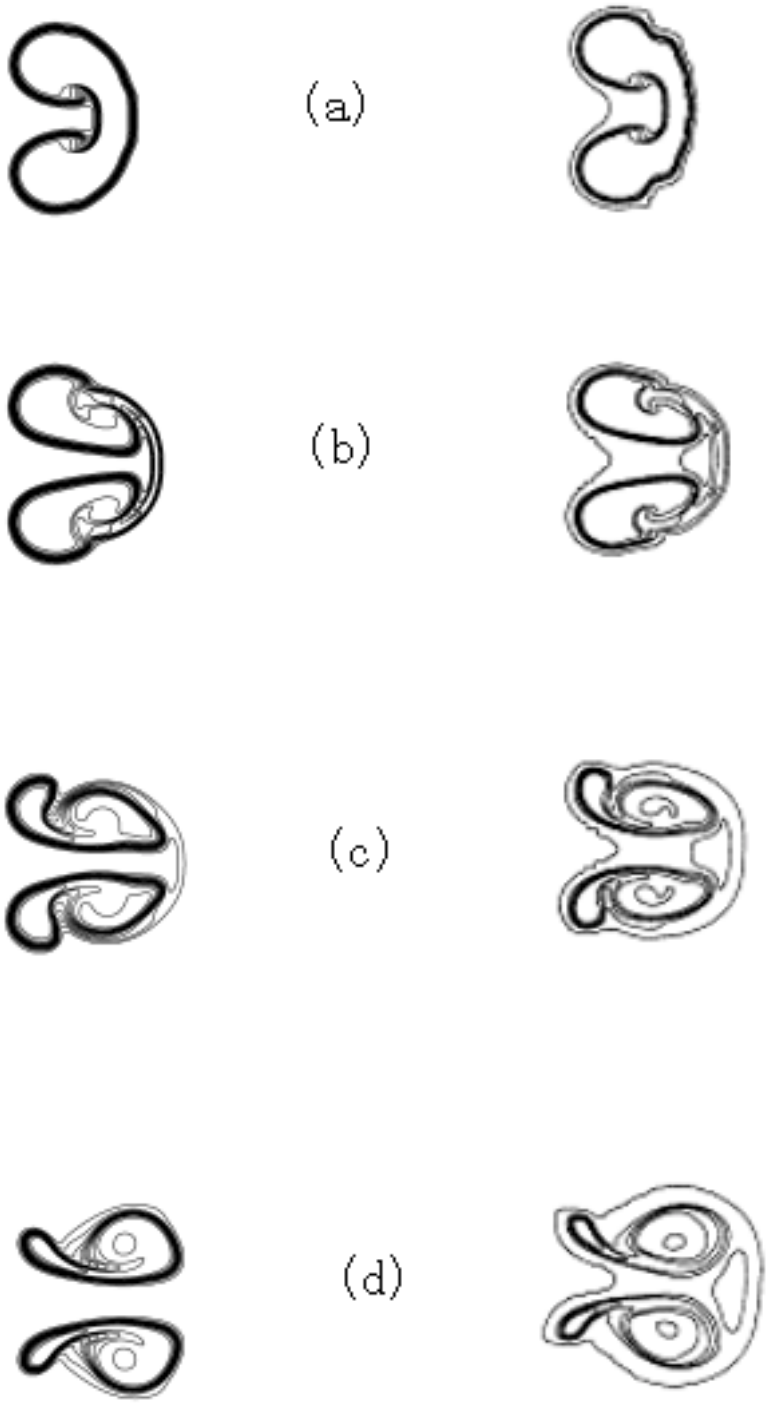


Figure 4.3: The comparisons of density contours at (a) $t = 123\mu s$, (b) $t = 373\mu s$, (c) $t = 573\mu s$, (d) $t = 773\mu s$. Left side --- CVC. Right side --- Adaptive Unstructured Algorithm [8].

## 4.3 Present Study for Shock-Vortex Interaction

Povitsky and Ofengeim [8] computed the problems of a moving shock over a circular vortex shown in Figure 4.4. The initial conditions for the vortex model used their study and in the present study can be written as follows:

$$u_\theta(r) = \begin{cases} U_c r / R_c, r \le R_c \\ Ar + B/r, R_c < r \le R_0 \end{cases}, \tag{4.1}$$

where

$$\left.\begin{aligned} A &= -\frac{U_c R_c}{R_0^2 - R_c^2}, \\ B &= \frac{U_c R_0^2 R_c}{R_0^2 - R_c^2}. \end{aligned}\right\} \tag{4.2}$$

The parameters used in the present study are listed bellow:

$$\left.\begin{aligned} &R_0 = 2R_c, \\ &\rho_l / \rho_h = 0.2, \\ &M_s = 1.5. \end{aligned}\right\} \tag{4.3}$$

The maximum tangential velocity $U_c$ of the circular vortex is 0.5 times the velocity behind the moving shock wave. This is one of the cases calculated by Povitsky and Ofengeim [8]. The computational domain is $40R_0 \times 20R_0$. The large height was used to try to minimize the channel effect.

First we performed the calculation with a fine grid $600 \times 200$. Two runs were carried out. One was completed without vorticity confinement; the other was completed with vorticity confinement. The basic solver was the finite-volume scheme with MDM [(2)] with the scalar confinement procedure described in Chapter 2. The dissipation parameter $E_d$ was set to 0.3. The confinement parameter $E_c$ was set to 0.005.

In this case we did not tuned the values of the parameters and just used the values of the calculation of the shock-bubble interaction because we believed that the initial conditions of the two cases were close to each other. Table 4.1 and Table 4.2 compare the pressure and density in the center of the three vortices of the present study without vorticity confinement and with vorticity confinement to that obtained using an unstructured adaptive algorithm [8]. It is well known that the lower the pressure and the density are, the stronger the vorticity will be in the center of the vortex if the ambient conditions are fixed.

Table 4.1: the pressure comparison ($p / p_{amb}$)

| | w/o CVC | | | w/ CVC | | | Adaptive Algorithm |
|---|---|---|---|---|---|---|---|
| Grid | 600x200 | 300x100 | 200x50 | 600x200 | 300x100 | 200x50 | unstructured grid |
| MV | 0.853 | 0.891 | 0.909 | 0.813 | 0.863 | 0.892 | 0.884 |
| SV1 | 0.915 | 0.949 | 0.955 | 0.898 | 0.920 | 0.943 | 0.920 |
| SV2 | 0.991 | 0.996 | 0.997 | 0.990 | 0.994 | 0.996 | 0.993 |

Table 4.2: the density comparison ($\rho / \rho_{amb}$)

| | w/o CVC | | | w/ CVC | | | Adaptive Algorithm |
|---|---|---|---|---|---|---|---|
| Grid | 600x200 | 300x100 | 200x50 | 600x200 | 300x100 | 200x50 | unstructured grid |
| MV | 0.274 | 0.400 | 0.482 | 0.268 | 0.316 | 0.476 | 0.244 |
| SV1 | 0.658 | 0.801 | 0.828 | 0.653 | 0.737 | 0.823 | 0.787 |
| SV2 | 0.845 | 0.978 | 0.984 | 0.787 | 0.972 | 0.978 | 0.917 |

Legend: MV --- Main Vortex; SV1 --- Secondary Vortex , No. 1; SV2 --- Secodary Vortex No. 2

Figure 4.5 shows the density contours and the maximum values of the vorticity in the core regions of the three vortices at $t = 421\mu s$ . The result with vorticity confinement has much stronger vorticity than the result without vorticity confinement. For example, the maximum vorticity with vorticity confinement at the core of the main vortex is the 1.44 times the one without vorticity confinement. The stronger the vorticity is in the core region of the vortex, the lower the pressure and the lower density are at the core region of the vortex under the circumstances when the ambient conditions are fixed. This observation is consistence with the comparisons between the pressure and density in Tables 4.1 and Table 4.2.

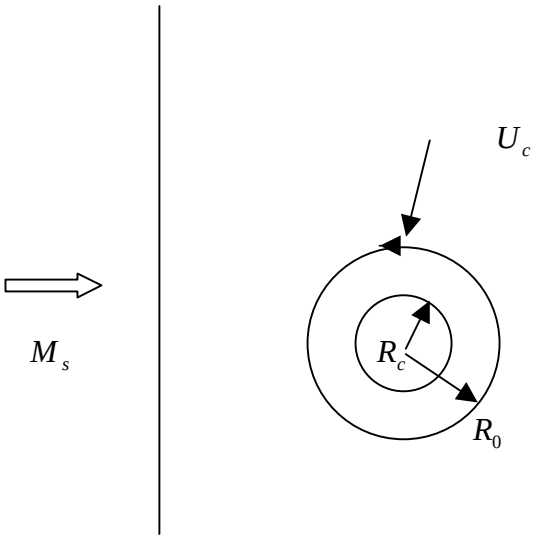


Figure 4.4: A moving shock over a circular vortex model.

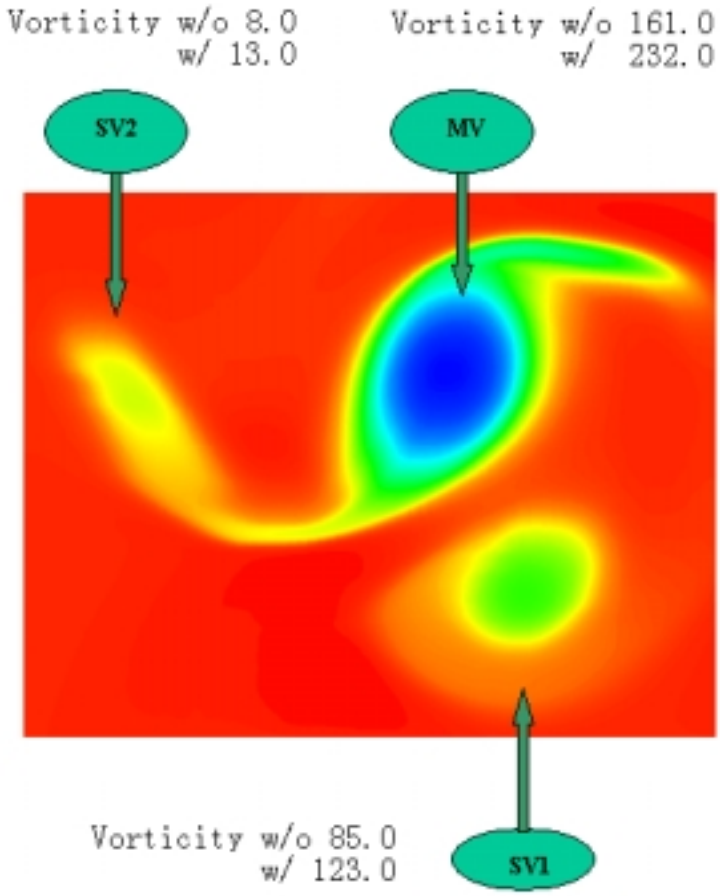


Figure.4.5: The density contours at 421 $\mu s$ .

Figure 4.6 shows the density contour comparisons between present results and the results calculated using complex adaptive unstructured algorithm by Povitsky *el al* [8]. The present result seems to be a duplication of that of Povitsky *et al.*.

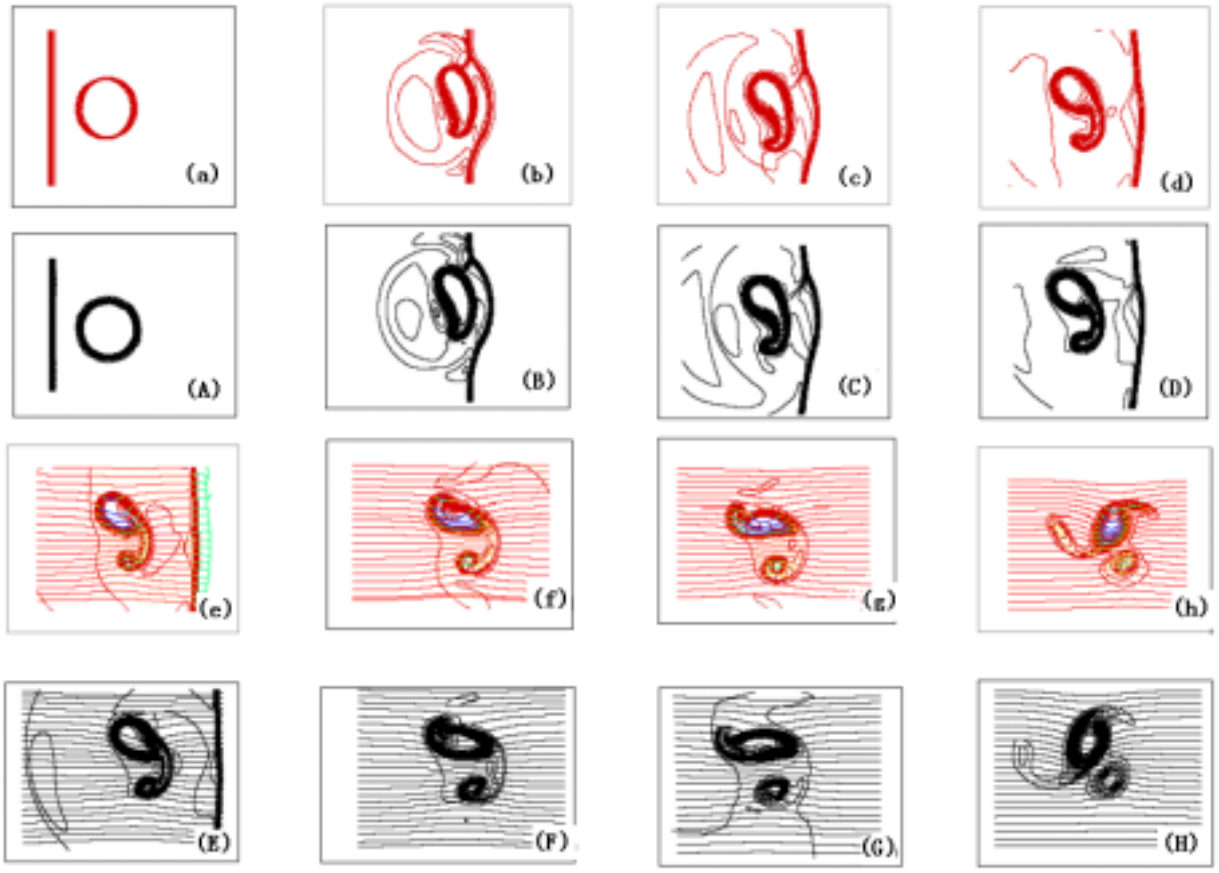


Figure.4.6: The density contours in the time interval 0 - 421 $\mu s$ .

(a, A) t = 0 $\mu s$ ; (b, B) t = 50 $\mu s$ ; (c, C) t = 70 $\mu s$ ; (d, D) t = 90 $\mu s$ ; (e, E) t = 110 $\mu s$ ; (f, F) t = 157 $\mu s$ ; (g, G) t = 203 $\mu s$ ; (h, H) t = 421 $\mu s$ .

a - h ---- CVC. A - H ---- adaptive unstructured algorithm by Povitsky *et al.* [8].

Next we consider how CVC works with coarser grids. We recalculated the shock-vortex interaction with two sets of coarser grids: 300x100 and 200x50. Figure 4.7 shows the comparison of the grids among the present grids and the adaptive grid used by Povitsky and Ofengeim [8] at two different times that

correspond to the time before shock-vortex interaction and the time after shock-vortex interaction. From the figure we see that the adaptive grid in the core region of the vortex and the region near the shock is much denser than the present grids, though the present grids in other regions are denser than the adaptive grid. Figure 4.8 presents the comparison of the density contours between the present results and the results obtained using an adaptive algorithm [8]. From this figure we see that the agreement is very good, though the result of the coarsest grid of the present study shows a little dissipation in the core region of the vortex and the region near the shock, but the solution captured the main vortex features such as the vortex roll up and pinch off. The result of the finest grid of the present study captured more details of the complicated vortex structure than the unstructured adaptive algorithm, although the grid in the core region of the vortex of the present study is coarser than the unstructured adaptive grid. In addition, the quantitatively comparisons of the pressure and the density in the center of the three vortices are presented in Table 4.1 and Table 4.2. From these tables we see that CVC works well with coarse grids.

## 4.4 Conclusion

Many modern CFD schemes, such as the FCT scheme used in present examples are high order finite-difference schemes which increase CPU loads. These schemes often contain mesh refinement algorithms and the adaptive unstructured grid algorithms which have complicated logic and are difficult to implement. Furthermore, an unstructured adaptive algorithm is CPU intensive, because many more grid points are embedded in the vicinity of the regions with steep gradients such as the vortex core and discontinuities. Also, if the problem solved is an unsteady problem, the time step is restrictive by the small adaptive grid cells and the computational grid needs to be reconstructed at beginning of each time step. In addition, grid adaptation is difficult to implement for complex flows in three dimensions. Compared with these methods, for vortex dominant flows, CVC is a robust numerical method which requires much less computation to achieve accurate results.

On the other hand, the CVC method has some drawbacks. In the calculation we observed that when very large values of the confinement parameter were used, such as $E_c = 0.4$ in the shock-vortex interaction problem, the structure of the vortical layer was broken down to many tiny vortices and the confinement procedure was not effective. The results under this circumstance are presented in Figure 4.9 and appear to be somewhat chaotic. Furthermore, from the point view of how CVC is constructed, the vorticity confinement works only in the vortical regions in which there exist strong vorticity gradients. For

example, in the calculations of shock-bubble and shock-vortex interaction, before and after interaction, near the region close to the shock wave, the vorticity gradient is small or equals to zero and the CVC method has little or no effect. Furthermore, from Figure 4.8 we see that when the grid size increases, the shock was diffused by the numerical dissipation. Therefore, the dissipation in shock region was not strongly affected by the confinement, because the CVC term in this region is very small or equals to zero. However, in the core region of the vortices, the edges of the vortices are still sharp when the grid size increases, because there exist strong vorticity and strong vorticity gradients and that the CVC term tends to balance the numerical dissipation.

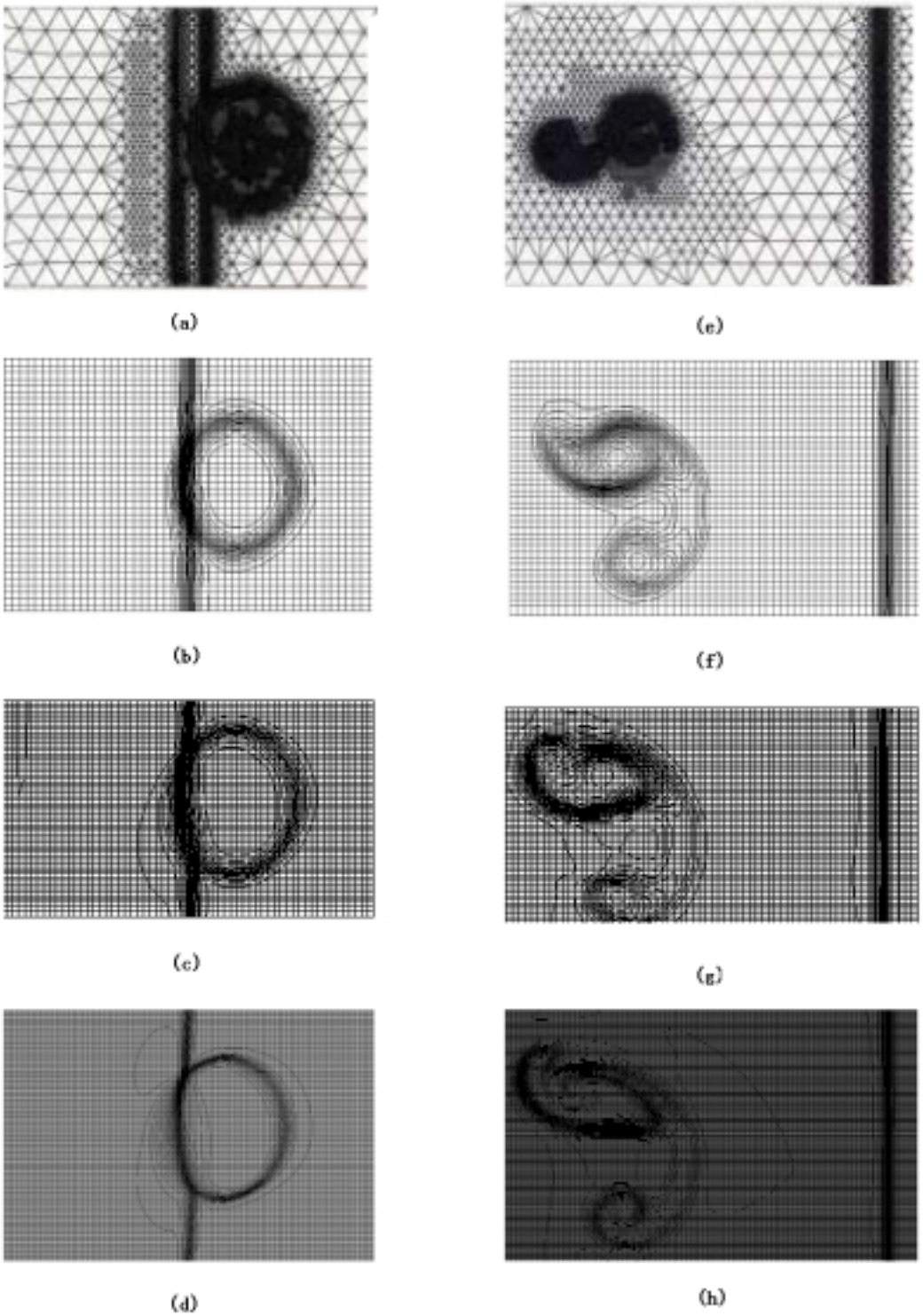


Figure 4.7: The comparison of the grids. (a), (e) the grid layout before and after interaction , unstructured adaptive grid [8]; (b), (f) the grid layout before and after interaction of the present study, 200x50; (c), (g) the grid layout before and after interaction of the present study , 300x100; (d), (h) the grid layout before and after interaction of the present study, 600x20.

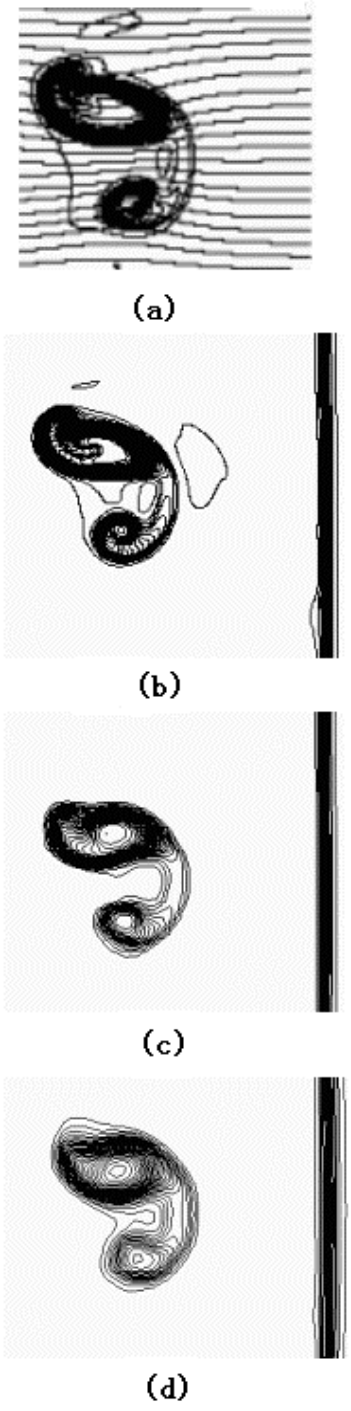


Figure 4.8: The comparison of density contours at time 157 $\mu s$ on different grids. (a) unstructured adaptive grid [8]; (b) regular Cartesian grid of the present study 600x200; (c) regular Cartesian grid of the present study 300x100; (d) regular Cartesian grid of the present study 200x50.

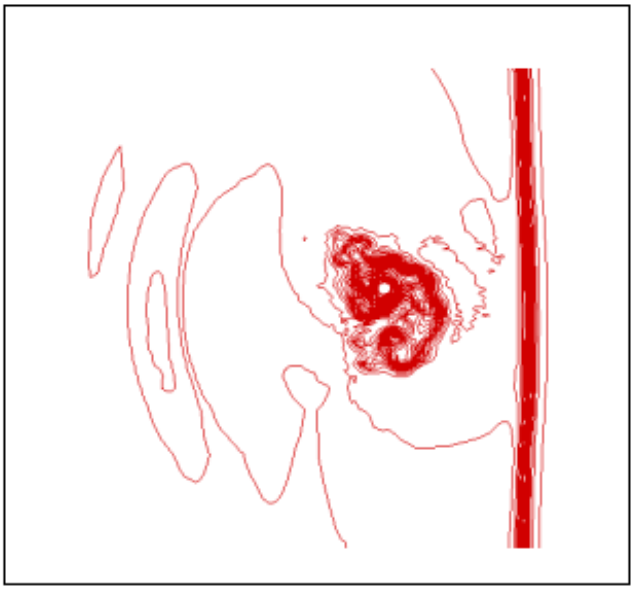

(a)

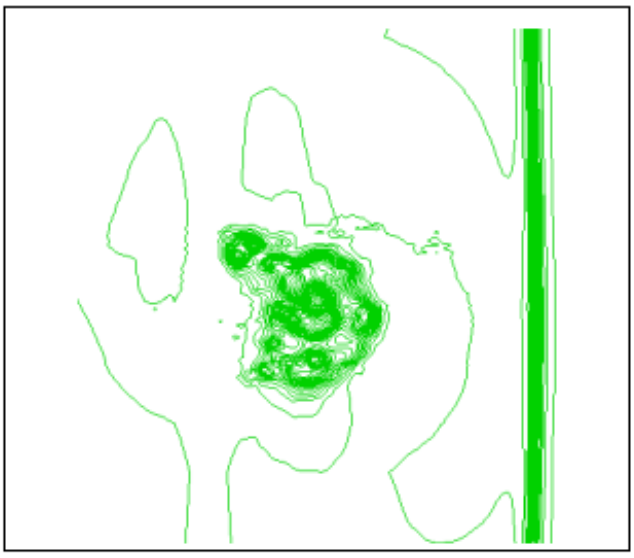

(b)

Figure 4.9: The density contours at (a) t = 90 $\mu s$ and (b) t = 157 $\mu s$ for the grid 200x50 and $E_c$ = 0.4.

# Chapter 5

# Calculations of Flows past Bluff Bodies

The study of the flows around bluff bodies is fundamental to the understanding of the mechanisms of complex 2D and 3D vortex-dominant flows. In this chapter the flows past a 2D square cylinder and a 3D cube mounted on the floor of a plate channel will be investigated; the qualitative and quantitative comparisons among Compressible Vorticity Confinement (CVC), Large Eddy Simulation (LES) and calculation of Reynolds-Average-Navier-Stokes (RANS) equations will be given, and finally some conclusions will be stated.

The purpose of these calculations is to test how CVC works with complex turbulent flows with massive separation past bluff bodies. We did these calculations to see how the value of the confinement parameter impacts the vortex shedding for the flow past a 2D square cylinder and what is the effects of CVC on the flow patterns of the massive separation of the flow past a surface-mounted cube. At the same time, we tested the drawbacks of the CVC method in the process of the calculations for these kinds of flows.

## 5.1 Introduction

The flows past a 2D square cylinder and a 3D cube produce many complex phenomena such as multiple separation, reattachment, unsteady vortex shedding, large-scale turbulent structures as well as bimodal behavior even for relatively simple geometries. Flows past bluff bodies are involved in many realistic engineering problems. Generally speaking, it is difficult to numerically simulate such flows because they are the most challenging problems in current CFD. The detailed experimental data for the flows around a 2D square cylinder and a 3D surface-mounted cube are available from Durao [3], Lyn *et al.* [49,50], and Larousse, Martinuzzi and Tropea [4,5]. Both cases are test cases that were computed by LES and RANS

calculations with various turbulence models and submitted to an LES workshop in 1996, so we can qualitatively and quantitatively compare the results calculated by CVC with that measured in experiments and the results calculated by using LES and RANS with various turbulence models.

In practical problems, the Reynolds numbers are very high. The values of viscous terms in Navier-Stokes equations are much smaller than that of the convection terms. We attempted to simulate those kinds of problems mentioned above using Euler equations. However, the boundary layer near the wall cannot be ignored because it is so important in vortex-dominant flows. So no-slip conditions were used in all our calculations to enforce the viscous flow boundary conditions on the wall. In most Euler calculations, if a no-slip wall conditions were imposed, an unreasonably thick boundary layer would develop because of the diffusive nature of the numerical algorithms. However, as we will show in Chapter 7, the CVC method produces a boundary layer that is a reasonable first approximation to a turbulent boundary layer in the near wall regions.

In the presents study, the time-dependent Euler equations were solved to get the instanteneous variables $(\rho, u, v, w, p)$. The accuracy for the calculations of complex vortex-dominant flows strongly depends on the method used, i.e., Franke and Rodi [14], and Bosh [51].

## 5.2 Calculation of a Flow past a 2D Square Cylinder

In the present study, an explicit fourth-order Runge–Kutta scheme was used for time discretization, and the finite-volume cell-centered scheme with a second-order matrix dissipation MDM $^{(2)}$ described in Chapter 2 was used to approximate the convection terms. The dissipation parameter $E_d$ was set to 0.3. The method used to choose the dissipation parameter has been discussed in Chapter 2, Chapter 3 and Chapter 4. The scalar confinement procedure with different values of confinement parameter $E_c$ was employed. The value of the vorticity confinement parameter was tuned according to the frequency of the vortex shedding and the velocity profile along the centerline of the square cylinder. The details will be discussed in the later part of this section. Furthermore, the parabolic approximation [52,53] was used to interpolate the primitive variables $(\rho, u, v, p)$ at cell centers to the cell faces where the numerical fluxes are evaluated.

The results for a flow around a 2D square cylinder will be given in this section. The detailed experiment data is available from Refs. [3,49,50]. There are two similar experiments referenced in the present study. One was done by Durao *et al*. [3]. The Reynolds number of this experiment was 14,000; the other experiment was done by Lyn *et al*. [49,50]. The Reynolds number of this experiment was 21,400. Rodi [13] and Murakami [54] reviewed the results of LES and RANS calculations with various turbulence models for flows past a 2D square cylinder. The calculation domain in the present study consists of 4.5 times the square cylinder dimension upstream, 14.5 times the square cylinder dimension downstream and 5.5 times the square cylinder dimension above and below the cylinder. The present calculation reproduced the vortex shedding. Figure 5.1 presents the comparisons of CVC, the experiment [49,50], RANS-RSM [14] and LES-UKAHY2 [13] calculations for streamline distributions at three phases and pressure, lift coefficient profile vs. non-dimensional time. It should be noted that the time scale of the present study is not the same as that of the experiment, but the non-dimensional frequency Strouhal number $S_t$ ($\frac{fH}{U_\infty}$, f is the shedding frequency, H is the dimension of the square cylinder and $U_\infty$ is the free stream velocity) obtained in the present study is very close to that measured in the experiment [3,49,50] if the value of the confinement parameter $E_c$ was set within prescribed range.

In the present study the free stream Mach number was 0.4; the flow. The non-dimensional vortex shedding frequency Strouhal number can be calculated as follows:

$$\begin{aligned} S_t &= fH/U_\infty = fH/(M_\infty a_\infty) = (n/(tt_r))H/(M_\infty a_\infty) \\ &= (n/(tH/a_\infty))H/(M_\infty a_\infty) \\ &= n/(tM_\infty), \end{aligned} \tag{5.1}$$

where t is the non-dimensional time interval, n is the number of vortex shedding in non-dimensional time *t*, $t_r$ is the reference time $H/a_\infty$, $M_\infty$ is the free stream mach number. In the calculations, the compressible Euler equations were solved with free stream Mach number 0.4. In the calculations we observed that the value of the confinement parameter played an important role to decide the vortex shedding frequency. No confinement produced the vortex shedding frequency that was smaller by 6 % - 13 % than the measured range in the experiments. As the value of the confinement parameter increased, the frequency of the vortex shedding increased which was within 1 % - 8 % of the measured range in the

experiments. However, when the value of the confinement parameter exceeded a value of $E_c = 0.005$, the vortex shedding frequency began to decrease, and when the value of the confinement parameter increased further to an extra large value, $E_c = 0.5$, no separation occurred, as a result, no vortex shedding occurred. The range of the appropriate values of the confinement parameter for this case with grid 100x90 can be found in Table 5.1. A sample lift coefficient profile is presented in Figure 5.1 from which we see that n is fallen into the range of 5 - 5.5 in non-dimensional time of 100, and as a result, the range of the $S_t$ number equals to 0.135 – 0.138, which is very close to the range measured in the experiment. From Eq. (5.1) we see that $S_t$ is only related to the free stream Mach number $M_\infty$ and number of vortices shedding n in non-dimensional time interval t. $S_t$ does not depend upon the Reynolds number, which is confirmed experimentally and with LES and RANS calculations. The computed drag coefficient and lift coefficient are defined as follows:

$$\left.\begin{aligned} C_D &= \frac{F_D}{\frac{1}{2}\rho_\infty V_\infty^2 H}, \\ C_L &= \frac{F_L}{\frac{1}{2}\rho_\infty V_\infty^2 H}, \end{aligned}\right\} \tag{5.2}$$

where $C_D$ is the drag coefficient, $C_L$ is the lift coefficient, $F_D$ is the drag force, $F_L$ is the lift force, $\rho_\infty$ is the free stream density, $V_\infty$ is the free stream velocity, and H is the dimension of the square cylinder.

In Table 5.1 various integral parameters (e.g. Strouhal number $S_t$, drag coefficient $C_D$, etc.) predicted with various computational methods are summarized with the experimental data. From Table 5.1 we see that vorticity confinement produced as good agreement with experiment as did the LES and RANS calculations. From the calculations we observed that $C_D$ increased as $E_c$ increased, because the base pressure decreases when $E_c$ increases. However, The drag coefficient without confinement was predicted smaller by 5 % - 17 % of the measured range of the experiments. In addition, $l_R$ decreased when $E_c$ increased, because vorticity confinement prevents the vortices from being diffused; so the length of the recirculation behind the cylinder will be shorten when $E_c$ increases. On the other hand, the length of the recirculation $l_R$ without confinement was predicted larger by 17 % of the measured one in the experiments. Furthermore, The vortex shedding frequency decreased when the value of the confinement parameter exceeded $E_c = 0.005$. As mentioned above, when an extra large value of the confinement parameter was used, for example, $E_c = 0.5$, no vortex shedding occurred. In Chapter 7, we will see how

the values of the confinement parameter change the velocity profile of the turbulent flow over a 2D flat plate. As a result, we suggest using $0.001 \le E_c \le 0.02$ for the calculation of the flow past a square cylinder. Over this range of values, the results are relatively insensitive to the values of $E_c$.

Table 5.1 shows that the LES calculations produced correct $C_D$ values in the range of experiments [49,50]. Some of the LES calculations yielded high and low Strouhal numbers; the reason is not clear. The RANS calculation with RSM produced very low $l_R$, but the $k-\varepsilon$ model with Kato-Launder (KL) modification ($KL-k-\varepsilon$) [51] and the RGN $k-\varepsilon$ model [55] yielded correct value of $l_R$ compared with the experiment of Lyn [49,50] and Durao [3]. The $KL-k-\varepsilon$ model produced smaller $C_D^{'}$ and $C_L^{'}$ than LES and CVC. However, the RNG $k-\varepsilon$ model and *TL-RSM* calculations [14] produced similar $C_D^{'}$ and $C_L^{'}$ to LES and CVC.

The time average velocity U along the centerline of the square cylinder is presented in Figure 5.2. The results of the CVC, LES, RANS and experimental data due to Lyn [49,50] and Durao [3] are included. From that figure we see that there are large differences in the wake region for the two experimental results and computed results with different numerical methods. There could be two reasons that cause the large difference of the recovery behavior behind the square cylinder between the two experiments. One reason could be the different Reynolds numbers in the two experiments (the Reynolds number of Durao's experiment was 14,000; the Reynolds number of Lyn's experiment was 21,400). We may speculate that the other reason could be associated with problems in Lyn's experimental data. We note that the other experiment [3] and all the computational results but just one LES result show faster recovery of the wake behind the cylinder compared with the Lyn's data [49,50].

From Figure 5.2, we see that the $KL-k-\varepsilon$ model with the wall function [51] over-estimated the length of the reverse flow region behind the cylinder. The two LES calculations [13] under-estimated the length of the separation region behind the cylinder. Furthermore, The two LES calculations showed surprisingly large differences both in terms of the separation region and the recovery behavior. The LES-KAWAMU calculation [13] showed an unrealistic slope of U at larger x values and produced very slow recovery. The *TL-RSM* result [14] showed a separation zone that was too short, and negative velocity that was considerably too small. Finally, we can conclude that CVC showed better agreement with the experiments than RANS and LES calculations in the prediction of velocity and separation zone for the flow past a 2D square cylinder.

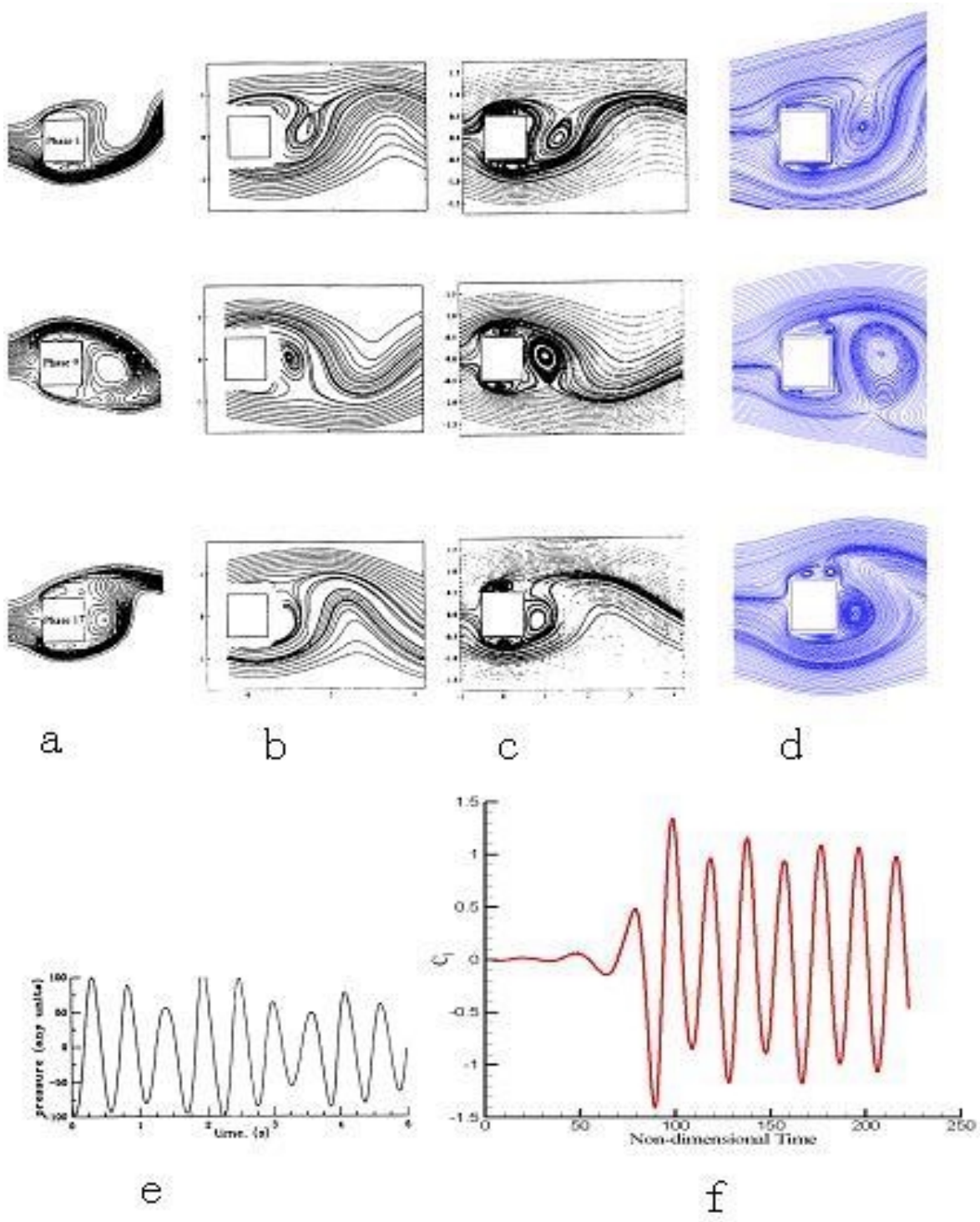


Figure 5.1: Streamline distributions at three phases and time variation of pressure and lift coefficient for a flow past a 2D square cylinder; a, e – experiments of Lyn *et al.* [49,50], b -- RANS-RSM of Franke *et al.* [14], c -- LES-UKAHY2 of Rodi [13], d, f – CVC.

Table 5.1: the comparisons of integral parameters for a flow past a 2D square cylinder

| Method | $C_D$ | $C_D$' | $C_L$' | $l_R$' | $S_t$ | Grid |
|---|---|---|---|---|---|---|
| Basic Solver ($E_c$ = 0.0) | 1.82 | 0.35 | 1.25 | 1.76 | 0.130 | 100x90 |
| CVC ($E_c$: 0.001- 0.02) | 2.1- 2.68 | 0.1-0.7 | 2.0-2.3 | 1.3-1.7 | 0.135–0.138 | 100x90 |
| LES: | | | | | | |
| Murakami [54] | 2.09 | 0.13 | 1.6 | | 0.132 | 104x69x10 |
| KAWAMU [13] | 2.58 | 0.27 | 1.33 | 1.68 | 0.15 | 135x78x20 |
| UMIST2 [13] | 2.02 | | | 1.21 | 0.09 | 140x81x13 |
| RANS: | | | | | | |
| $KL-k-\varepsilon$ WF [51] | 1.79 | 0.013 | 0.614 | 2.04 | 0.142 | 100x76 |
| RNG $k-\varepsilon$ [56] | 2.13 | 0.23 | 2.08 | | 0.133 | |
| TL-RSM WF [14] | 2.15 | 0.27 | 1.49 | 0.98 | 0.136 | 70x64 |
| Exp. [49,50] | 1.92 – 2.2 | | | 1.38 | 0.138 – 0.136 | |

Legend: $C_D$ --- the time average of the drag coefficient, $C_D$' --- the amplitude of the fluctuation of the drag coefficient. $C_L$' --- the amplitude of the fluctuation of the lift coefficient $C_L$, $l_R$ --- the length of the recirculation zone behind the cylinder, $S_t$ --- Strouhal number, WF --- the wall function.

Figure 5.3 presents the comparisons of the mean pressure along the surface of the square cylinder among the experimental data [49,50,56], CVC, LES and RANS calculations. Again we note that there are discrepancies between the two experimental data, which may be caused by the different experimental conditions (the Reynolds number of Lyn's experiment was 21,400, and the Reynolds number of Bearman's experiment was 20,000). The result without confinement and result of RGN $k-\varepsilon$ model show agreement with Lyn's experimental data [49,50] on the sidewall of the square cylinder, while both CVC and LES calculations obtained agreement with Bearman's experimental data [56]. However, we have shown earlier that the vortex shedding frequency with and without confinement is different.

Next, we consider the grid effect on the calculation for the flow past a 2D square cylinder. Firstly, a very coarse grid (25x25) was used, but no vortex shedding was produced. When very coarse grids are used,

the vortices in the forward corner cannot be formed, so no vortex shedding results. In this situation, vorticity confinement cannot help because vorticity confinement lets the velocity profile get fuller than without confinement, and no vortices are formed in the forward corners. As a result, no vortex shedding occurs. When the grid gets finer, the vortex shedding can be produced, but the overall good agreement for the flow cannot be obtained unless the grid gets finer. Table 5.2 presents the comparison of the results of two different sets of grids for the flow past a 2D square cylinder.

From Table 5.2 we see that for the coarser grid, the vortex shedding frequency is closely produced; the amplitudes of the drag and lift coefficient fluctuations are also good. However, the length of the recirculation zone is a little shorter than the experimental one, and the drag coefficient is much higher than that of the experiment. If we compare the results with the results of RANS calculation and some LES results presented in Table 5.1, the result for the coarser grid (50x50) would be reasonable. When the grid gets finer, 100x90, the computed overall flow field is even better. Therefore, as the grid size is changed, some characteristic parameters such as the vortex shedding frequency do not change, but the other characteristic parameters such as the drag coefficient are affected. Overall, the fine grid CVC computation produces results as good as state of the art LES calculations on much finer grids.

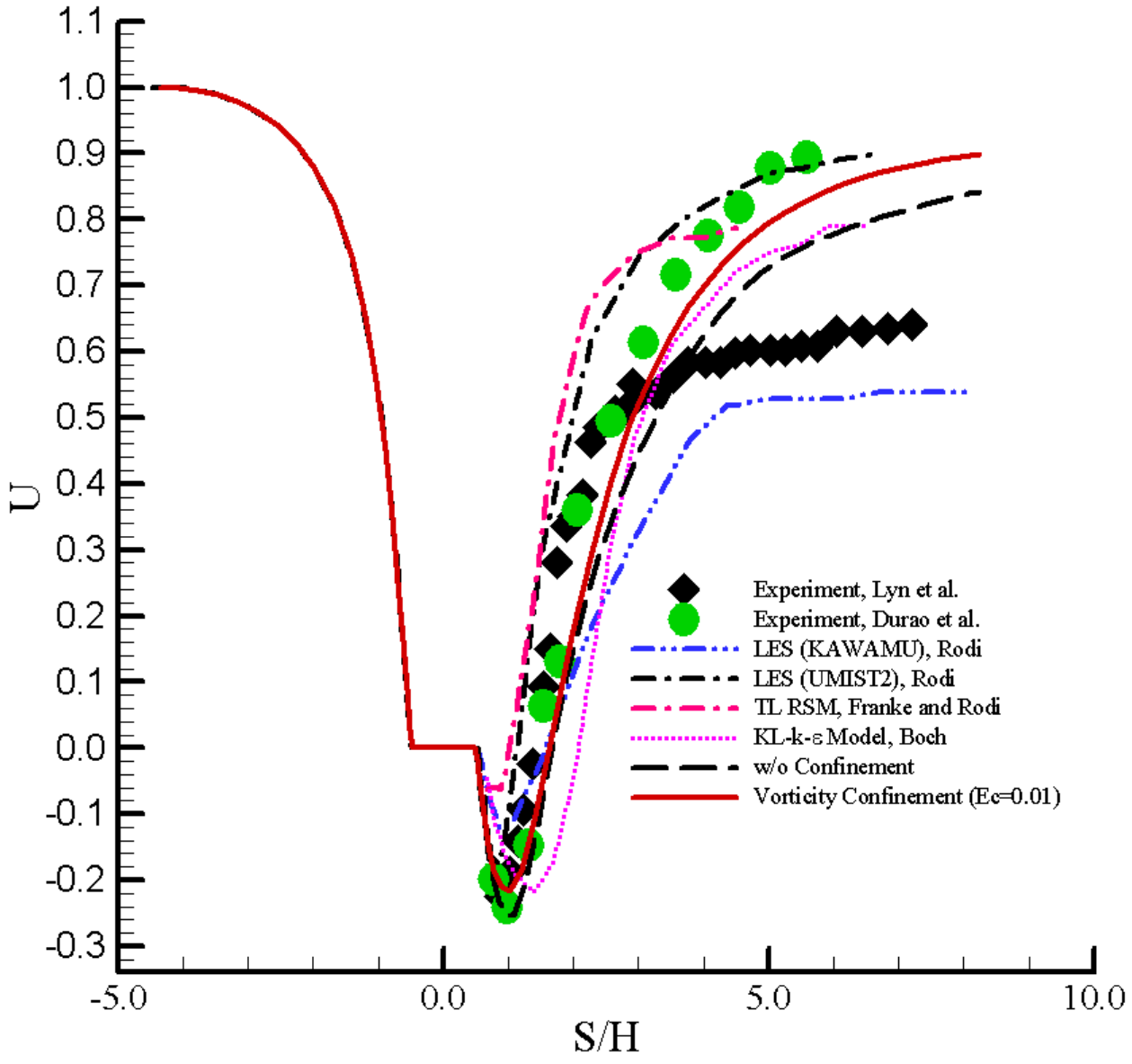


Figure 5.2: Time average-velocity U along the centerline of a 2D square cylinder

Table 5.2: the comparisons of the integral parameters for the two different sets of grids for the flow past 2D square cylinder.

| Method | $C_D$ | $C_D'$ | $C_L'$ | $l_R$ | $S_t$ | *Grid* |
|---|---|---|---|---|---|---|
| CVC (Ec = 0.005) | 2.41 | 0.135 | 1.25 | 1.49 | 0.138 | 100x90 |
| CV C (Ec = 0.005) | 3.13 | 0.500 | 2.51 | 1.21 | 0.130 | 50x50 |

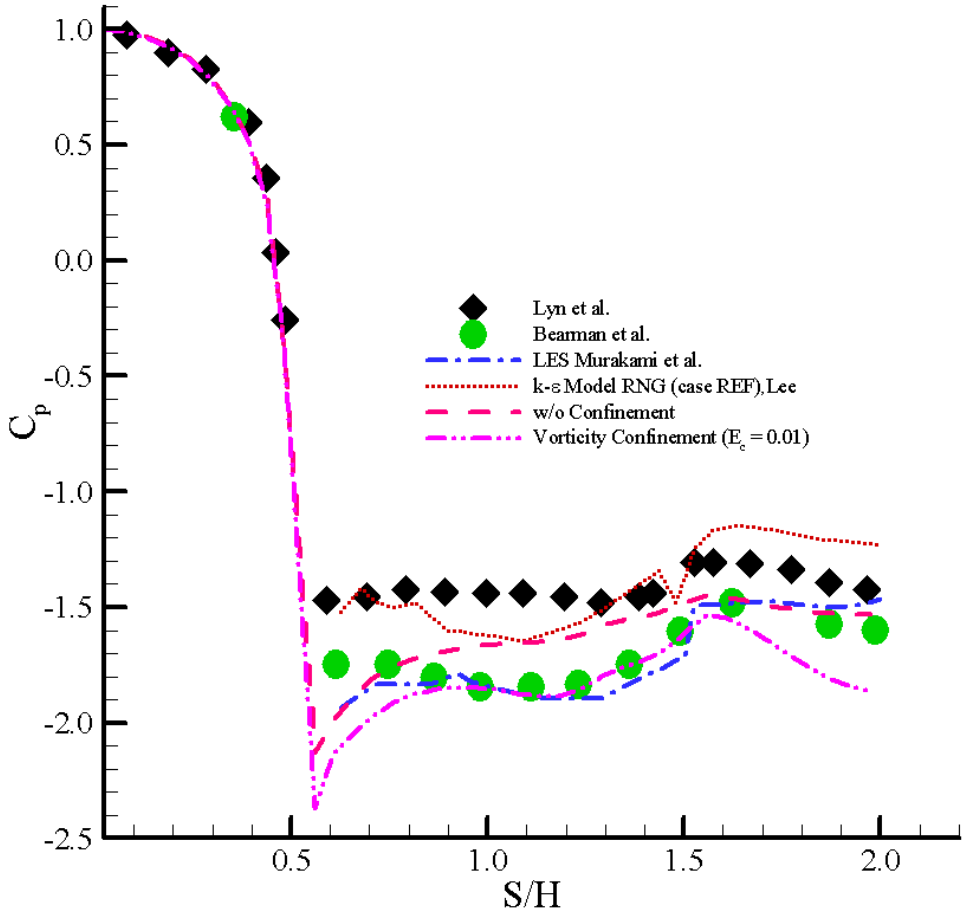


Figure 5.3: The mean pressure on the surface of a 2D square cylinder.

## 5.3 Calculation of a Flow Over a Surface-Mounted Cube in a Plate Channel

The flow pattern past a surface-mounted cube on the floor of a plate channel has a very complicated nature in spite of the simple geometry. The flow involves multiple separation at different locations including the front corners on the roof, the sidewall and in front of the cube. According to the flow patterns sketched in Figure 1.3f [4,5], the main separation vortex and secondary ones were formed in front of the cube. The main vortex is bent as a horseshoe vortex and convects down stream into a wake around the cube with converging-diverging characteristics. Directly downstream of the leading edge on the two sides of the cube, two corner vortices are formed at the junction of the channel floor and base of the cube, extending downstream to the corner vortices after the cube. These vortices join at the symmetry plane to form a closed arch behind the cube. The interactions among the horseshoe vortex, the corner vortices behind the cube and the impinged mixing-layer in the wake dominate the flow structure for the flow around the cube. The separation in front of the cube is characterized by bimodal behavior. That is, in one mode, high-inertia fluid is deflected back upstream in the form of jet by the front wall. This part fluid travels against the pressure gradient and rolls up to form up to four vortices. In the other mode, the other part of the fluid goes downstream around the cube and forms a horseshoe vortex.

We attempted to simulate the flow past a surface-mounted cube in the plate channel with a coarse Cartesian grid 32x24x24. 32 grid points were distributed within ten times of the cube dimension in the free stream direction; 24 grid points were arranged within 7 and 2 times cube dimension in the span-wise and lateral direction, respectively. The cube was located at the center of the computational domain. In order to get enough resolution near the floor of the channel and the cube wall, the grid was stretched and clustered near the floor of the channel and the cube wall. After 3-5 grid lines were stretched, the rest of the grid lines were distributed uniformly. The grid lines are stretched according to the following formulation:

$$x_i = x_{i-1} + \alpha(x_{i-1} - x_{i-2}), \tag{5.3}$$

where $i$ is the index in one of the Cartesian coordinates. In the present study, the value of the ratio $\alpha$ was 1.15 - 2.2, which was chosen in such a way that the grid lines were distributed as smoothly as possible. The distance between the first grid line to the floor and the wall of the cube was 0.03 in the present study. The grid on the symmetry plane is presented in Figure 5.4. A 1 / 6 power law of the velocity profile with

the maximum velocity value located at the center of the channel was used as the inlet boundary condition. The convection boundary condition was used at the exit of the domain. The pressure at the exit boundary was extrapolated from the closest interior points. No-slip boundary conditions were used on the wall of the cube and the floor of the channel where the pressure is the only contribution to the numerical flux. A parabolic approximation was used to get the pressure at boundary points from the closest interior points. The cell-centered finite volume central-difference scheme was used with Cartesian velocity components. In order to obtain oscillation-free solution, the matrix dissipation model MDM [2] described in Chapter 2

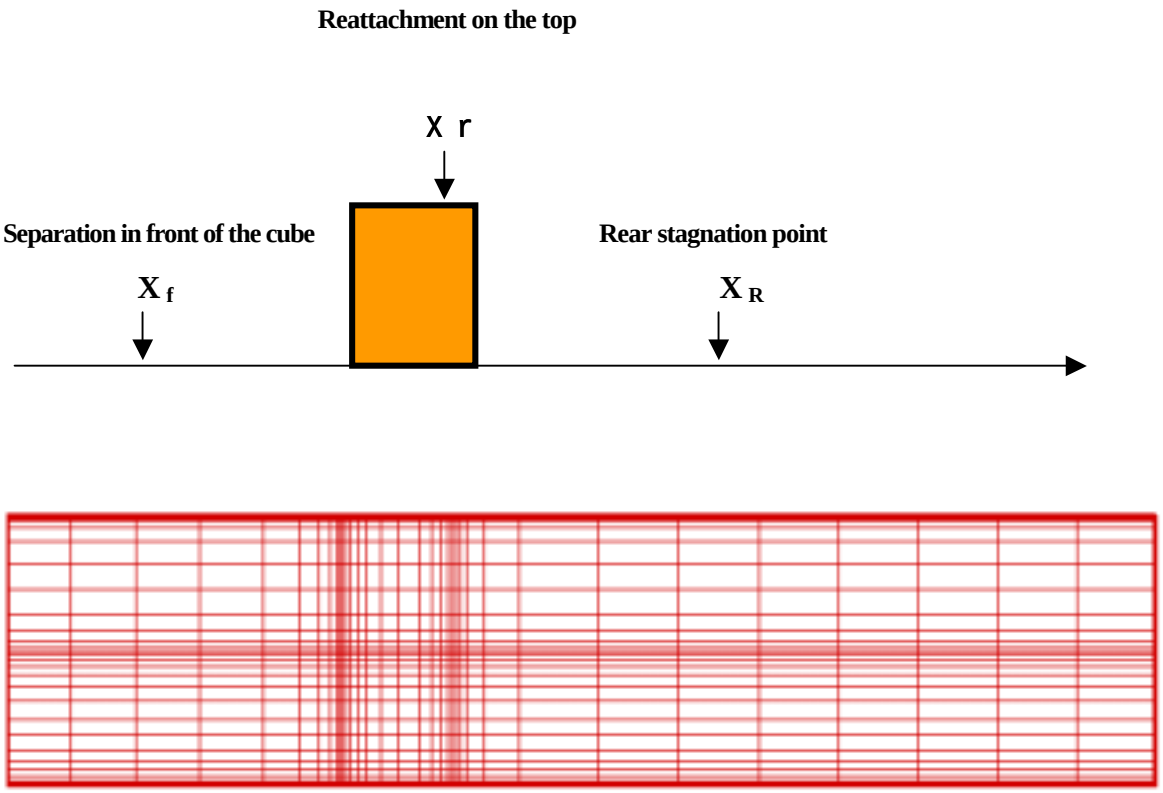


Figure 5.4: The grid layout on the symmetry plane of a cube.

was used. The dissipation parameter $E_d$ was the standard value 0.5. The value of the confinement parameter is set to 0.02, which was the value tuned for the calculation of the flow past a 2D square cylinder. The primitive variables $(\rho, u, v, w, p)$ at the face of grid cell are needed to evaluate the flux and

the dissipation matrix. The parabolic interpolation [52,53] for primitive variables was used to calculate the values at either side of the cell interface. After averaging the two values we get the values of the primitive variables at the cell interface. We also used a limiter (presented in Chapter 2) to prevent oscillations.

Figure 5.5 presents the streamline comparisons on the symmetry plane and near the floor of the channel among CVC, LES, RANS calculations [13] and the experiments [4,5]. The time-averaged streamlines are presented for experiment and LES. The streamline distribution calculated by vorticity confinement and LES [57] on a plane parallel to the back face of the cube at 0.1 step size of the cube dimension are compared in Figure 5.6. Various separation lengths defined in Figure 5.5 are summarized in Table 5.3. The present calculated length of the separation zones in front of the cube and behind the cube and the thickness of the separation zone on the roof of the cube are close to the experimental ones. From the Figure 5.5, Figure 5.6 and Table 5.3 we see that the complicated vortex-dominant flow around the cube was simulated very well using vorticity confinement. On the other hand, the standard $k-\varepsilon$ model with the wall function predicted the primary front separation point ($X_f$) too close to the cube while the $TL-k-\varepsilon$ model gives good agreement with the experiment for $X_f$. The $k-\varepsilon$ model with wall function produced a much short separation region with unrealistic reattachment on the roof. When the KL modification is used in the $k-\varepsilon$ model, a much longer separation region on the roof is produced with no

Table 5.3: the comparisons of the global parameters between the preset study and the Ref. [13] for the flow around a surface-mounted cube

| Method | Key | $X_f$ | $X_r$ | $X_R$ | Grid |
|---|---|---|---|---|---|
| CVC | | 0.98 | | 1.52 | 32x24x24 |
| LES [13] | UKAHY3 Smag. | 1.29 | | 1.70 | 165x65x97 |
| LES [13] | UKAHY4 Dyn. | 1.00 | | 1.43 | 165x65x97 |
| LES [13] | UBWM2 Smag. | 0.81 | 0.837 | 1.72 | 144x58x88 |
| RANS [13] | $Std-k-\varepsilon$ WF | 0.65 | 0.43 | 2.18 | 110x32x32 |
| RANS [13] | $KL-k-\varepsilon$ WF | 0.64 | | 2.73 | 110x32x32 |
| RANS [13] | $TL-k-\varepsilon$ | 0.95 | | 2.68 | 142x84x64 |
| Exp. [4,5] | | 1.04 | | 1.61 | |

Note: The Reynolds number in the experiments [4,5] is about $10^5$.

reattachment, but the separation bubble is still too thin compared with the observation in the experiment [4,5]. The *KL* version $k-\varepsilon$ model produced a longer separation region on the roof. The $k-\varepsilon$ Model with TL approach and *KL* modification gave better agreement with the measured in the experiment on the roof region, but the center of the bubble moved to too far down stream. All RANS calculations with $k-\varepsilon$ model predicted a separation zone behind the cube that was too long. The standard $k-\varepsilon$ model with the wall function produced about 35 $^{0}/_{0}$ longer separation zone behind the cube than the experimental one. The $k-\varepsilon$ model with the *TL* and *KL* modifications enlarged $X_R$ further, giving the most excessive length 110 $^{0}/_{0}$ longer separation zone behind the cube than that measured in the experiment. The CVC and LES clearly did a better job. Vortex shedding from the sidewall of the cube was observed in experiments [4,5]; such vortex shedding can contribute greatly to the momentum exchange in the wake and therefore can significantly shorten the separation zone behind the cube. Even though there was no clear vortex shedding found in CVC and LES calculations [13], the resolution of large scale unsteady vortical motions seems to produce the correct effect.

Figure 5.5 shows that the horseshoe vortex is generally produced quite well by the different methods. LES calculations and $TL-k-\varepsilon$ model captured the converging-diverging behavior of horseshoe vortex, but CVC and the $k-\varepsilon$ model with the wall function did not produce this feature. CVC predicted the correct separation length behind the cube, but the $TL-k-\varepsilon$ model produced the separation length that was too long.

Figure 5.6 shows that both CVC and LES calculations captured the strong vortical motion associated with the horseshoe vortex and its interaction with the corner vortices behind the cube. In our calculation, we found that horseshoe vortex center moves upward away from the floor of the channel in the down stream direction.

Figure 5.7 presents the comparison of the streamline distributions on the floor of the channel between confinement and without confinement. The solution without confinement did not captured the corner vortices behind the cube. Figure 5.8 presents the comparison the streamline distribution on a plane parallel to the back face of the cube and at 0.1 step size of the dimension of the cube. The solution without confinement captured the horseshoe vortex very poorly.

Figure 5.9 shows the comparison among CVC, LES [58] and the experiment [4,5] for the vertical profiles of mean velocity component U at several locations on the symmetry plane. The results with confinement show slighter better agreement with experiment than LES [58] on the roof region, and similar agreement wit LES downstream of the cube. Although the results without confinement for the velocity profile on the roof region are reasonable, the results elsewhere as shown in Figures 5.7 - 5.8 indicate poor agreement.

Next we consider the grid effect for the calculation of the flow past the 3D surface-mounted cube. A finer grid 51x35x40 was used. Figure 5.10, Figure 5.11 and Figure 5.12 present the comparison of the streamline distributions calculated with two sets of grids on a plane parallel to the back face, on the floor of a channel and on the symmetry plane. From these figures we see that the results with the finer grid are generally qualitatively closer to the experimental results and the computed results of LES. From the streamline distributions on the floor we see that the results of the finer grid displayed the converging-diverging behavior of the horseshoe vortex, but the result of the coarser grid just has a simple pattern. The streamline distribution with the finer grid on the plane parallel to the back face is much closer the flow pattern computed using LES. Furthermore, from the streamline distributions on the symmetry plane, we see that the separation bubble on the top of the cube for the finer grid is larger than that of the coarser grid. The velocity profiles on the symmetry plane are presented in Figure 5.13. This figure quantitatively compares the two computed results of CVC with two different grids to the experimental results and the computed results of LES. From this figure we see that the velocity profiles of the finer grid are much closer to the experimental results in the near wall region. This is the result of more grid points arranged in the boundary layer. However, the profile in the core region does not seem to improve and degrades slightly. This behavior may be explained by the computed results of the flow over a 2D flat plate using CVC in Chapter 7.

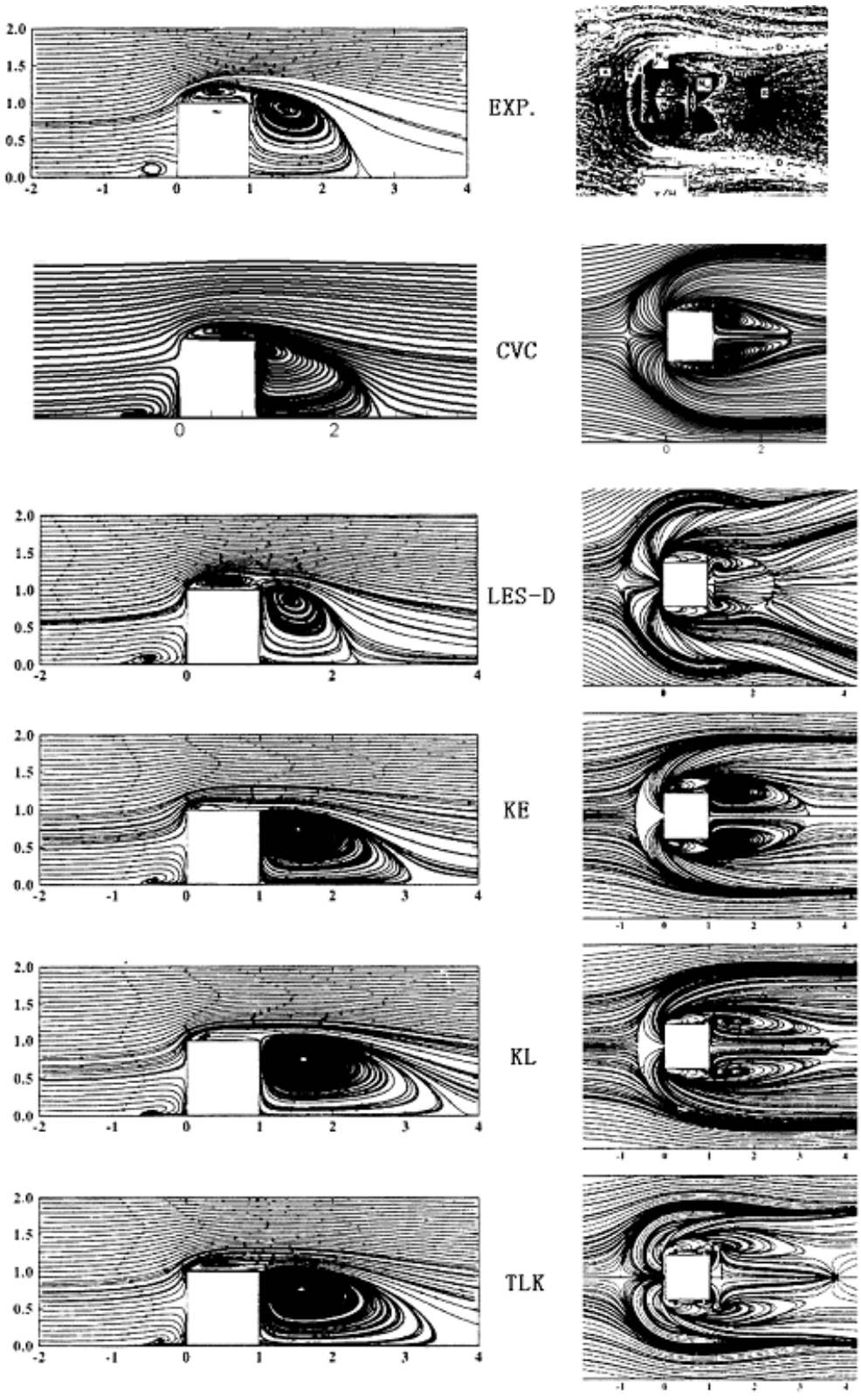


Figure 5.5: The comparisons of the streamline distributions on the symmetry plane and on the floor of the channel. All the results but CVC are from Rodi [13].

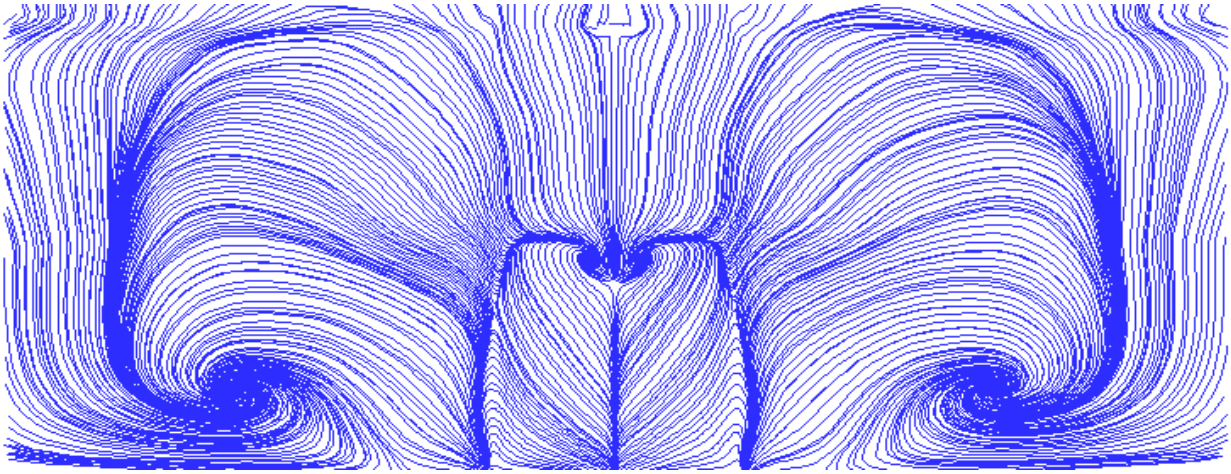

CVC

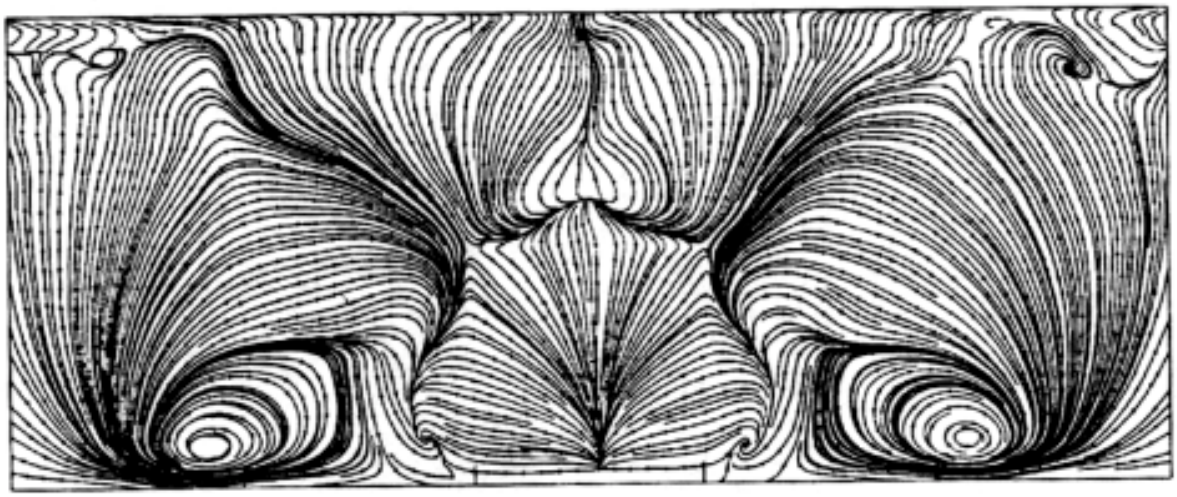

LES [57]

Figure5.6: The comparisons between CVC and the LES calculation [57] for the streamline distributions on the plane parallel to the back face at 0.1step size of the cube dimension.

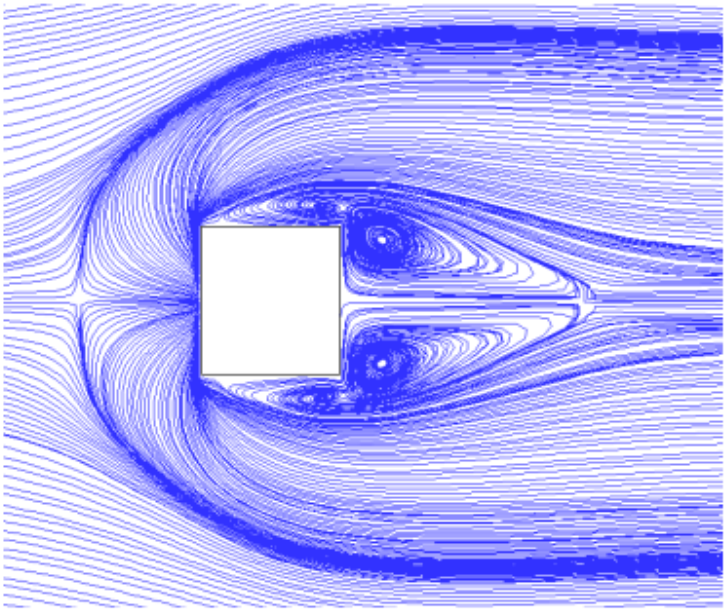

With CVC

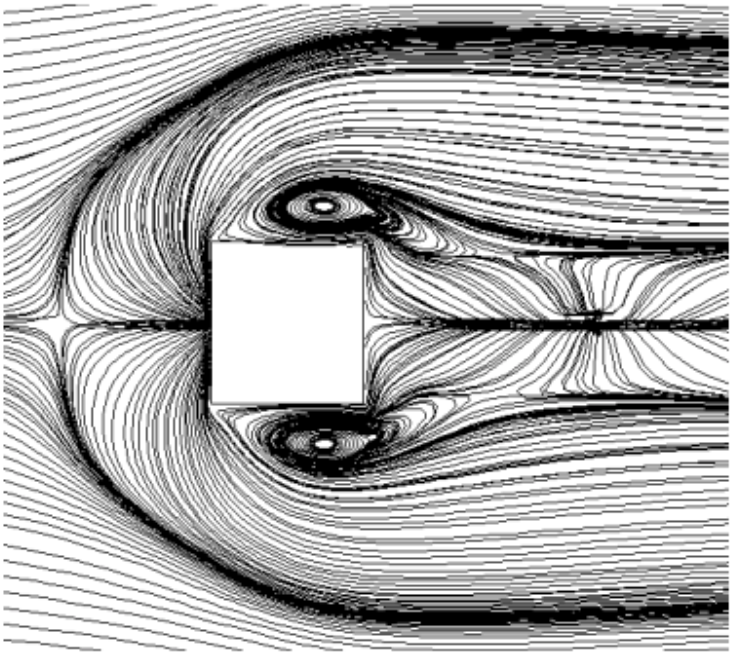

Without CVC

Figure 5. 7: Comparison of the streamline distributions with and without CVC on the plane near the floor of the channel. Grid 32x24x24.

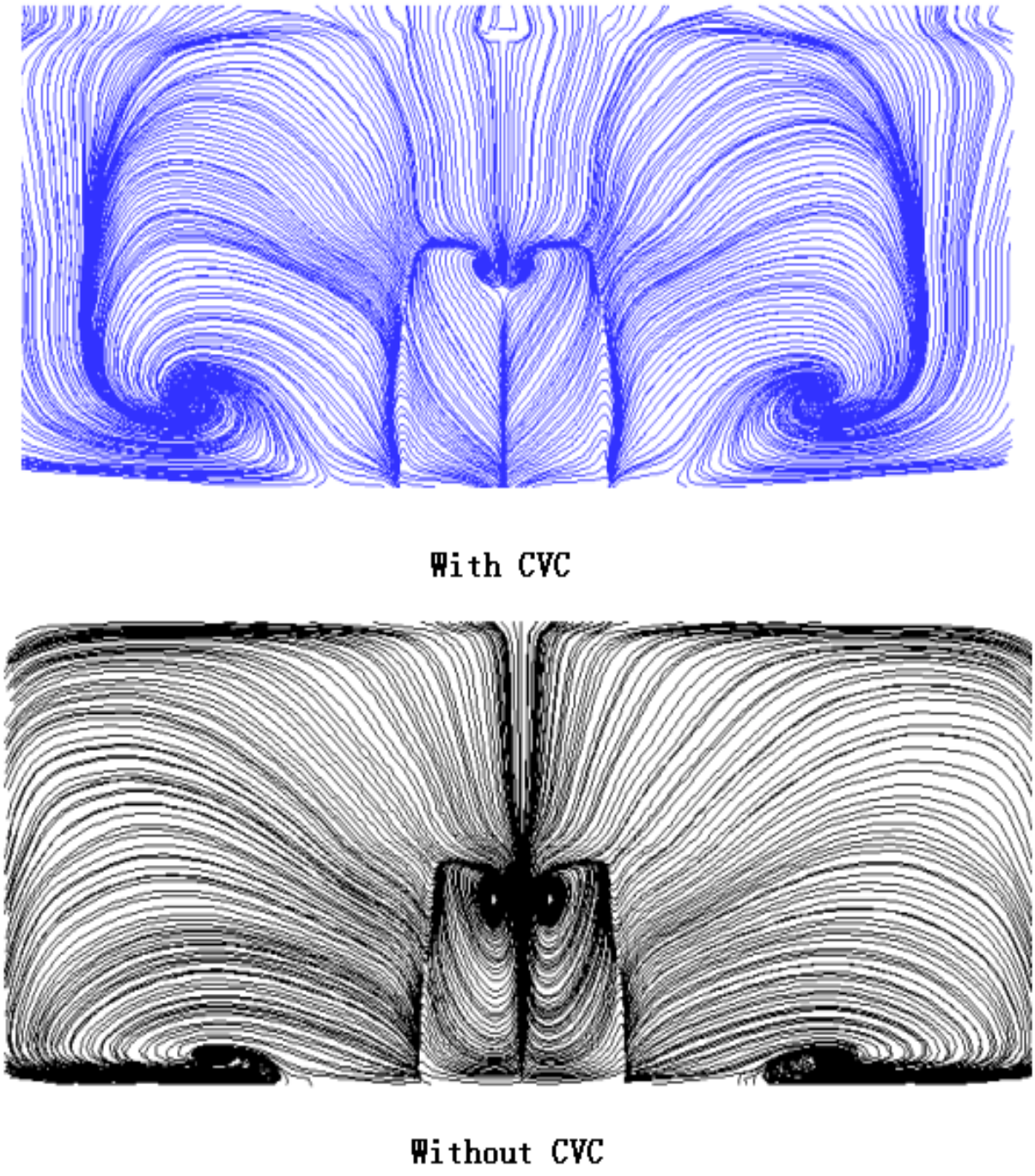


Figure 5. 8: Comparison of the streamline distributions with and without CVC on the plane which is at 0.1 step size of the dimension of the cube and parallels to the back face of the cube. Grid: 32x24x24.

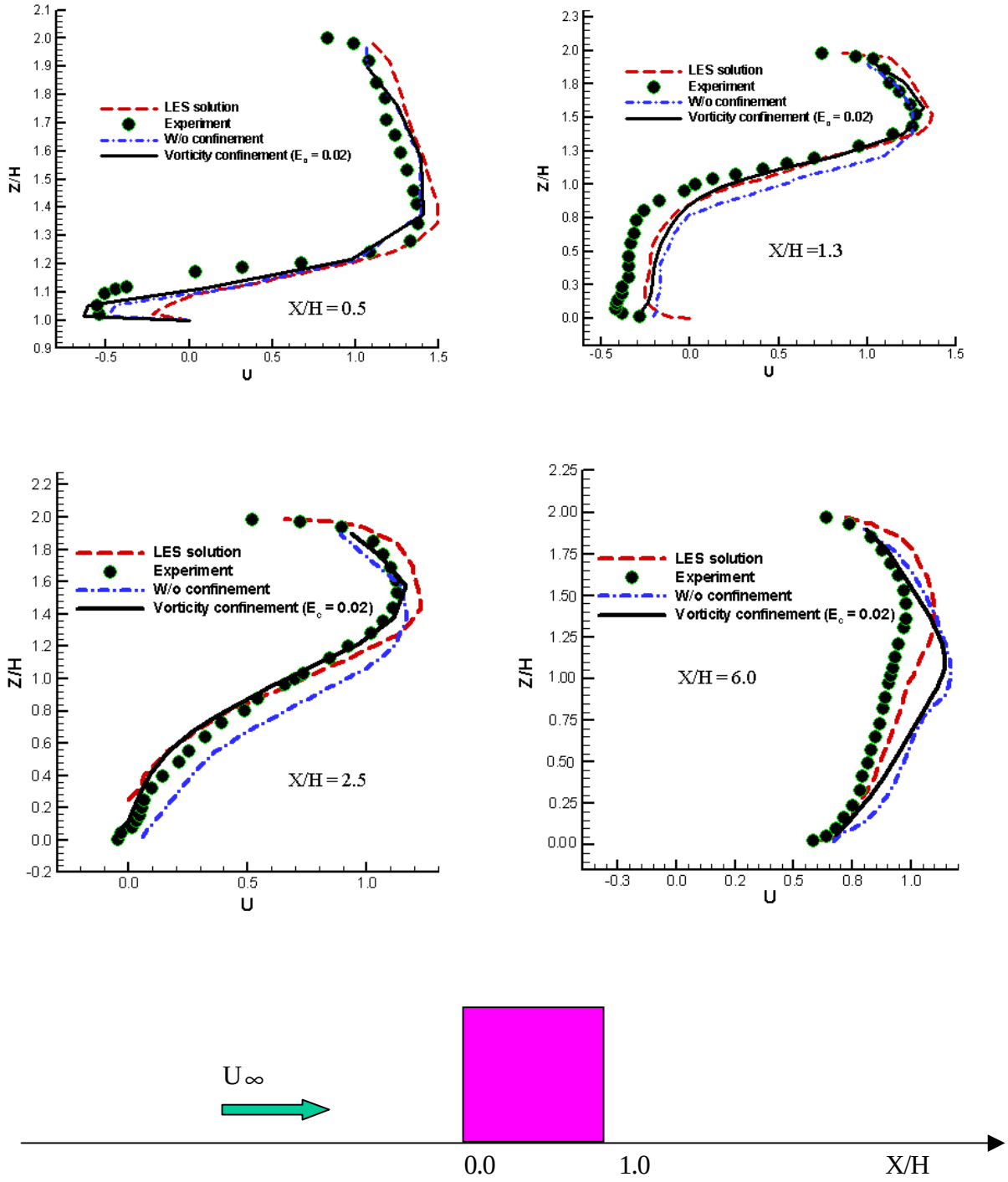


Figure 5.9: The comparison among CVC, LES [58] and the experiments [4,5] for the mean velocity component U at several locations on the symmetry plane.

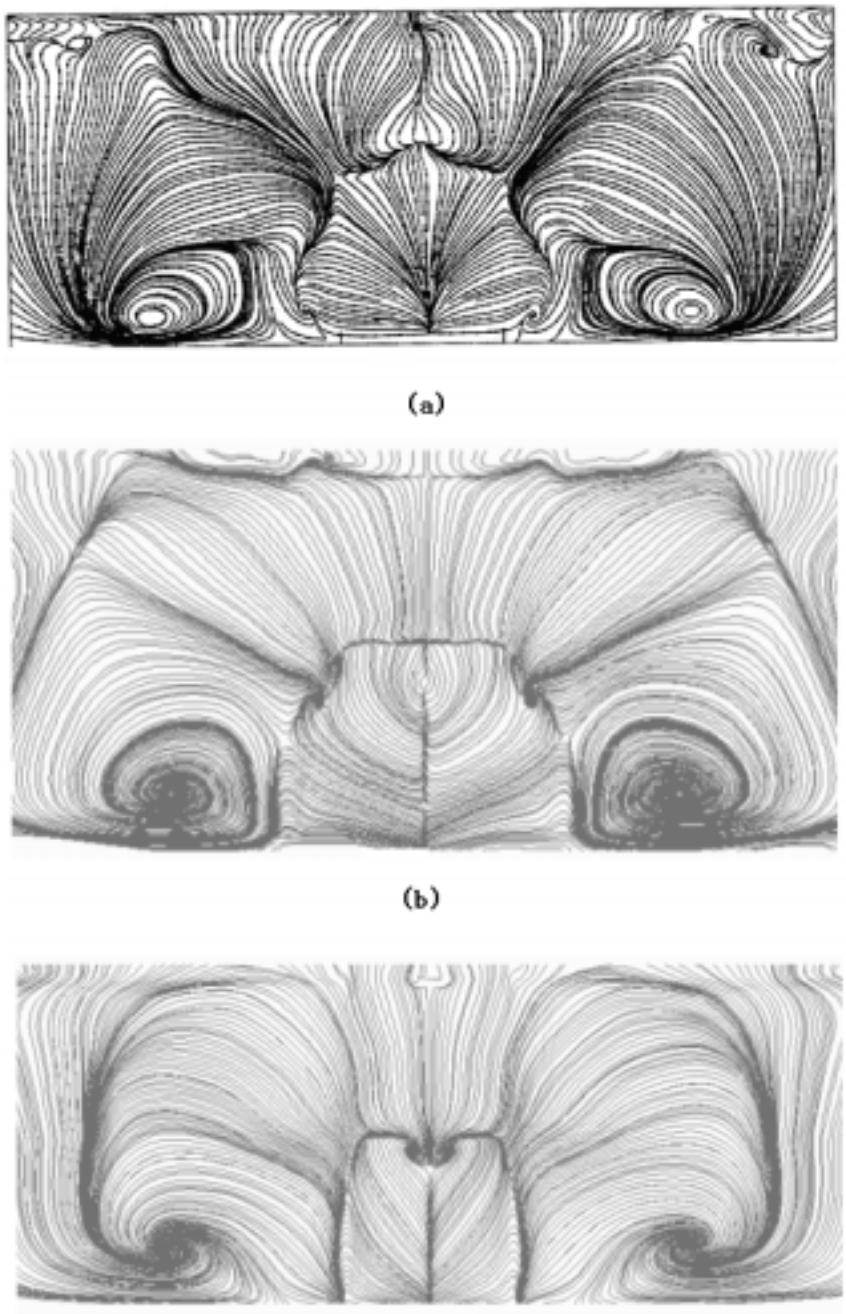


Figure 5.10: The comparison between CVC and LES calculation [57] for the streamline distributions on the plane parallel to the back face at 0.1 step size of the cube dimension.
Legend: (a) LES [57], (b) CVC with grid 51x35x40, (c) CVC with grid 32x24x24.

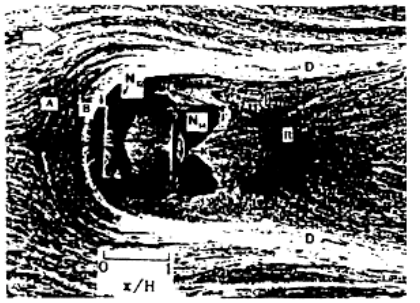


(a)

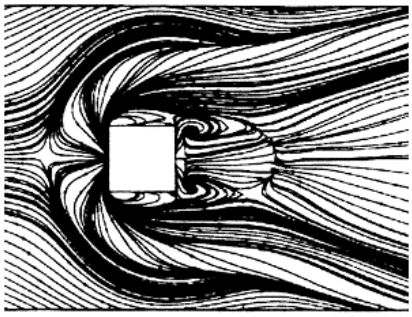

(b)

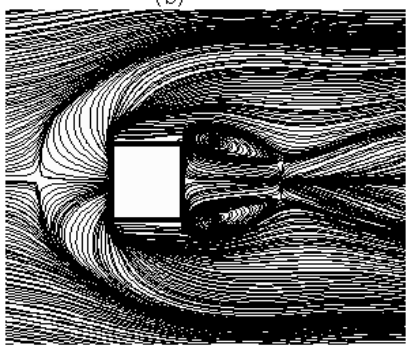

(c)

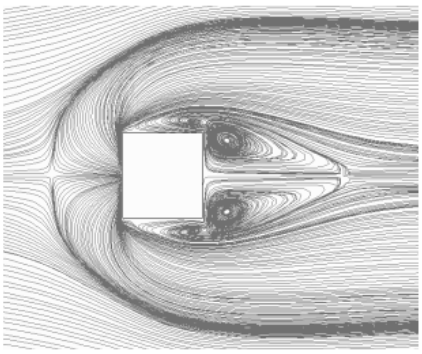

(d)

Figure 5.11: The comparison among experiment [4,5], LES-D [13], and CVC for the streamline distributions on the floor of the channel.

Legend: (a) experiment [4,5], (b) LES-D [13], (c) CVC with grid 51x35x40, (d) CVC with grid 32x24x24.

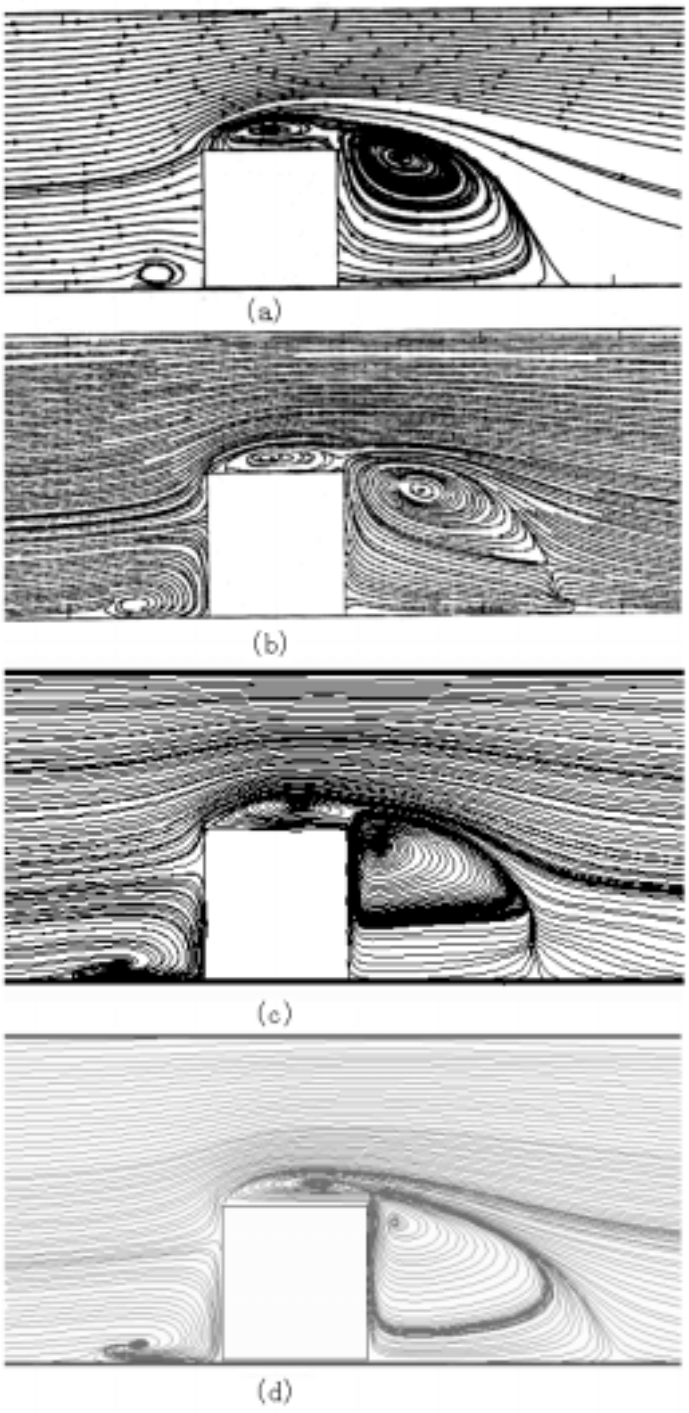


Figure 5.12: The comparison among experiment [4,5], LES [57], and CVC for the streamline distributions on the symmetry plane.

Legend: (a) experiment [4,5], (b) LES [57], (c) CVC with grid 51x35x40, (d) CVC with grid 32x24x24.

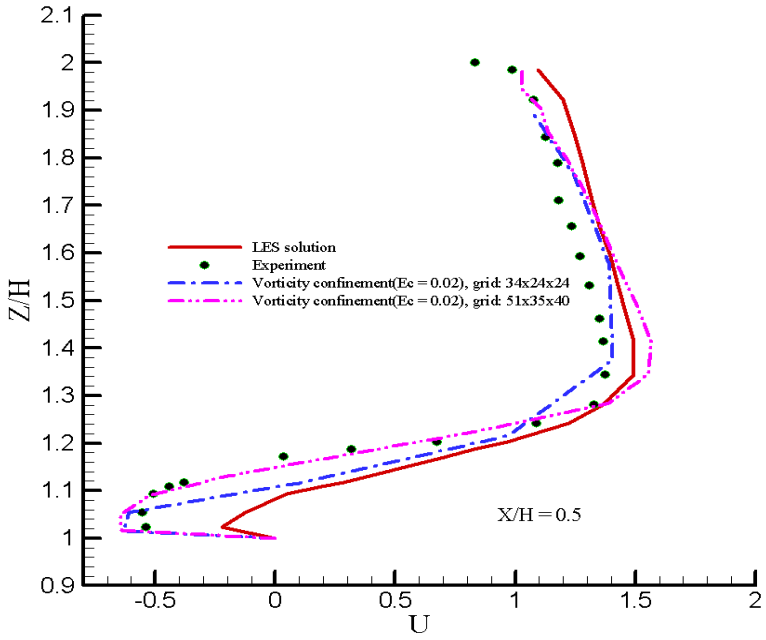


(a)

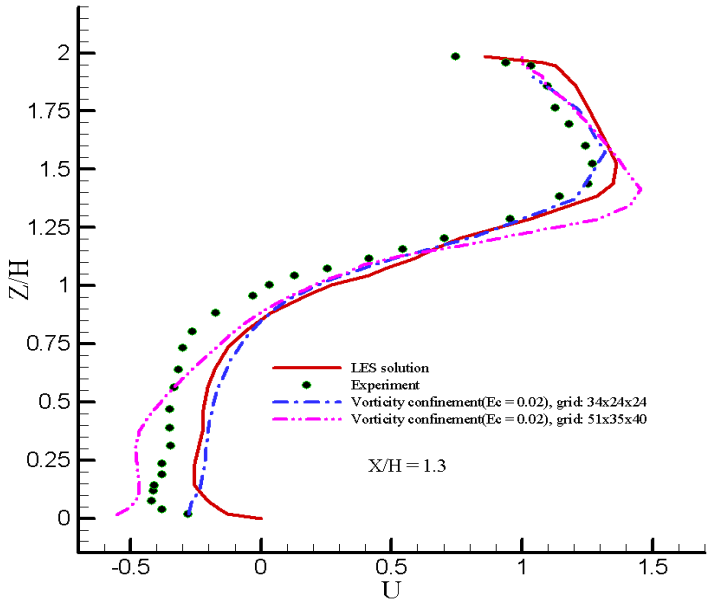


(b)

Figure 5. 13: The velocity profiles on the symmetry plane. Experiment --- Refs.[4,5]; LES --- Ref.[58].

## 5.4 Conclusions

The numerical simulation for the turbulent flows past a 2D square cylinder and a 3D surface- mounted cube are among the most difficult problems in current CFD, since the flow patterns are very complex and featured by bimodal, multiple separations with steep streamline curvature, arch and corner vortices behind the cube, and for two-dimensional case, periodical vortex shedding.

The comparisons of results from CVC, LES and RANS calculations for the flow around a 2D square cylinder presented above showed that CVC calculation gives an entirely satisfactory qualitative picture of the flow field. The standard $k-\varepsilon$ model produced very poor results due to its under predicting the unsteady large-scale vortical motions that may be explained by its excessive "turbulence production" (modeled dissipation) in the front stagnation region. The TL and KL modification produced improved results. The excessive "turbulence production" is removed by using RSM, but this will give over prediction of the unsteady vortical motions.

The LES calculations gave better results than did the RANS calculations for the flow around a 2D square cylinder, but the price to be paid for these results was very high. According to Ref. [13], The LES-UKAHY2 calculation took 73 hours on a SNI S600/20 vector computer, but RANS calculation with the wall function took 2 hours and TL approach took 8 hours on the same computer, while CVC calculation took about 4 hours on PC with a 733 MHz Pentium III Processor.

For the flow over the 3D cube on the floor of a channel, the flow field calculated with CVC was in generally good qualitative agreement with the experimental results and LES calculations. However, the detail of the converging-diverging behavior of the horseshoe vortex near the floor and behind the cube was not predicted on the coarse grid. Grid refinement did capture this detail with CVC.

In general, CVC produced much better agreement with experimental data than RANS calculations, which completely failed to predict the correct separation length behind the body. The quantitative agreement for axial velocity profiles for the CVC calculations was excellent and compared very favorably with the best of the LES calculations.

For the calculation of the flow past a cube, LES-UKAHY2 took 160 hours on SNI S600/20 vector computer while RANS with TL model took 6 hours and the standard $k-\varepsilon$ model with the wall function only took only 15 minutes on the same computer [13], but CVC with 32x24x24 grid points just took about 40 minutes on PC with a 733 MHz Pentium III processor. In addition, LES calculations must use very fine grids (about one million) to obtain reasonable solution for 3D calculations. However, in the present study, by using CVC we obtained a reasonable solution with just about 2% grid points of the LES calculations; as a result, much less computer resource was used. With the overall performance and the computer resource required, CVC looks to be very promising for solving the realistic engineering problems such as the flows around tall buildings, bridges and automobiles, etc. However, further study and testing are necessary to evaluate solution accuracy and reliability.

From the calculations we observed that the value of the confinement parameter played important roles in deciding the vortex shedding frequency and the drag coefficient for the flow past a 2D square cylinder. Furthermore, the vortex shedding frequency without confinement was predicted smaller by 6 % - 13 % of the measured range of the experiments and no vortex shedding occurred when a very large value of the confinement parameter is employed, ($E_c = 0.5$ was tested in the present study). In addition, the drag coefficient increases as the value of the confinement parameter increases. The drag coefficient without confinement was predicted smaller by 5 % - 17 % of the measured range of the experiments. On the other hand, if $E_c = 0.001 - 0.01$ is chosen, the drag coefficient will fall in the measured range of the experiments.

Finally, we consider the issue of grid convergence. For the calculation of the flow past the 2D square cylinder, we used two sets of grids. One was 50x50; the other was 100x90. We believe that we obtained the grid convergent solution with the finer grid. However, for the calculation of the flow over the 3D cube mounted on the floor of a channel, we have not been able to test finer grids because very large computer resources are needed, and we may not have obtained the grid convergent solution for this case.

# Chapter 6

# Parallel Computation for the Flow past a 3D Surface-Mounted Cube Using Domain-Decomposition Algorithms

## 6.1 Introduction

Turbulent flows around three-dimensional (3D) obstacles are common in nature and occur in many applications including flow around tall buildings, vehicles and cooling flows around computer chips. The sketched flow pattern for the flow past a cube mounted on the floor of a plate channel is presented in Figure 1.3f. Understanding and predicting the properties of the flows are necessary for effective, economical and good engineering designs. Experimental techniques are expensive and often provide data that is not sufficiently detailed. With the advent of supercomputers it has become possible to investigate these kinds of flows using numerical simulations.

As we discussed in Chapter 1, a number of approaches to computer prediction of flows past 3D obstacles have been proposed and used. One of the approaches is solving Reynolds-Averaged-Navier-Stokes (RANS) [13,15] equations with a variety of turbulence models. Another approach is Large Eddy Simulation (LES) [13,57,58], in which the large scales of motion are computed explicitly, while the small or sub-grid scale motions are modeled. In the present computation, we used Euler equations with Compressible Vorticity Confinement (CVC) approach. The complicated turbulence models of RANS

and huge computation of LES are both avoided in this approach, and from discussion in Chapter 5, we see that it should suffice to capture the large turbulent structures present in the flows.

## 6.2 Computer Requirements

If the LES approach is used to simulate the turbulent flows past a 3D surface-mounted cube in a plate channel, it is estimated that the grid points will have to be about one million in order to obtain "engineering-accuracy" prediction of the surface pressure and the overall wind force over the cube. Furthermore, about 100,000 iterations will be required in order to resolve the unsteady motion of the turbulent flow structures. Supposing 10,000 operations per point per iteration, then about $10^{15}$ operations will be required per problem. In 1990, H. Werner and H. Wengle used LES to simulate the turbulent flow over and around a cube mounted on the bottom of a plate channel using 144x96x56 (766,364) grid points [58]. In 1996, K. B. Shah and J. H. Ferziger performed the LES for a 3D surface-mounted cube with 196x64x94 (1,179,646, more than one million) grid points [57]. If a sequential code was used to run this kind of problem, both run time and memory storage could be problematic. So in this chapter an effective fast parallel computation will be developed using domain-decomposition algorithms.

## 6.3 Parallel Algorithms

From the long-term viewpoint, parallel computing is the solution for intensive computer simulations in CFD research and its engineering applications. Parallel computing offers the promise to provide the massive computational resources that CFD requires. However, the practical achievement also relies on the parallel algorithms and numerical methods that play important roles in the computation. Domain decomposition is the most natural and popularly used approach for parallel computing in CFD. In fact, decomposition of physical or computational domains has been used in CFD for years because of the benefits of allowing physically zonal modeling and saving storage in implicit procedures. For most explicit solution methods, implementation of domain decomposition is straightforward. Some effort must be made, however, to minimize synchronization and communication overhead. On the other hand, load balancing is another very important factor that must be considered for achieving high performance

parallel computing in CFD. The effects on performance of the synchronization and load balance will be reported in the last part of this chapter.

### 6.3.1 Domain Decomposition Algorithm Using One-To-One Scheme [59]

The computational domain is divided into a number of equal size sub-domains in the stream direction (the same as the number of processors in use), and the computation within each of the sub-domains is mapped onto one of the processors available, hence the name of the algorithm. Here "equal-size" means that the number of mesh points of each sub-domain is about equal to each other. Within each sub-domain, updating of the flow variables $\rho, u, v, w$ and $p$ is done sequentially, where $\rho$ is the density in the flow field, $(u, v, w)$ is the velocity component in x, y and z direction, respectively, in Cartesian coordinates. The values of the flow variables at boundary points of each sub-domain are transferred from the closest two neighbors. Only two communications are required per sub-domain per iteration. There also have been two other domain-decomposition algorithms available for CFD. One has six way communications if the computational domain is divided into sub-domains in x, y, and z directions simultaneously [60]. The other has four way communications if the computational domain is divided into sub-domains in x and y directions simultaneously [60]. The algorithm used in the present research has the minimum communication cost among these three methods. Furthermore, the load balance can be achieved more easily with the domain being divided into sub-domains just in one direction.

In conclusion the domain decomposition algorithm using the one-to-one scheme is given below:

Step 1: Decompose the computational domain into number of processors N in the stream direction.
Step 2: Map each sub-domain onto one of the processor available.
Step 3: Do n = 1, N_iteration in parallel.
Step 3_1: Let all the processor do each iteration n within each sub-domain.
Step 3_2: Let all the processor $P_1$, $P_2$, … $P_N$ do synchronization at the end of each iteration.
Step 3_3: Let all the processors do communication between the two closest neighboring processors.
End do.

### 6.3.2 Domain Decomposition Using Pipeline Scheme [59]

The manner used for domain decomposition for a pipeline scheme is the same as the one-to-one scheme, but the communication and implementation is completely different. First, let one of the processors compute an iteration over the entire domain one sub-domain by one sub-domain so that when it finishes one sub-domain or begins to compute a new sub-domain, let another processor start working on it at the new iteration, and so on so forth. If the domain is decomposed into N sub-domains, and N number processors can be available, let N processors collaborate to compute the entire domain, after the N-th processor finishes the last sub-domain, the first processor should begin to calculate the (N+1)-th iteration. Obviously, the processor needs the data of the previous iteration, so the communication is needed between the processors that perform the current iteration and the previous iteration. In order to communicate in the consistent way with the pipeline scheme, the processor should transfer the data for each sub-domain into the processor that will perform the same sub-domain at the next iteration. In this fashion the data gets communicated in something like the manner with which 4 people collaborate to do a relay race game. When one person finishes a quarter of a circle, he or she transfers the baton to another person who is waiting there and after he or she gets the baton, he or she continues to run the second quarter of the circle, so on and so forth until they finish the race.

In conclusion, the domain decomposition algorithm using the pipeline scheme can be given as follows:

Do n = 1, N_iteration, N_processor.

Step 1: Let processor 1 start to compute the entire domain from sub-domain 1 to sub-domain N at time step n.

Step 2: If (processor 1 finishes the calculation of the first sub-domain) Let processor 2 start to compute the entire domain at time step n+1.

Step N: … so on so forth until to processor N.

End Do.

### 6.3.3 Synchronization

One of the very important issues for parallel CFD is the synchronization. For unsteady problems, synchronization must be enforced at the end of each iteration or at the beginning of each iteration to

guarantee accuracy, because the data at the boundary points and the data between n and n+1 time steps are dependent upon each other. But this must be paid off for run time overhead. On the other hand, for steady problem, synchronization is not performed at every iteration, but may be performed at every 10 or 20 iterations. That will save the time for synchronization. In the present research, we ignored the synchronization in pipeline scheme to study the effect of synchronization on the performance of the parallel computation.

### 6.3.4 Load Balancing

Load balancing is related to the size of the sub-domain in domain decomposition using the one-to-one scheme, because the processor that corresponds with the sub-domain within the cube will be in idle status. This problem may be solved by letting the size of the sub-domain that corresponds to this part of the flow field increase so that the work to be done in the sub-domain inside the cube is about equal to that in the sub-domain outside the cube. However, in order to study how load unbalancing impacts on the performance of the parallel computation, we decompose the domain into sub-domain with about equal length in the stream direction. When the number of sub-domain increases, the size of each sub-domain will decrease, and load unbalancing will increase. The effects on performance of load unbalancing will be reported in the last part of this chapter.

## 6.4 Implementation Issues

The whole implementation was completed using Fortran 90 and Message Passing Interface (MPI) [61] on a Beowulf computer. The implementation includes the numerical methods along with the communication and synchronization approaches. In this section, we will discuss how to implement the communication between processors and processes and how to synchronize all the processors and processes. The original sequential code was written in Fortran 90. Fortran 90 is a good language for parallel scientific computation. There are many built-in procedures that can help to achieve high performance. In the present research the original Fortran 90 code was modified into parallel code using MPI.

The communications between the two closest processors / processes are implemented using MPI. The MPI_SENDRECV is used to implement the data shift in the two neighboring processors for one-to-one scheme to prevent the dead lock that may be caused in the communications. MPI_SEND and MPI_RECV both were used in the two closest processes (the process at time step n and the process at time step n+1) in the pipeline scheme. For one-to-one scheme, MPI_GATHER is called to gather the data from each processor to calculate the residual of the whole domain and stores the data for visualization of the whole computation domain, and MPI_BCAST is used to broadcast the data from the root processor (with zero process id) to each of the other processors for initializing the flow variables. The pipeline scheme calculates the residual in each processor, so that no data gather will be performed. Furthermore, the data initialization for flow variables is needed just for the processor that begins the calculation in the first iteration. So no MPI_GATHER and MPI_BCAST are needed to do the data initialization for pipeline scheme. Just one MPI_BARIER is called to implement the synchronization of all the processes at end of each iteration for the one-to-one scheme.

## 6.5 Numerical Experiment Results and Analyses

In this section, we present all the numerical experiment results of the parallel computation using the methods described above.

The Speed Up and Efficiency are defined as Speed Up = $T_1/T_p$ and Efficiency = Speed Up / p. Here, $T_1$ is the CPU time for one node to finish the whole computation (using the same code and memory space). $T_p$ is the CPU time for p nodes to collaborate to complete the parallel calculation.

The parallel computation was performed with 100 time steps and 32x24x24 Cartesian grid points. This set up is just for purpose of testing the program. In an actual computation, many more iterations and many more grid cells may be required.

The Speed Up curve is presented in Figure 6.1, the Efficiency curve is presented in Figure 6.2, and the performance curve in term of CPU time is shown in Figure 6.3.With the curves presented here we can discuss that how the type of scheme, synchronization, the size of sub-domain and load unbalancing impact on the performance of the parallel computation.

### 6.5.1 Speed Up and Efficiency vs. Scheme and Synchronization

With the Speed Up curve presented in Figure 6.1, we can see that the slope of the Speed Up of one-to-one scheme with synchronization is much lower than the pipeline scheme without synchronization. At the same time the efficiency curve presented in Figure 6.2 shows the efficiency of pipeline is much higher than that of the one-to-one scheme. Both the type of the scheme and synchronization played a very important role in this parallel computation. Synchronization is especially important; it shows more importance because the work done in one-to-one scheme and pipeline scheme are not substantially different. The data transferred in pipeline scheme from one processor that performs the calculation at time step n to the processor which performs the calculation at time step n+1 is much more than the data transferred in one-to-one scheme between the closest two neighboring processors. Because in the pipeline scheme the data transferred are the whole data in each of the sub-domain while the data transferred in the one-to-one scheme are just the data at the boundary points. So the communication time in the pipeline scheme should be longer than that taken in one-to-one scheme. Hence the synchronization overhead in one-to-one scheme dominates the total overhead in the computation. This observation is the same as that reported in other parallel CFD computations [59].

### 6.5.2 Efficiency vs. Load Balancing

The efficiency curve presented in Figure 6.2 shows that the efficiency for the one-to-one scheme decreases very sharply as the number of processors increases. One of the reasons could be synchronization. Another very important reason is the load unbalancing. As the number of processors increases, the number of sub-domain also increases. The domain is divided into equal-size sub-domains with the same number of processors, so the size of the sub-domain will decrease as the number of sub-domains increases. The grid used is a Cartesian grid, the sub-domain inside of the cube is still counted as sub-domain, but the work done there is much smaller than the work done in the sub-domain outside the cube. So the processor that performs the calculation of the sub-domain inside the cube idled most of the

time; therefore, the load is unbalanced. When the number of processors increases, the load unbalancing gets much worse. One of the procedures that can fix this problem is to increase the size of the sub-domain inside the cube letting the work to be about the same as that done in the sub-domain outside the cube. But here we have divided the domain into equal size sub-domain in order to study the effect on the performance of the parallel computation by the load unbalancing. Therefore, in addition to synchronization, load balancing is another very important factor for obtaining high parallel performance.

### 6.5.3 Performance in Term of CPU Time

The CPU time curve presented in Figure 6.3 shows smaller difference between the one-to-one scheme with synchronization and pipeline scheme without synchronization compared with efficiency difference between the two schemes. The load unbalancing inside the cube left some of the processors idle. However, the time for the processor to perform its computation in the sub-domain outside the cube should be the same if the number of processors used is the same for two schemes. The only difference comes from the differences of the overhead due to synchronization and communication. So the results obtained are reasonable. The same conclusion was obtained by other parallel computation [59].

## 6.6 Conclusion

The performance of parallel computation strongly depends on the specific algorithms and the actual implementation. The type of the scheme, the size of the sub-domain, synchronization and load balancing all play very important roles and are correlated in achieving high parallel computing performance. For the types of problems that we were solving the pipeline scheme without synchronization achieved the best performance in a simple domain and a structured grid.

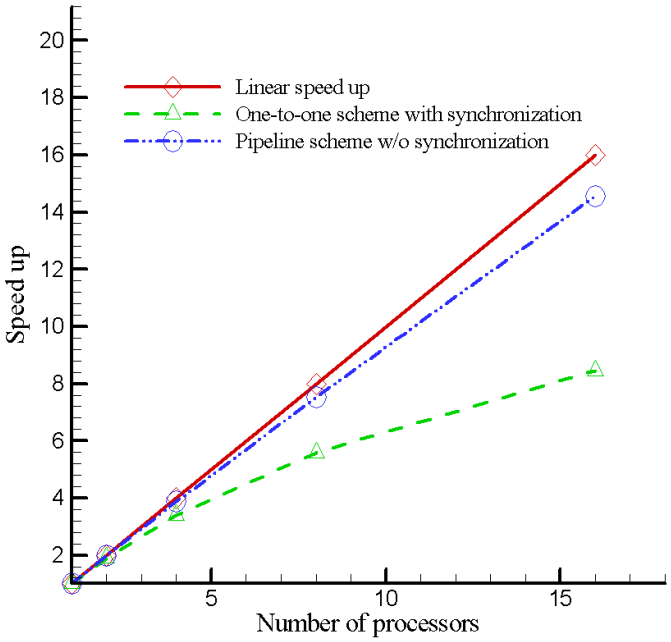


Figure 6.1: Speed Up vs. type of scheme and synchronization.

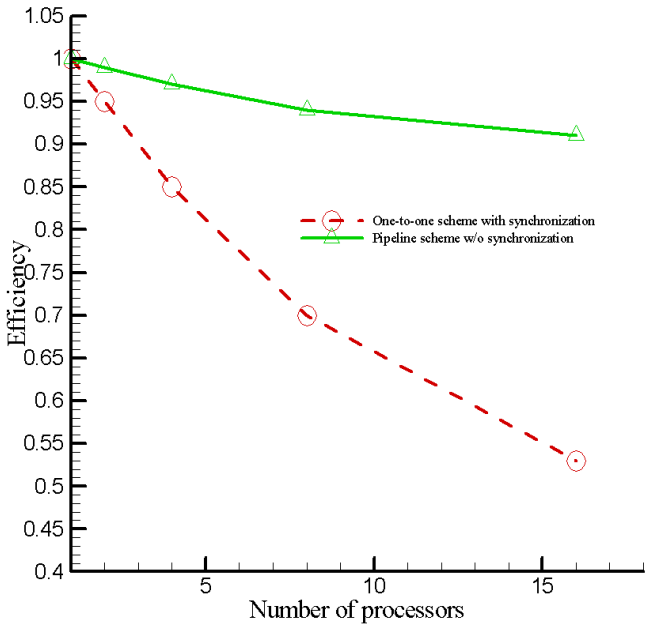


Figure 6.2: Efficiency vs. load balancing.

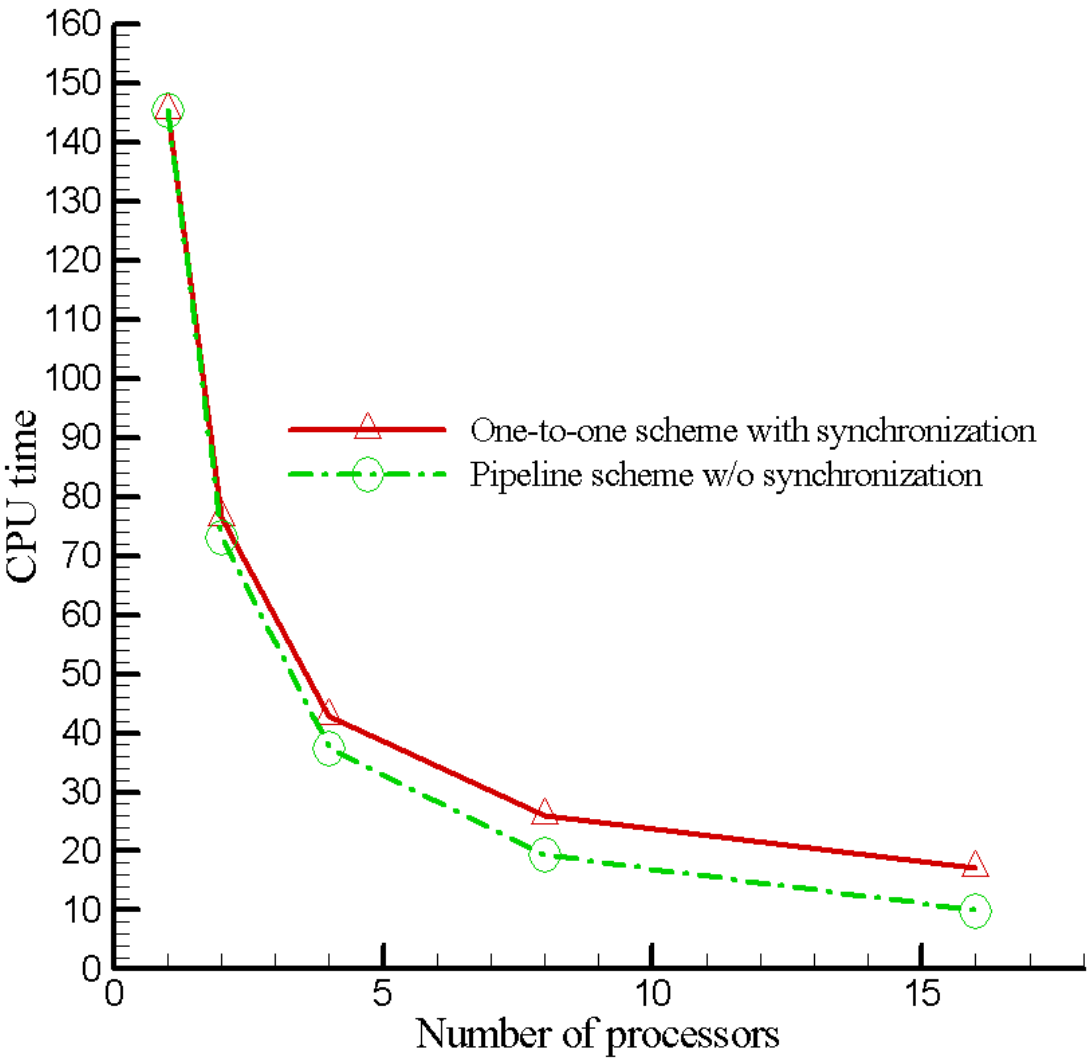


Figure 6.3: Performance in term of CPU time.

# Chapter 7

# Fundamental Properties of Compressible Vorticity Confinement (CVC)

Some applications of Compressible Vorticity Confinement (CVC) to complex vortex-dominant flows were presented in Chapters 3 through 6. However, a number of fundamental questions have arisen: Why does CVC work so well for turbulent flows? What is the numerical accuracy for CVC? What are the limitations for using CVC? In this chapter, we will try to give some preliminary answers for these kinds of questions and attempt to give some insight to the fundamental properties of CVC.

## 7.1 Turbulent Boundary Layer Over a Flat Plate

Almost all engineering problems in fluid dynamic applications are turbulent. The flow past a square cylinder and the flow over a surface-mounted cube on the floor of a plate channel are complicated turbulent flows with massive separation. The results presented in Chapter 5 are generally in good agreement with experiments and state-of-art computations with RANS and LES methods despite the fact that only an Euler solution with the grid spacing appropriate for an inviscid flow was used with a no-slip boundary conditions enforced on solid walls. One large difference between CVC and LES calculations is the number of grid points. The grid points (32x24x24) we used for the flow over a cube were about 1 / 60 the number of grid points (172x64x76) used by Shah and Ferziger [57] and about 1 / 40 the number of grid points (144x72x58) used by Werner and Wengle [58]. An important question is now why did CVC obtain good agreement with the experiments and LES using such a coarse grid?

The turbulent flow over a flat plate is much simpler than the turbulent flow past a 3D cube in a channel or the flow over a 2D square cylinder. The results of this simple case may help to understand the

complicated situations. In order to gain insight into the behavior of the method, we considered the flow over a 2D flat plate.

The calculations are performed using our basic inviscid flow solver, with the confinement term added along with a no-slip boundary condition, using a grid adequate to model the inviscid phenomena. Note that we are not advocating this approach to produce accurate boundary layer results. We are performing this calculation to try to understand the results presented for the vortex dominated flows in the preceding chapters. The basic solver MDM [(2)] and scalar vorticity confinement with dissipation parameter $E_d = 0.3$ were employed in this calculation. We chose this value because in most of our applications we used this value or a value that was close to it. On the other hand, we will use different values of the confinement parameter to test the effects of the value of the confinement parameter on the velocity profile of the flow over a 2D flat plate. Furthermore, different grid sizes in the normal direction of the flat plate and along the plate were used to test the effect of the grid size on the velocity profile.

The flat plate is 1 ft long ($L$ = 1ft), and the free stream is the air at sea level with Mach number 0.1, at which the Reynolds number approximates 200,000. Uniform free stream conditions are imposed at a distance *L/4* upstream of the plate, and *L/2* above the flat plate. No-slip conditions are applied on the plate and the flow variables are extrapolated downstream at the exit of the computational domain in stream wise direction.

The coordinates consist x and y; x is the coordinate in stream direction with the origin at the inlet and *y* is the coordinate in the normal direction with the origin at the flat plate. In order to present our results, there are two scales which may be used to scale the vertical coordinate y. One is the thickness of a laminar boundary layer over a flat plate, which is written as follows:

$$\delta_L \approx 5.0\sqrt{\frac{\nu x}{U_e}}\ , \tag{7.1}$$

the other is the thickness of a turbulent boundary layer over a flat plate, which may be approximated as follows:

$$\delta_T \approx x \frac{0.375}{(U_e x/\nu)^{1/5}}\ , \tag{7.2}$$

where $U_e$ is the velocity at the outer edge of the boundary layer, $\nu$ is the kinematic viscosity in the flow. We use Blasius solution as the "exact" solution of the laminar boundary layer, and use 1/8 power law profile as the turbulent boundary layer solution. The 1/8 power law is written as follows:

$$\frac{u}{U_e} = (\frac{y}{\delta_T})^{\frac{1}{8}}. \tag{7.3}$$

First, we computed the flow on a 100x25 grid and a 200x25 grid without confinement ($E_c = 0$) and with confinement ($E_c = 0.12$) to test the effect of the confinement and the grid spacing effect in the streamline direction on the velocity profile. Figure 7.1 presents $u/U_e$ profiles with and without confinement versus the $y/\delta_T$. Figure 7.2 presents $u/U_e$ profiles without confinement versus $y/\delta_L$. Figure 7.3 presents $u/U_e$ profiles with confinement ($E_c = 0.12$) versus $y/\delta_T$. Figure 7.4 presents the velocity profiles versus $y/\delta_T$ at more locations about the developmental boundary layer. With this figure we have three important findings:

(1) The velocity profile $u/U_e$ with confinement vs. $y/\delta_T$ is fuller than the turbulent velocity profile but resembles a turbulent boundary layer in the near wall region;

(2) The velocity profile $u/U_e$ vs. $y/\delta_L$ more closely approximates a laminar velocity profile than a turbulent profile when confinement is turned off;

(3) The solutions at different axial locations are more "similar" to each other when confinement is applied in the calculation. Solutions without confinement do not appear to have any measure of this similarity property.

Next, we consider the effect of grid spacing in the normal direction by considering mesh sizes of 100x10, 100x25, 100x50 and 100x100, all with vorticity confinement, $E_c = 0.06$. In Figure 7.5 we see that the velocity profile evaluated at x = 2L/3 becomes slightly fuller as the mesh is refined. However, all the profiles have very similar behavior near the wall, even the coarsest grid. The coarsest grid case somewhat mimics the three-dimensional separated flow cases discussed in section 5.3, which had one or two grid points in the turbulent boundary layer, but obtained an overall good approximation to the experimental data.

Finally, we show the effect of confinement parameter on the velocity profile. Figure 7.6 presents the velocity profiles $u/U_e$ at x = L/3 and a100x25 grid with a series of the confinement parameters $E_c = 0.96,0.48,0.24,0.12,0.06,0.04,0.02,0.01,0.005$ and no confinement $E_c = 0$. From Figure 7.6 we see that increasing the confinement parameter over this range of values produces increasingly fuller profiles until, for values beyond $E_c = 0.35$, the velocity profile overshoots. For small values of $E_c$, the profile is more "laminar", but as discussed previously, the similarity property is not well represented. However, we see that over a range in values of $0.06 \le E_c \le 0.24$, that at least in the near wall region, the velocity profile is relatively insensitive to the value of confinement parameter. Over this range of values, as shown in Figure 7.7, we believe that the current method provides a rough approximation to a turbulent boundary layer. Then, for flows involving massive separation, the approximate boundary solution may be accurate enough to generate a separation of large-scale structures. It is well known that massive separation from sharp edges is dominated by the behavior of the inviscid rotational flow. Once the structures are generated, the vorticity confinement method does a good job of computing the mainly inviscid rotational flow.

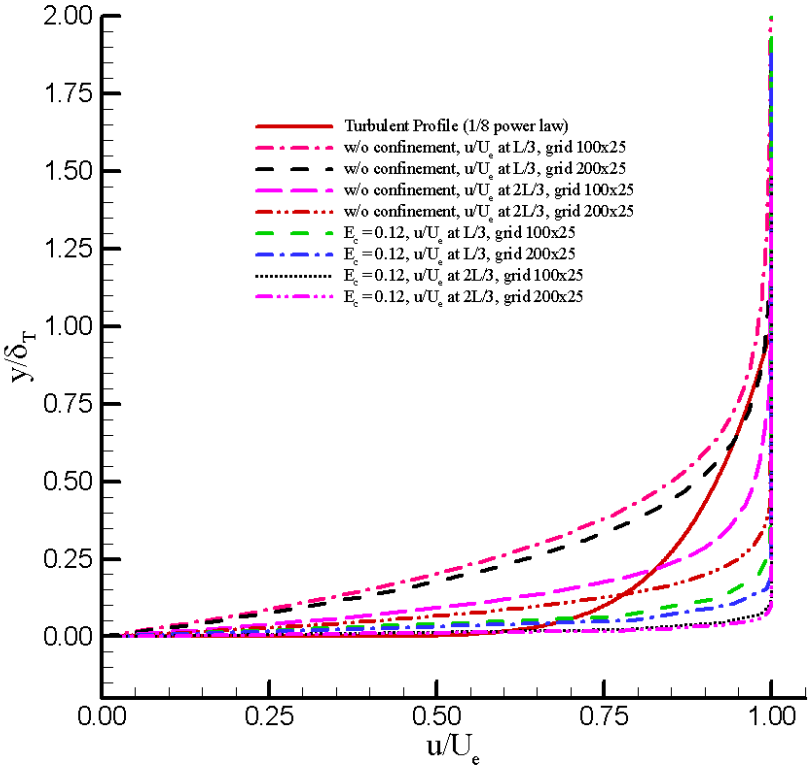


Figure 7.1: Velocity profiles with and without confinement at two locations in the stream direction.

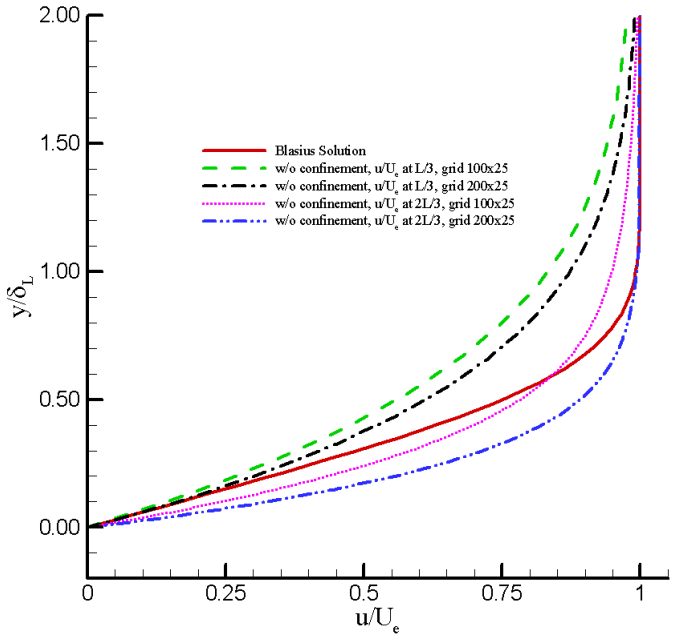


Figure 7.2: Velocity profiles without confinement at two locations in the stream direction.

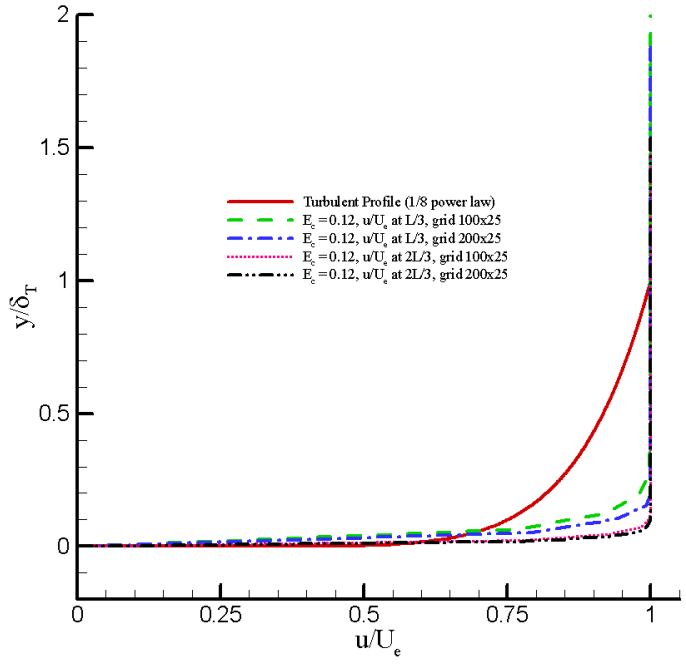


Figure 7.3: Velocity profiles with confinement at two locations in the stream direction.

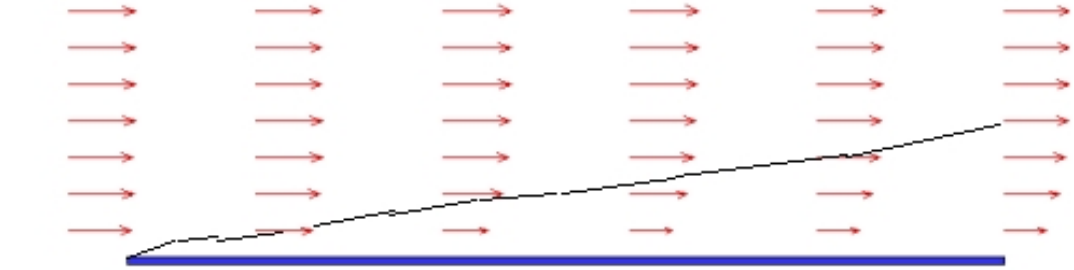

(a)

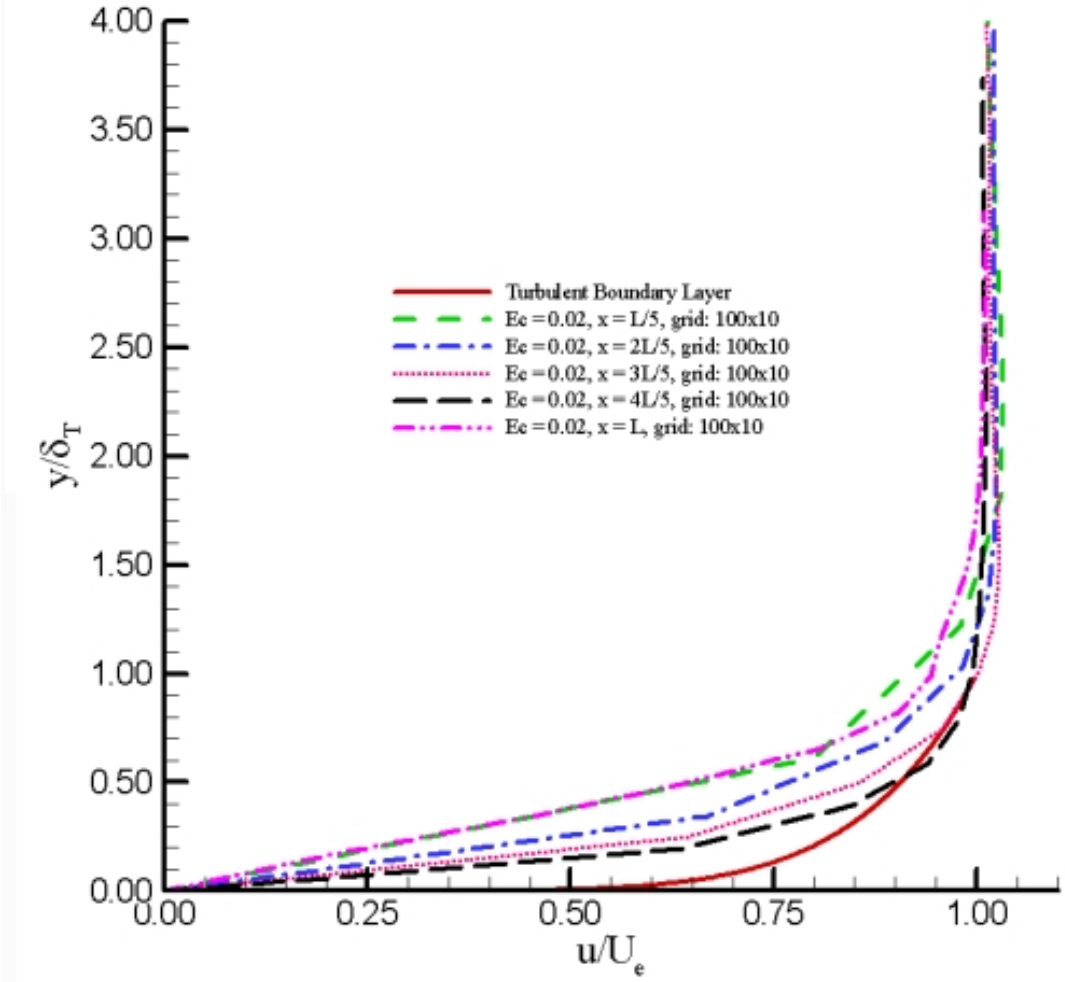


(b)

Figure 7.4: Velocity profiles of the developmental boundary layer. (a) Velocity vector distributions at different locations. (b) Velocity profiles $u/U_e$ at different locations vs. $y/\delta_T$.

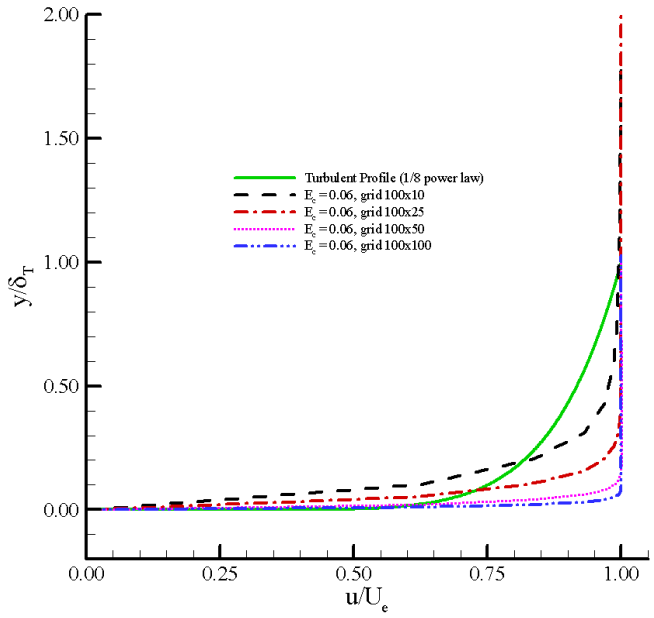


Figure 7.5: Grid spacing effect on the velocity profile.

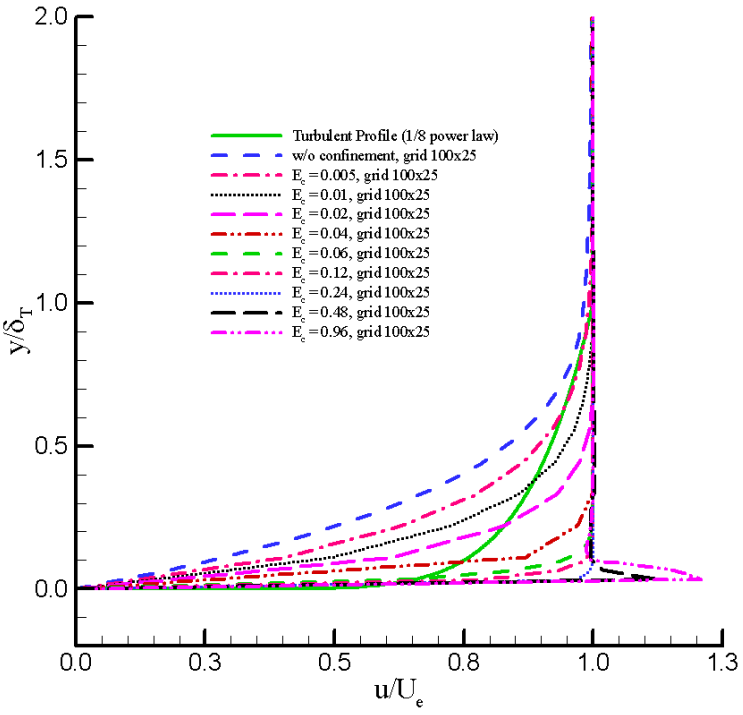


Figure 7.6: Effect of confinement parameter on velocity profiles

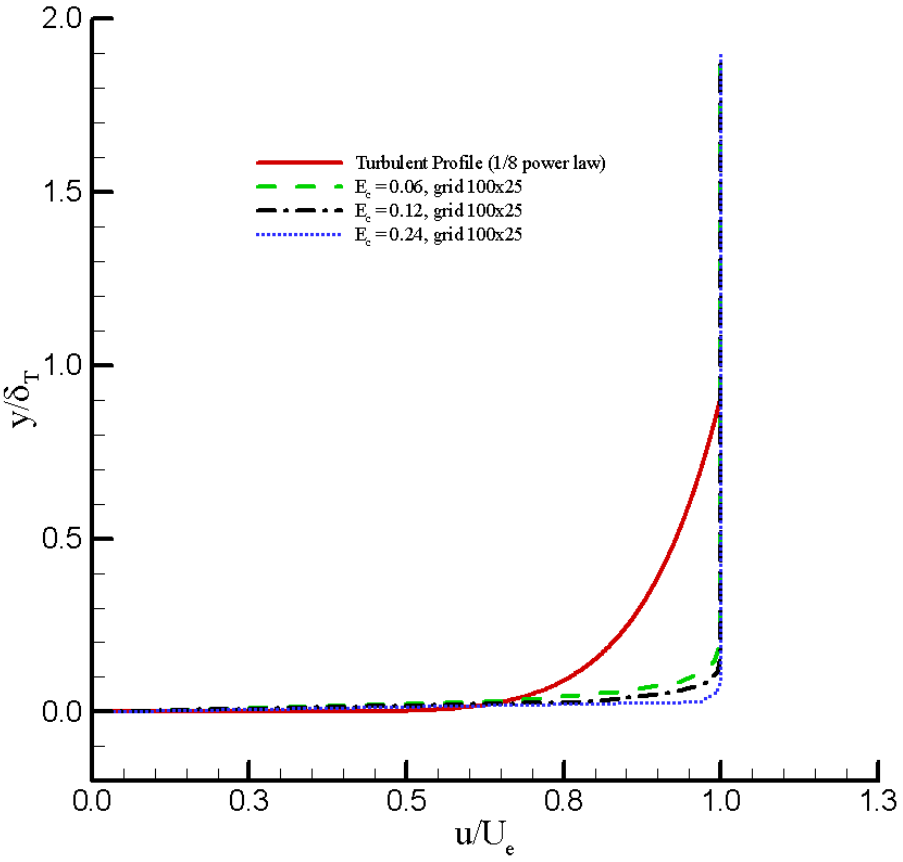


Figure 7.7: Effect of confinement parameter on the velocity profile.

## 7.2 Supersonic Shear Layer

An inviscid supersonic shear layer flow is formed by two parallel streams, one at Mach number M = 2.4 and the other at M = 2.8. In order to show that the solution is independent of the direction of the grid, we let the two streams flow at an angle of 30$^{o}$ relative to the horizontal grid line. The computational grid is a 100x100 uniform Cartesian grid. The basic solver is the MDM [(2)] (discussed in Chapter 2) with dissipation parameter $E_d$ = 0.3. Figure 7.8 and Figure 7.9 show the Mach number contours. Figure 7.8 presents the result of the calculation with the vorticity confinement turned off. The dissipation of the shear layer is obvious. Figure 7.9 shows the same computational result, but with the confinement in effect.

The contours indicate practically no degradation of the shear layer. Figure 7.10 presents the Mach number profile computed using confinement meters $E_c$ = 0.3, 0.1 and no confinement $E_c$ = 0.0 along a cut line that parallels to vertical axis. From the Mach profiles we see that without confinement the solution is significantly degraded, and increasing the confinement parameters will sharpen the discontinuity, but eventually develop an overshoot in the profile.

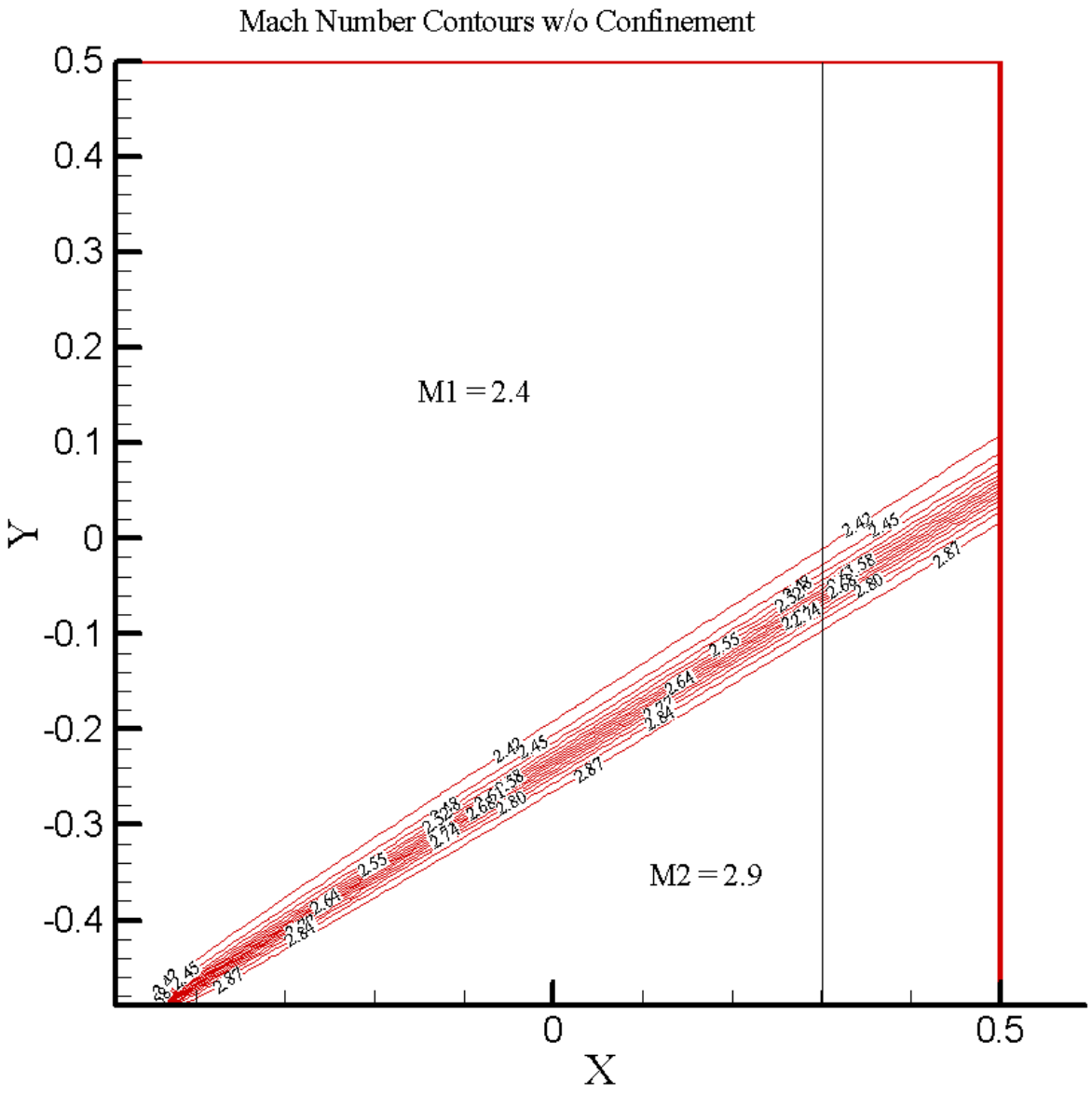


Figure 7.8: The Mach contours of inviscid supersonic shear layer. No confinement.

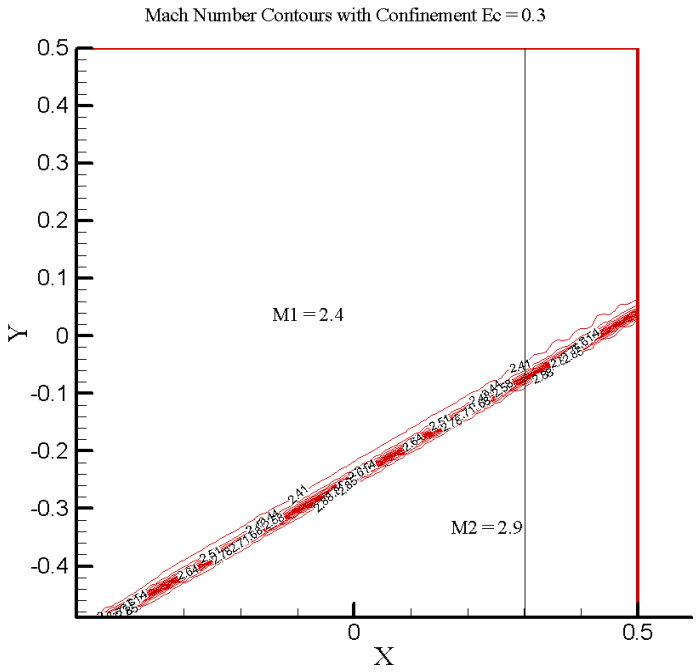


Figure 7.9: The Mach contours of inviscid supersonic shear layer. With confinement.

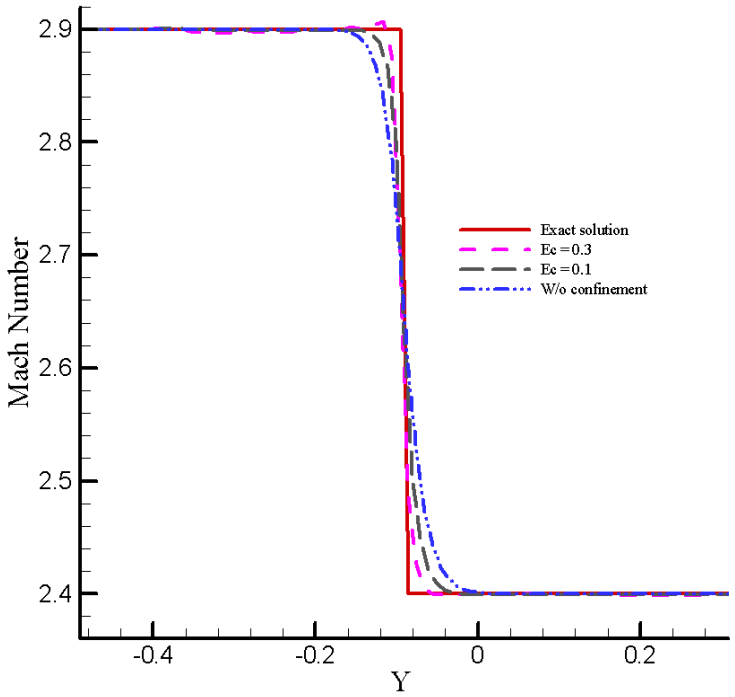


Figure 7.10: The Mach profile along a cut line that parallels to the vertical axis.

The effect of grid size on the classical accuracy of the solution for this problem has been investigated by performing the calculation on three sets of grids, 200x200, 100x100 and 50x50 for $E_c$ varying from 0 to 0.3. Figure 7.11 presents the $L_2$ norm of the error between the computed Mach number distribution and the exact (non-dissipated) Mach number distribution. With the analysis of Figure 7.11 we have two findings:

(1) The error decreases as the grid size decreases when confinement parameter is fixed;

(2) The error decreases as the confinement parameter increases when the grid size is fixed.

Therefore, the effect of decreasing the grid size (increasing the grid points) is similar to increasing confinement parameter when the grid size is fixed. This conclusion may help to explain why we could use the very coarse grids to get good results for 3D and 2D turbulent flows. Furthermore, the conclusion drawn above can be reached by accuracy analysis presented in Figure 7.12, which shows the slope of the log of the norm of the error with respect to the $\log(\Delta x)$. From this figure we see an improvement in the error with increasing value of confinement parameter, with $E_c = 0.3$ achieving close to second-order accuracy.

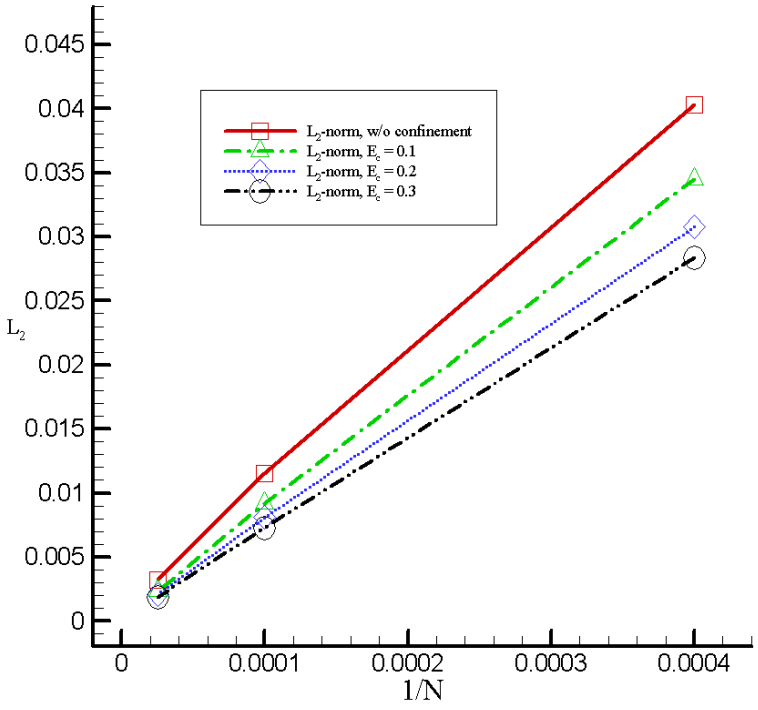


Figure 7.11: $L_2$ error norms vs. grid size for supersonic shear flow calculations. $N$ is the number of grid points.

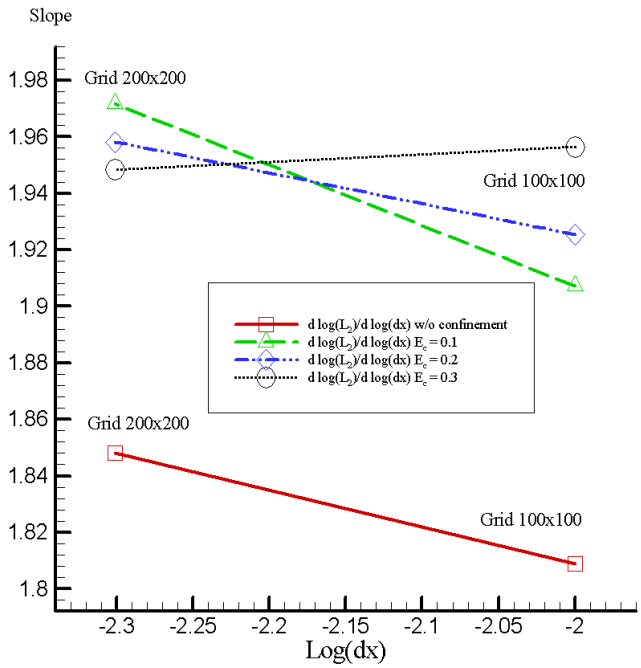


Figure 7.12: Slope of the log of the error $L_2$ norm with respect to log of grid size.

## 7.3 Vortex Moving with a Uniform Free Stream

Next, we consider the flowfield about a vortex moving with a uniform stream. The computational boundary is a square domain 1x1 $m^2$. Periodic boundary conditions are set at all edges of the domain. The computed vortex will then pass through the grid and reappear on the other side. The initial condition of the vortex is set up according to Povitsky and Ofengeim [8]. The tangential velocity distribution is prescribed between an outer radius $r = R_0$ and a core radius $r = R_c$. Outside $R_0$ the tangential velocity of vortex is set to zero. Inside the circle with radius $R_c$ the velocity is linearly proportional to the radius r, hence goes to zero at the center of the vortex, $r = 0$. The tangential velocity of the vortex can be expressed as

$$u_\theta(r) = \begin{cases} U_c r / R_c, r \le R_c \\ Ar + B/r, R_c \le r \le R_0 \end{cases}, \tag{7.4}$$

where

$$\left.\begin{aligned} A &= -\frac{U_c R_c}{R_0^2 - R_c^2}, \\ B &= \frac{U_c R_0^2 R_c}{R_0^2 - R_c^2}. \end{aligned}\right\} \tag{7.5}$$

From Eqs. (7.4)-(7.5), we see that $u_\theta(0) = 0, u_{R_c}(R_c) = U_c$, and $u_\theta(R_0) = 0$. The velocity $u_\theta$ at R $_c$ reaches $U_c$, the maximum velocity magnitude of the whole domain and $U_c$ is a parameter being prescribed before calculation.

The initial vortex is imposed on a uniform free stream and the center of the vortex is located in (0,0) of the Cartesian coordinates. In order to study the non-uniform grid effect on the solution, the grid is stretched and non-uniformly generated. The minimum grid space is 0.0044, which is located at the center of the domain. Then the grid space is stretched according to an exponential function, which is written as follows:

$$\left.\begin{aligned} x_i &= x_1 + m(x_{i_{\max}} - x_1) \\ m &= \frac{e^{\beta_2} - 1.0}{e^{\beta_1} - 1.0} \\ \beta_2 &= k\beta_1 \\ k &= \frac{i-1}{i_{\max} - 1} \\ i &= 1,2,...,i_{\max} \end{aligned}\right\}, \tag{7.6}$$

where $x_1 = 0.0022, x_{i_{\max}} = 0.5, \beta_1 = 1.5, i_{\max} = 50$. The grid is symmetric about the x and y coordinates. A sample grid is presented in Figure 7.13.

We performed the calculation with $R_c$ = 0.05 m, $R_0$ = 10 $R_c$. The speed of sound was $a_\infty = 347 m/s$ and $U_c = U_\infty = 0.5 a_\infty$ on the 100x100 non-uniform grids. The calculation was carried out with MDM [1] and the scalar confinement described in Chapter 2, in which the dissipation and confinement parameters were set to $k^{(2)} = 0.01, k^{(4)} = 0.30, E_c = 0.006$.

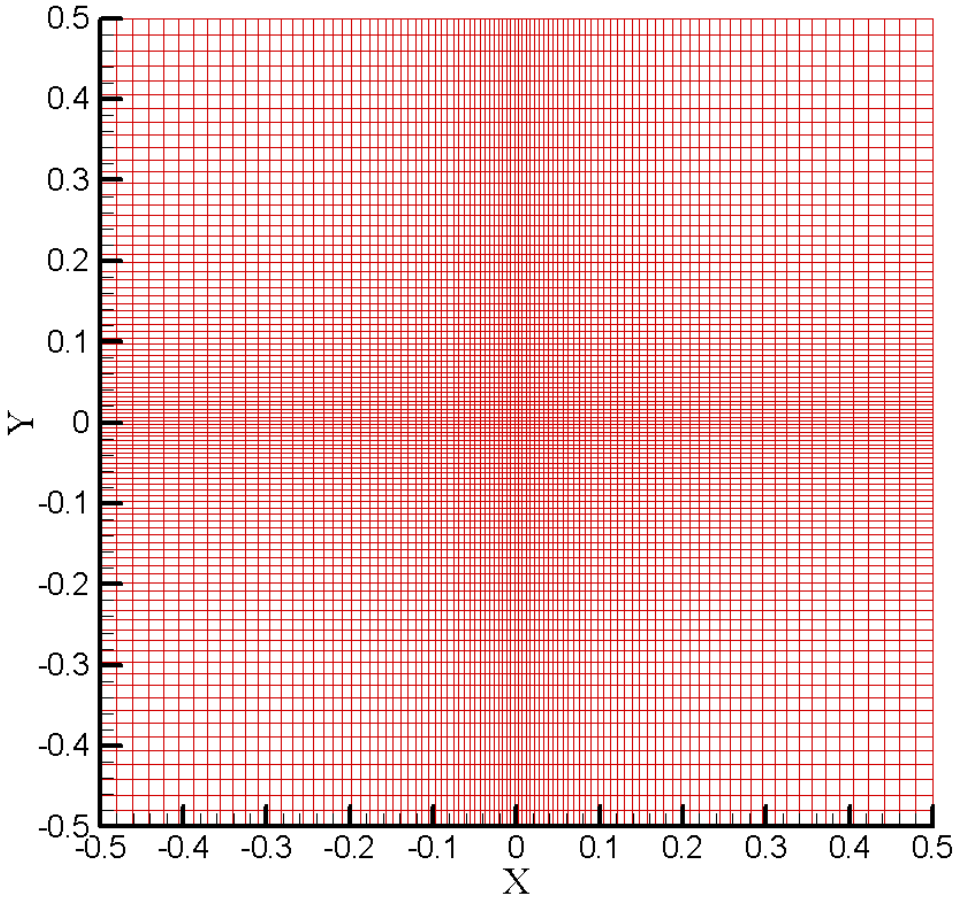


Figure 7.13: Sample grid for calculation of a moving vortex in uniform compressible flow.

The analytical solution and the initial conditions of a compressible vortex moving with a uniform free stream are presented in Appendix C. From Appendix C we see that the quantity $\omega / \rho$ of a vortex will be conserved as it convects in compressible, inviscid, non-conducting fluids. Figure 7.14 presents the contours of the quantity $\omega / \rho$ of the flow without confinement after the vortex has passed through the grid one cycle and approximately backed to the center of the computational domain. Figure 7.15 presents the same calculation, but after passing through the grid ten cycles. The degree of dissipation is quite obvious. Next, Figure 7.16 and Figure 7.17 present the results of the same calculations with the vorticity confinement in effect. These figures are essentially identical to each other, no dissipation are shown in these two figures.

The profile of the quantity $\omega/\rho$ along a diameter of the moving vortex is presented in Figure 7.18. From this figure we see that the solutions without confinement looks like the solution of the Navier-Stokes equations with the physical viscosity replaced by the numerical dissipation. However, we solved the Euler equations; no viscosity terms exist. Therefore, the solution should not have had the dissipative behavior similar to the solution of Navier-Stokes equations. On the other hand, the solutions with confinement do not show the dissipative behavior of the solutions without confinement, even though the vortex moved for ten cycles and backed to about the original place. Furthermore, the solution without confinement decreases as the vortex moves along with the uniform free stream, until all the value of $\omega/\rho$ is damped out, because no "force" exists to balance the numerical dissipation. On the other hand, the solution with confinement is approximately close to the analytical solution except that there are some wiggles at the region near $r = R_c$, which may be caused by the interaction of the free stream and the edge of the core of the vortex where exists a strong velocity and vorticity gradients. From this fact we may conclude that the vorticity confinement almost cancel most of the numerical dissipation errors to conserve the quantity $\omega/\rho$ of the vortex.

In order to see how vorticity confinement method works on a very coarse grid, we did the same calculation on very coarse grid 12x12. The profile of the quantity $\omega/\rho$ with confinement along a diameter of the vortex is presented in Figure 7.19. The solutions are actually dissipated, but essentially do not change with time. The vortical structure is captured within 4-6 grid cells and convects without changing the internal structure. This is our objective in design of the vorticity confinement method for practical flow situations in which thin concentrated vortical layers persist very long distances without significant dissipation. Actually, the conventional CFD numerical method cannot be used to obtain the solution without significant dissipation due to dissipative error of numerical discretization. This situation is more serious when the calculation is performed on a coarse grid. In a practical calculation, especially for 3D flow passing through a complex geometry, fine grid calculations may be very expensive, and computer storage may be an issue. However, with CVC, complex flow fields may be computed using coarse grids. In addition, Hu and Grossman presented some interesting results and discussion of CVC for a moving vortex with a uniform stream in Ref. [46].

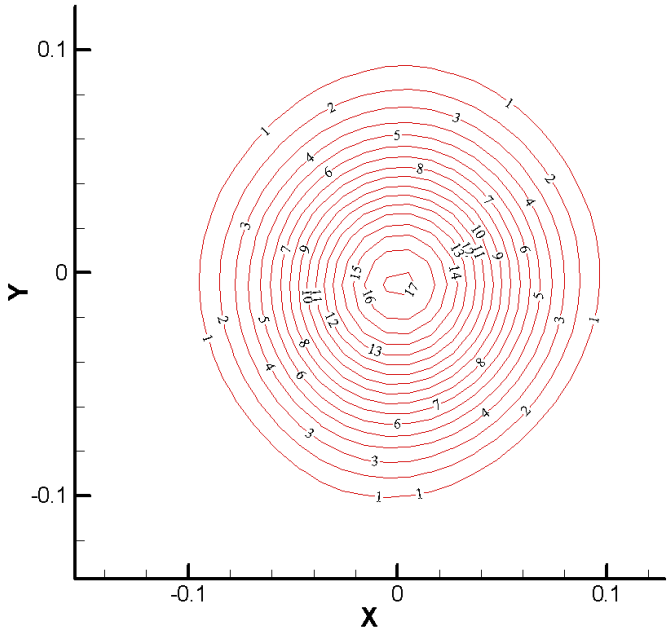


Figure 7.14: Contours of the quantity $\omega / \rho$ of a vortex moving with a uniform free stream after one cycle. No confinement.

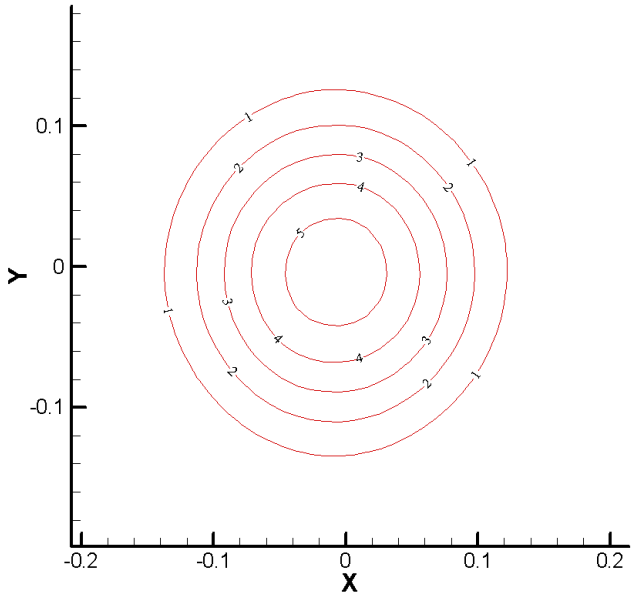


Figure 7.15: Contours of the quantity $\omega / \rho$ of a vortex moving with a uniform free stream after ten cycles. No confinement.

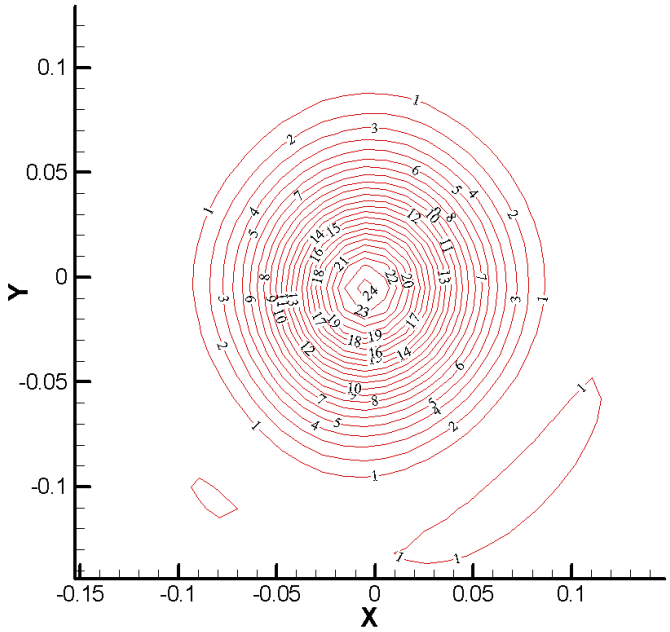


Figure 7.16: Contours of the quantity $\omega / \rho$ of a vortex moving with a uniform free stream after one cycle. With confinement.

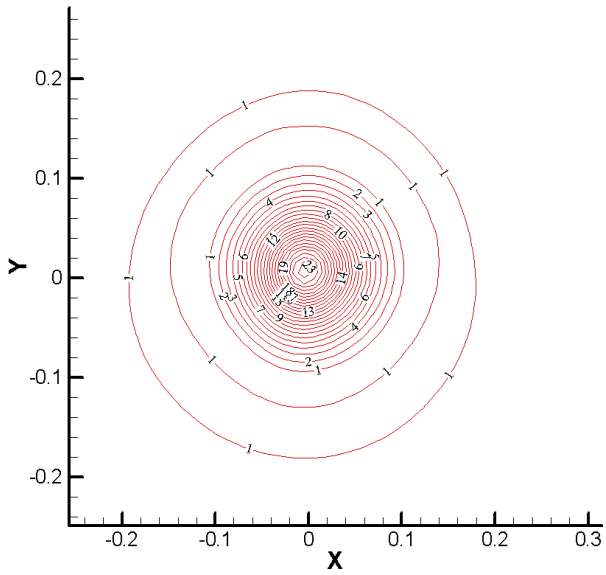


Figure 7.17: Contours of the quantity $\omega / \rho$ of a vortex moving with a uniform free stream after ten cycles. With confinement.

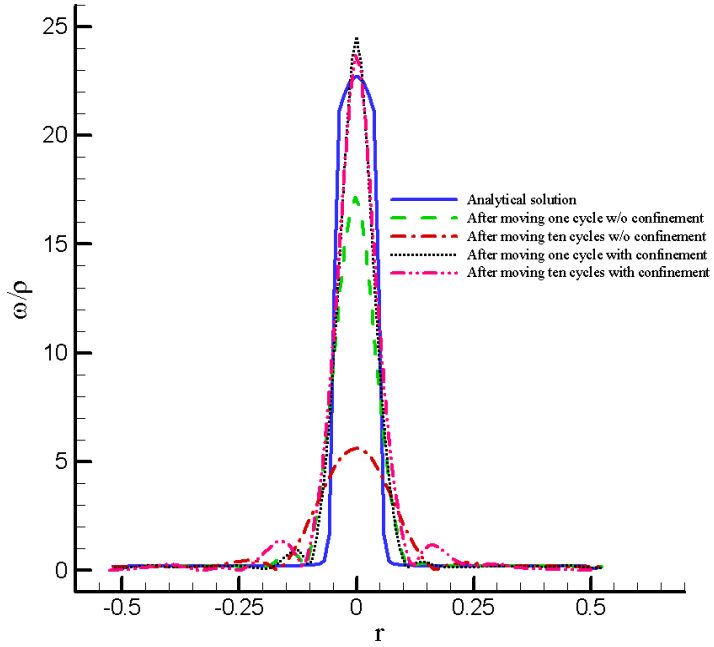


Figure 7.18: Profile of the quantity $\omega / \rho$ across the diameter of a moving vortex. Finer grid 100x100

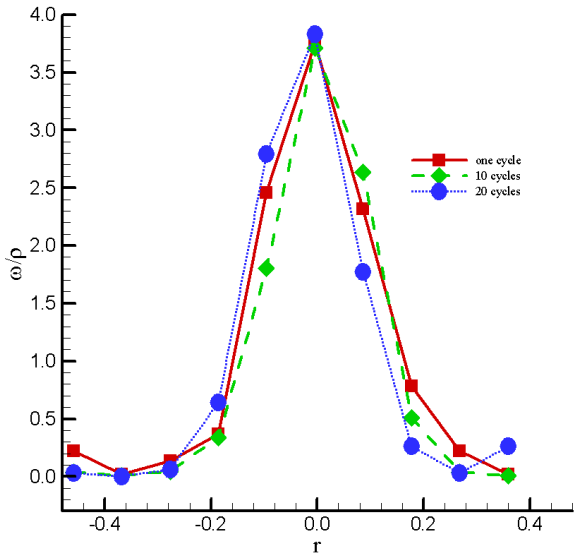


Figure 7.19: Profile along a vertical slice taken through the center of the vortex. Coarse grid 12x12.

The moving vortex problem also can serve as test of the numerical formulation. In Ref. [62], it was pointed out that for large values of confinement parameter, the present formulation may increase the total temperature of the flow. The initial investigations showed that small variations of $T_0$ occur, and, disturbingly, grow with iteration. It also appeared that using relatively large values of the confinement parameter $E_c$ for the body confinement procedure exacerbated this phenomenon [62]. The initial study indicated that the situation was improved by using a scalar implementation of the confinement, rather than the matrix form. Secondly, the situation was also improved by completely eliminating the rate of work done by the "body force" as it appears in the energy equation. Then a systematic procedure was developed by considering the following conditions:

1) The present formulation, i.e., rate of work term in the energy equation and matrix confinement;
2) Rate of work term in the energy equation and scalar confinement;
3) No rate of work term in the energy equation and matrix confinement;
4) No rate of work term in the energy equation and scalar confinement.

We have repeated the computation of the vortex moving in a uniform flow with the same data previously outlined but on uniform grid 100x100. The computation was executed for 15,000 iterations that correspond to approximately 9 circuits. We have observed that the different formulations give almost the same results in terms of the vortex confinement. We can conclude that all the formulations are effective in confining the vortex. However, the total temperature changes. We computed the average total temperature, $T^0_{avg}$, defined as follows:

$$T^0_{avg} = \frac{1}{(i_{\max}-1)(j_{\max}-1)} \sum_{i=1}^{i_{\max}-1} \sum_{j=1}^{j_{\max}-1} T^0_{i,j} , \tag{7.3}$$

where $T^0_{i,j}$ indicates the total temperature at each cell center (i , j), and $i_{\max}, j_{\max}$ are the maximum number of grid points in the x and y directions, respectively. Figure 7.20 presents the evolution of $T^0_{avg}$ during the computation. The formulation in 4) above, gives an almost constant total temperature trend, which follows from the physics of the problem. The introduction of the rate of work in the energy equation determines increases of the total temperature. Increases can also be observed for the matrix confinement with no work inserted in the energy equation. Indeed, the matrix multiplication causes the fifth term of the vector S to be nonzero, although no work is explicitly inserted in the energy equation. For

computing smaller vortices (with respect to the grid size), larger values of the vortex confinement coefficient $E_c$ are required. Noting that the total temperature increase is roughly proportional to $E_c$. Significant errors may be expected if the work term is inserted into the energy equation and if the matrix confinement is applied. Errors as large as 35% have been experienced in the body confinement computations [62]. Indeed, this computation required $E_c$ values two orders of magnitude larger and the observed total temperature errors were approximately two orders of magnitude larger.

The second case that we calculated for investigating the effect of work done by the "body force" on the total temperature is the flow over a flat plate. We repeated the same calculation of the flow over a flat plate using the systematic procedures outlined above and a Cartesian grid 200x25. The confinement parameter in this case $E_c = 0.06$. Figure 7.21 presents the velocity profiles at 2L/3. From this figure we see that all the four confinement procedures produced the same confinement effect for turbulent velocity profile. However, Figure 7.22 shows that the work rate inserted in energy equation increases the total temperature. The tendency of increasing total temperature in this case is the same as that of the moving vortex. However, until now we found that the total temperature increases less than 2% except when the body confinement [62] with a very large confinement parameter was used. The flows over the flat delta wings were calculated using CVC with work rate in energy equation. This case includes subsonic, transonic and supersonic flows. Furthermore, there are bow shock, cross-flow shocks and shock-vortex interactions in the flow field. Therefore, the flows are highly compressible. However, the pressure coefficients of the present study agreed well with experiments and the other computed results.

In addition to the description above, Dadone, Hu and Grossman presented some interesting results and discussions for a better understanding vorticity confinement in compressible flows including body confinement [62].

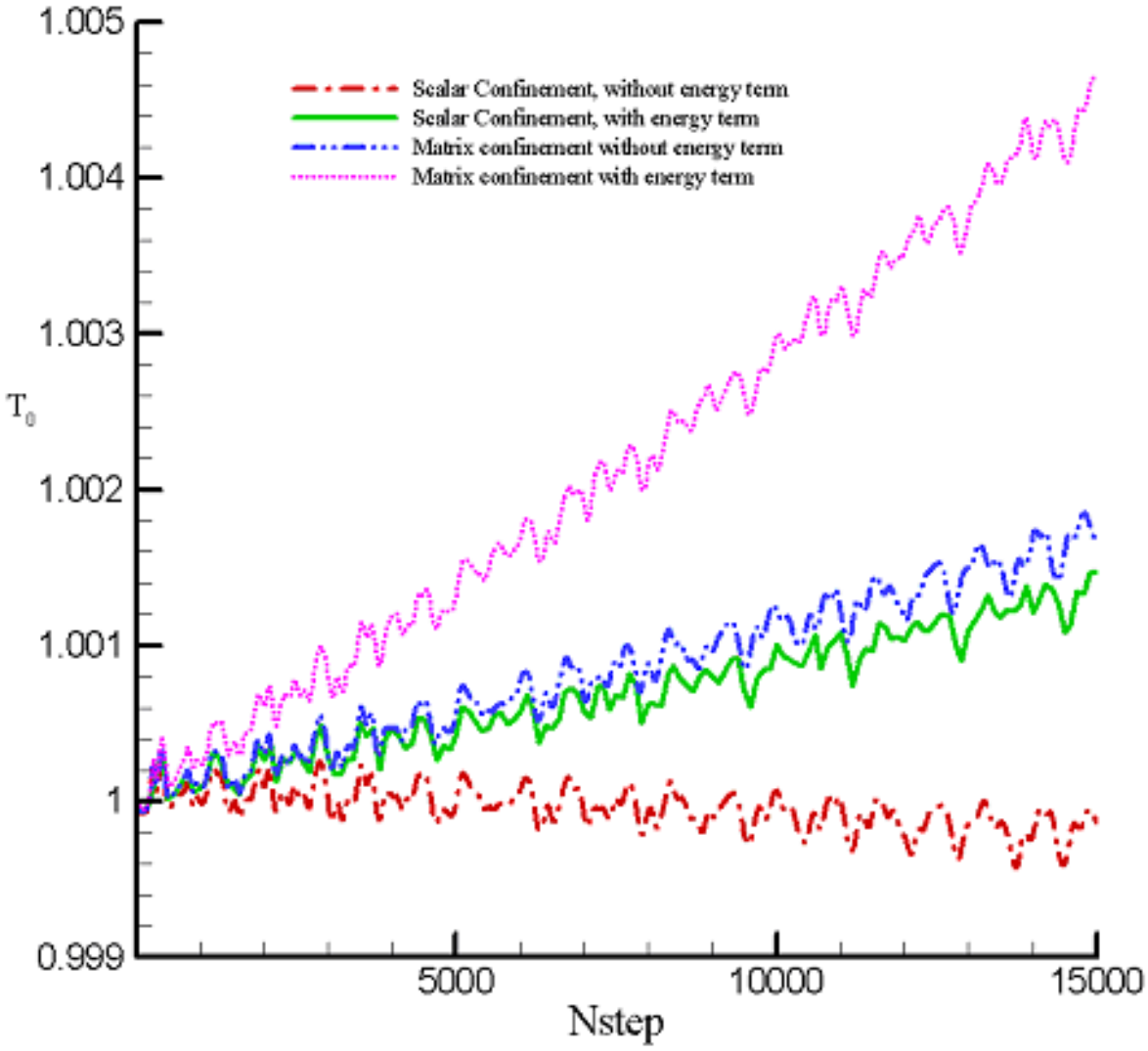


Figure 7.20: The average total temperature versus time iterations for different vorticity confinement procedures for a moving vortex.

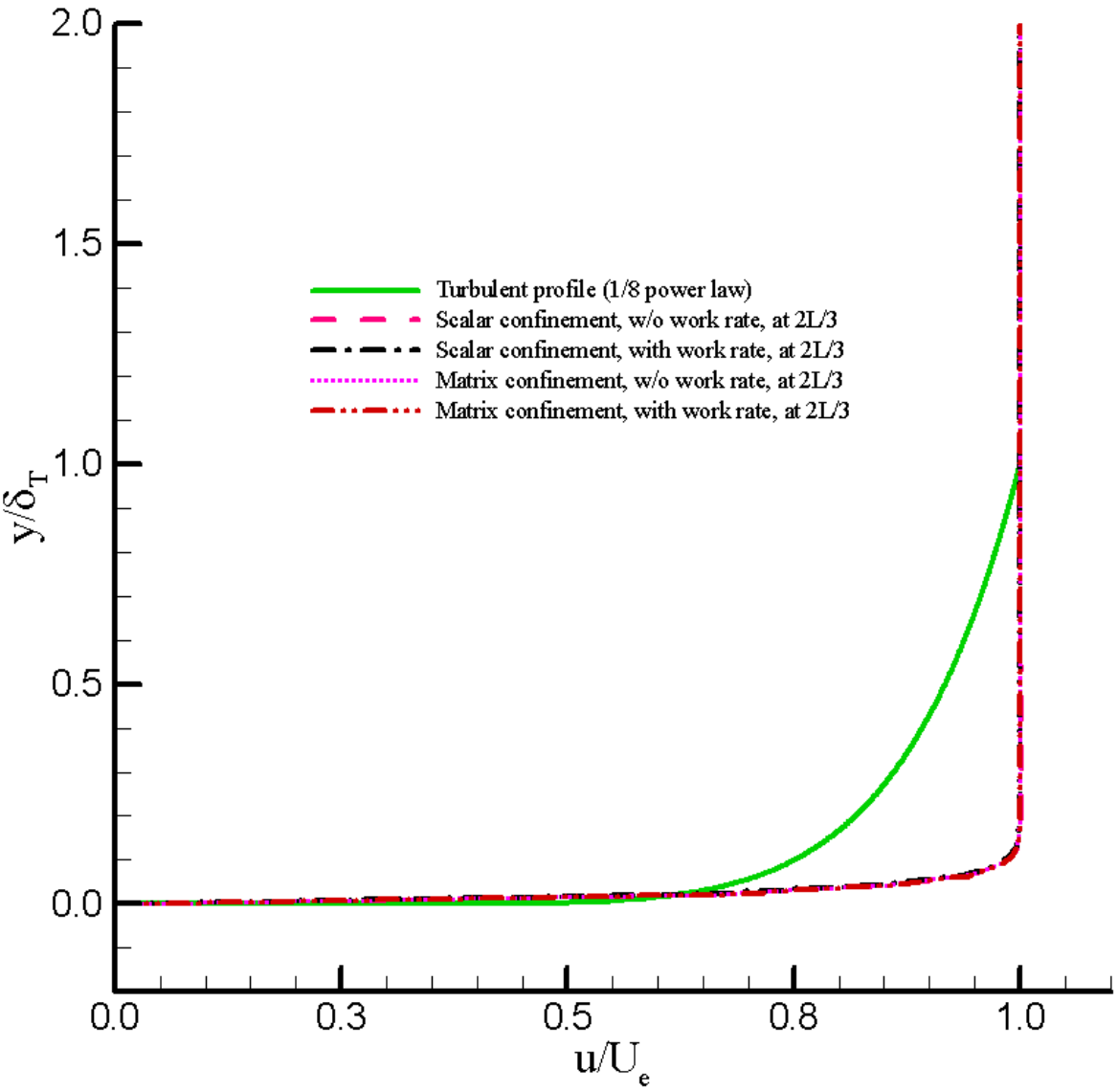


Figure 7.21: The velocity profile at 2L/3 for different vorticity confinement procedures.

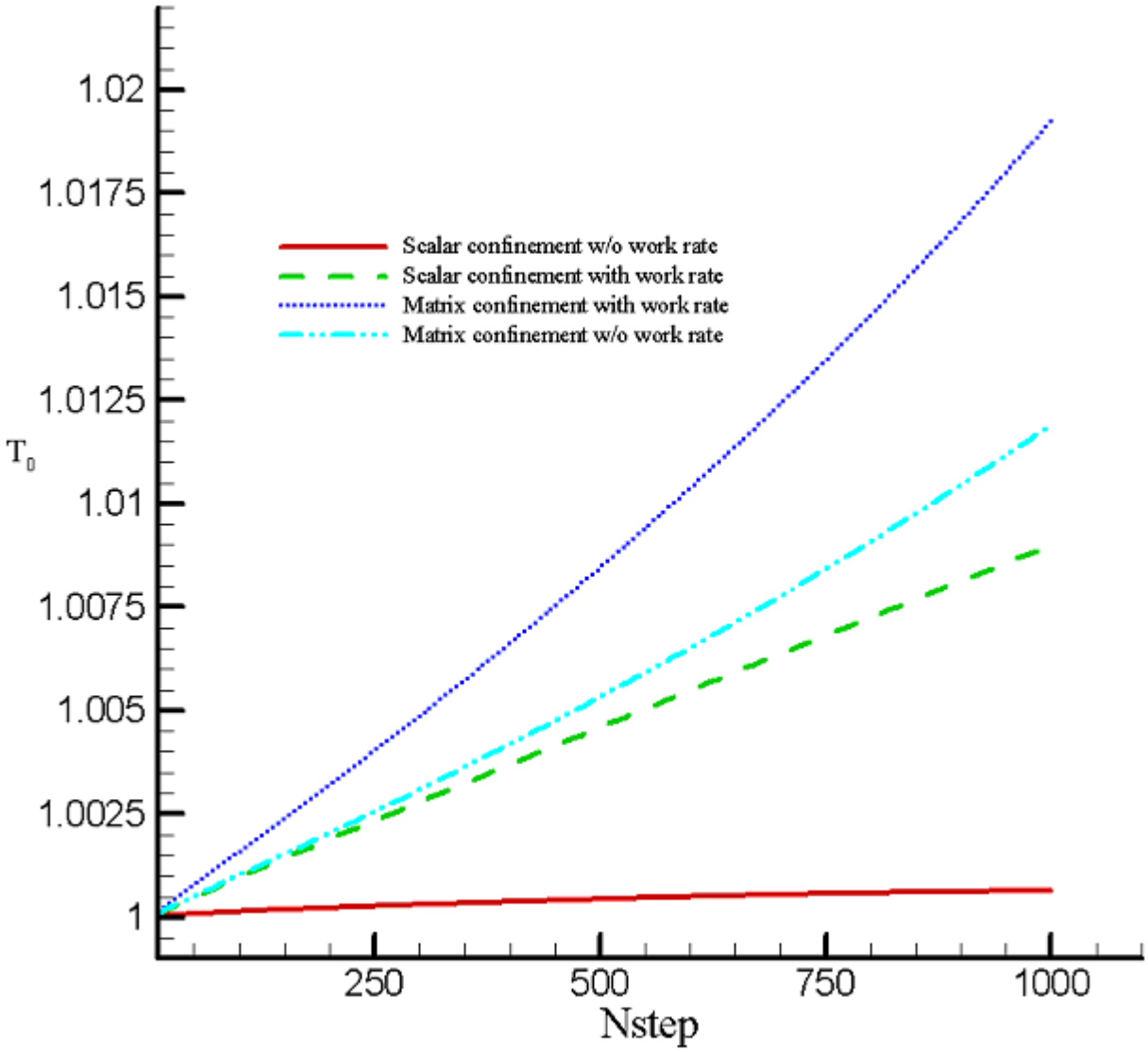


Figure 7.22: The average total temperature versus time iterations for different vorticity confinement procedures applied to the flow over a flat plate.

# Chapter 8

# Summary and Conclusions

An economical, accurate and robust numerical method for Compressible Vorticity Confinement (CVC) in vortex–dominant flows was presented. We extended the incompressible vorticity confinement approach of Steinhoff by adding a vorticity confinement term as a "body force" into the conservation laws for compressible flows. This method is especially designed for vortex-dominant flows, with the confinement term only effecting the portion of the flow where the vorticity gradient is large. This vorticity confinement term tends to cancel the numerical dissipative errors inherently related to the numerical discretization in regions with strong vorticity gradients.

We used two methods to assess the accuracy, reliability and efficiency of the CVC method. In one approach, we directly applied the CVC method to a number of applications involving complicated vortex structures and evaluated the accuracy by comparing the present results with existing experimental data and with other computational results. The applications of CVC considered include supersonic conical flows over delta wings, shock-bubble and shock-vortex interactions, the turbulent flow past a square cylinder and the turbulent flow over a cube mounted on the floor of a channel. In the second approach, we evaluated the effectiveness of the CVC method by solving simplified "model problems" and comparing with the "exact" solutions. Problems that we have considered are a two-dimensional supersonic shear layer, flow over a flat plat and a single two-dimensional vortex moving with a uniform stream.

The effectiveness of the CVC method for flows involving complex vortical layers and the interaction with shock waves was evaluated on several complex flow applications. First the supersonic conical flows over flat delta wings were investigated using CVC. This problem is of great interest to CFD researchers because the flow separates from the leading edge of the wing and forms two primary vortices with the secondary separation beneath them when the wing flies at large angles of attack and supersonic speeds. In this complex supersonic vortex dominated flow, the pressure coefficient not only depends on the primary vortex, but also depends on the cross-flow shocks and their interaction, particularly the strength and the

position of the primary vortex and cross-flow shocks. The results presented here in Chapter 3 show obvious improvement over the results obtained using local grid refinement by Powell [11], because the present approach obtained about the same suction peak, the same position and the size of the primary vortex as the measured ones in the experiments. On the other hand, the results without confinement show a more outboard of the position of the primary vortex and larger size of the primary vortex than the experiments. Next we used CVC to simulate shock-bubble and shock-vortex interaction. These types of problems are typical problems for investigating the complex mechanisms of the combustion process in engine chambers, which have attracted a lot of attentions in the CFD community. As described in Chapter 4, the results obtained using a higher order finite-difference FCT algorithm by Yang *et al.* [9] show too much dissipation in the steep vorticity gradient region. James *et al.* [48] utilized a sophisticated mesh refinement algorithm to simulate the complex vortical layers, and Povitsky and Ofengeim [8] used a complex unstructured adaptive algorithm to calculate the similar problems. Although they reproduced the intricate vortex structures that were observed in the experiments, the higher order schemes increase CPU time significantly, and the local grid refinement and adaptive algorithms are time-consuming and difficult to implement. However, in the present study, the finite-volume algorithm with the simple CVC method was used to solve these kinds of problems on a regular Cartesian grid, using much less CPU time, and with favorable agreement with the experiment and other computational results. Vorticity confinement appears to play an important role in effectively solving these problems.

The accuracy and effectiveness of the CVC method for the complex vortex dominated flows with massive separation from sharp edges were investigated on two flow problems: One is the turbulent flow past a 2D square cylinder which involves periodic vortex shedding, the other is the turbulent flow over a cube mounted on the floor of a channel which involves complex horseshoe vortex, primary separation and secondary separation in front of the cube and the arch vortices, corner vortices downstream of the cube. Both cases are the standard test cases chosen by LES workshop in 1996. There is much experimental data and other computational results of RANS and LES available to evaluate the present approach [3,4,5,13,14,15,49,50,51,54,55,56,57,58]. In the discussion of Chapter 5 we noted that the RANS calculations for bluff bodies completely failed, and that LES calculations cannot provide complete overall good flow field for the flow past a square cylinder. In addition, LES calculations must utilize a huge number of grid points in 3D flow problems to capture the large-scale vortex structures and model the sub-grid scales. However, in the present study, we considered the problem by adding a CVC term as a “body force” to the conservation laws for inviscid flows, with no-slip conditions enforced on solid walls,

and with a coarse grid appropriate for inviscid flows. We found that for values of confinement parameter in a range, $E_c$ = 0.001-0.01, the turbulent flow with periodic vortex shedding past a square cylinder was reproduced with good agreement with experimental data, including the unsteady flow structures, the drag coefficient, the vortex shedding frequency and the velocity distribution along the centerline of the square cylinder. For the turbulent flow over a cube mounted on the floor of a channel, the complex flow patterns and velocity profiles were in good agreement with time-averaged values of the experimental data and with LES simulations, even though the CVC approach utilized about a factor of 50 fewer than LES calculation cells (about 20,000 compared to over 1 million).

In order to better understand the applicability and limitations of the CVC, we performed the calculations of several simple "model problems" and compared numerical solutions with the "exact" solutions. The model problems we have considered include a turbulent boundary layer over a 2D flat plate, a supersonic shear layer and a single circular vortex moving with a uniform free stream. The effects of the grid spacing and the value of the confinement parameter on the velocity profiles of the flow over a 2D flat plate were investigated. The results show that the CVC method appears to act as a crude turbulent model in the near wall region for values of confinement parameter in the range $E_c$ = 0.06 - 0.24. This rough approximation to a turbulent boundary layer model appears to be accurate enough to generate separation of large-scale structures from sharp edges. For the massive separation cases considered in Chapter 5, The CVC method was then able to accurately predict the convection of the large-scale structures as an essentially inviscid rotational flow.

The study of a supersonic shear layer was used to evaluate the classical accuracy of the CVC method and demonstrate the low dissipation property of the CVC method in the strong vorticity gradient region. The basic solvers used in the present study are second-order finite-volume schemes, but the results without confinement show too much dissipation, and an initial profile which becomes dissipated with space and time. However, the results with confinement show no degradation of the initial profile of the supersonic shear layer. CVC appears to cancel most of the dissipation errors of the basic solver in the vortical regions. Classical accuracy was evaluated by evaluating the solution over a range of grids and confinement parameters. The CVC method was found to be nearly second-order accurate over a range of $0.1 \le E_c \le 0.3$ and was more accurate than the no confinement baseline, $E_c$ = 0. The high accuracy of the CVC approach was further confirmed by the study of a single circular vortex moving with a uniform stream. In the problem of a single vortex moving with a uniform stream, the numerical solution with

confinement was shown to be a good approximation to the "exact" solution of the problem, even as the vortex moved for ten cycles through the grid. The quantity $\omega / \rho$ in the core region of the vortex was conserved for the CVC method, whereas the numerical solution without confinement was damped dramatically after the vortex moved for ten cycles. It was also pointed out in Chapter 7 that the present formulation may slightly increase stagnation temperature for this case. It was found that this effect was only significant for conditions involving large values of $E_c$. It was determined that by using only the confinement term in the momentum equation and removing the term from the energy equation, along with a scalar rather than matrix confinement implementation, this phenomenon was effectively eliminated.

It is recognized that parallel computing is necessary for intensive computer simulation in CFD research and its engineering applications, especially for complex turbulent flows that require huge computations. In the present research, the domain decomposition with one-to-one and pipeline schemes was investigated, along with the effects of synchronization and communication overhead on the parallel computing performance were studied. The discussion in Chapter 6 shows that the performance of parallel computing strongly depends on the specific algorithms and the actual implementation, and that the type of the scheme, the size of the sub-domain, synchronization and load balancing all play very important roles and are correlated in achieving high parallel computing performance, and that a pipeline scheme without synchronization achieved the best performance in a simple domain and a structured grid. The parallel computing portion of this work was implemented in order to show potential benefits for CVC. However, the study was not meant to be broad based and inclusive.

From the summary above, we can draw the following conclusions:

- CVC is effective in simulating vortex dominated flows in high speeds, involving shocks, vortices and their interactions. The numerical experiments include the calculations of the supersonic conical flows over delta wings and the flows involving shock-bubble and shock-vortex interaction. The good agreement of the present results with the experiments and the other computational results demonstrates the applicability and the robustness of the CVC method for vortex-dominant flows in high speeds.
- CVC works for the vortex dominated flows with massive separation from sharp edges, even though an essentially inviscid formulation was used, with a no-slip condition on solid walls, and a

coarse inviscid-type grid. The applications include the flow past a square cylinder and the flow over a cube on the floor of a channel. The agreement of the CVC results with experimental data and other computational results of RANS and LES indicates the simplicity and effectiveness of this method. The present results of the flow over a flat plate show that CVC may be thought as a crude turbulent model in the near wall region.

- CVC is a significantly simpler approach than high order schemes, local grid refinement algorithms, unstructured adaptive algorithms, RANS approaches and LES simulations, but it can achieve favorable agreement with these methods for vortex-dominant flows with strong vorticity gradients using much less computer resources.
- A major drawback of the CVC approach is that at present one must ascertain the value of confinement parameter for each problem by numerical experimentation. This can be time consuming for complex 3D vortex dominated flows.

## Suggestions for Future Study:

There could be two interesting possibilities for future study about CVC presented in this dissertation:

- Find ways to determine the value of confinement parameter for a variety of problems. First, attempt to scale $E_c$ with mesh parameters for non-uniform grids. Then try to find ways to correlate values of $E_c$ with problem parameters such as Mach number and Reynolds number.
- Develop simplified boundary condition treatments to enable CVC to utilize uniform Cartesian grids, even for problems with complex geometries. One possibility is to find ways of extending the “body confinement” approach [27] to compressible flows.

# Bibliography

[1] Paul E. Rubbert, "CFD and the Changing World of Airplane Design," AIAA Wright Brothers Lecture, Anaheim, California, September 18-23, 1994.

[2] Miller D.S. and Wood R.M., "Lee-side Flow Over Delta Wing at Supersonic Speeds," NASA TP2430, NASA Langley Research Center, Jun. 1985.

[3] D.F.G. Durao, M.V. Heitor and J.C.F. Pereira, "Measurements of Turbulent and Periodic Flows around a Square Cross-section Cylinder," *J. Experiments in Fluids*, **6**, 1988, pp. 298-304.

[4] A. Larousse, R. Martinuzzi and C. Tropea, "Flow Around Surface-Mounted, Three-Dimensional Obstacles," in *Turbulent Shear Flows*, **8**, Selected Papers From Eighth International Symposium on Turbulent shear Flows edited by F. Durst, R. Friedrich, B.E. Launder, F.W. Schmidt, U. Schumann, J.H. Whitelaw, 1991, pp.137-139.

[5] R. Martinuzzi and C. Tropea, "The Flow around Surface-Mounted, Prismatic Obstacles Placed in a Fully Developed Channel Flows," *J. Fluids Engineering*, Vol.115, 1993, pp. 85-92.

[6] Rai M.M., "Navier-Stokes Simulation of Blade-vortex Interaction Using Higher-order Accurate Upwind Schemes, "AIAA paper No.87-0543, 1987.

[7] Strawn R.C "Wing Tip Vortex Calculation With an Unstructured Adaptive Grid Euler Solver," presented at the 47-th AHS forum of the American Helicopter Society, 1991.

[8] A. Povitsky, D. Ofengeim "Numerical Study of Interaction of a Vortical Density Inhomogeneity With Shock and Expansion Waves," NASA/CR-1998-206918, ICASE Report No.98-10.

[9] Joseph Yang, Toshi Kubota and Edward E. Zukoski, "A Model for Characterization of a Vortex Pair Forward by Shock Passage Over a Light-Gas Inhomogeneity," *J. Fluid Mech.* Vol.258, 1994, pp. 217-244.

[10] J. W. Jacobs, "Shock-induced Mixing of a Light-Gas Cylinder," *J. Fluid Mech.*, Vol.234, 1992, pp. 620-649.

[11] Powell K.G., *Vortical Solutions of the Conical Euler Equations*, Notes on Numerical Fluid Mechanics, Volume 28.

[12] Chi-Wang Shu, "High Order Finite Difference and Finite Volume WENO Schemes and Discontinuous Galerkin Methods for CFD, " NASA/CR-2001-210865, ICASE Report No. 2001-11, May, 2001.

[13] W. Rodi, "Comparison of LES and RANS Calculations of the Flow Around Bluff Bodies," *J. Wind Eng. and Ind. Aerodyn*. **69/71**,1997, pp. 55-75.

[14] R. Franke, W. Rodi, "Calculation of Vortex Shedding Past a Square Cylinder with Various Turbulence Models," in *Turbulent Shear Flows*, **8**, Selected Papers From Eighth International Symposium on Turbulent shear Flows edited by F. Durst, R. Friedrich, B.E. Launder, F.W. Schmidt, U. Schumann, J.H. Whitelaw, 1991, pp. 189-204.

[15] D. Lakehal, W. Rodi, "Calculation of the Flow past a Surface-Mounted Cube with Two-Layer Turbulence Models," *J. Wind Eng. and Ind. Aerodyn.*, **67/68**, 1997, pp. 65-78.

[16] Kim, J., Moin, P. and Moser, R., "Turbulence Statistics in Fully Developed Channel Flow at Low Reynolds Number, " *J. Fluid Mech*., Vol.177, 1987, pp. 133-166.

[17] Speziale, C.G., "Modeling the Pressure-Gradient-Velocity Correction of Turbulence," *J. Physics of Fluids*, Vol. 28, 1985, pp. 69-71.

[18] Leonard, A., "Vortex Methods for Flow Simulation, " *J. Computational Physics*, Vol. 37, 1980, pp. 289-335.

[19] Krasny R., "Vortex Sheet Computation: Roll-up, Wakes, and Seperation," Lecture in Applied Mathematics, Vol.28, 1991, pp. 383.

[20] Steinhoff J. and Ramachandran K. "A Vortex Embedding Method for Free-wake Analysis of Helicopter Rotor Blades in Hover," Vertica, Vol.13, 1989.

[21] Steinhoff J., Wang C., Underhill D., Mersch T. and Wenren Y., "Computational Vorticity Confinement: a Non-diffusive Eulerian Method for Vortex Dominated Flows," Preprint, Tullahoma, TN, 1992.

[22] Steinhoff J. and Mersch T., "Computation of Incompressible Flow Over Delta Wings Using Vorticity Confinement," AIAA paper, No.94-0646, 1994.

[23] Steinhoff J., "Vorticity Confinement: a New Technique for Computing Vortex Dominated Flows," in *Frontiers of Computational Fluid Dynamics* (Caughy D. and Hafez M., eds), pp. 235-263, New York: John Wiley and Sons, 1994.

[24] Steinhoff J., Raviprakash G. and Burley C., "Navier-Stokes Computation of Blade-Vortex Interactions Using Vorticity Confinement," In Proc. 33rd Aerospace Science Meeting, Jan.1995.

[25] Puskas E., Steinhoff J., Underhill D. and Wenren Y. "Computation of Short Accoustic Pulses," in Proceedings, 6th International Symposium on Computational Fluid Dynamics, (Lake Tahoe, NV), 1995.

[26] Steinhoff J., Wenren Y., Wang L., "Efficient Computation of Separating High Reynolds Number Incompressible Flows Using Vorticity Confinement," AIAA paper No. 99-3316, 1999.

[27] Wenren Y., Steinhoff J., Wang L., Fan M., Xiao M. "Application of Vorticity Confinement to the Prediction of the Flow over Complex Bodies," AIAA paper, No.2000-2621, 2000.

[28] Wenren Y., Fan M., Diets W., Hu, G., Braun C., Steinhoff J., Grossman B., "Efficient Eulerian Computation of Realistic Rotorcraft Flows Using Vorticity Confinement," AIAA paper, No.2001-0996, 2001.

[29] Kim, J. *et al.*, "Application of a Fractional-Step Method to Incompressible Navier-Stokes Equations," *Journal of Computational Physics*, Vol. 59, 1985.

[30] Pevchin S., Grossman B. and Steinhoff J., "Capture of Contact Discontinuities and Shock Waves Using a Discontinuity Confinement Procedure," AIAA paper 97-0874, Jan. 1997.

[31] Yee K. and Lee D.H. "Euler Calculation For a Hovering Coaxial Rotor Flow Field With New Boundary Condition," Paper AE04, 24th European Rotorcraft Forum, Sep.1998.

[32] Jameson A., Schmit W. and Turkel E., "Numerical Solutions of the Euler Equations by Finite Volume Methods Using Runge-Kutta Time-stepping Scheme," AIAA paper, No. 81-1359, 1981.

[33] E.Turkel, "Accuracy of Scheme with Nonuniform Meshes for Compressible Fluid Flows," Technique Report 85-43, ICASE, 1985.

[34] Turkel E., "Improving the Accuracy of Central Differences Schemes," in Lecture Notes in Physics, Vol.323, pp. 586-591, New York: Springer-Verlag, 1988.

[35] Turkel E. and Vatsa V., "Effect of Artificial Viscosity on Three-Dimensional Flow Solutions," *AIAA Journal*, Vol. 32, No. 1, pp. 39-45, 1994.

[36] Caughey D. A., Turkel E., "Effects of Numerical Dissipation on Finite-Volume Solutions of Compressible Flow Problems," AIAA paper, No. 88-0621, 1988.

[37] A. Rizzi, "Three-Dimensional Solution to the Euler Equations with One Million Grid Points," *AIAA Journal*, Vol.23, No.13, pp. 1986, Dec.1985.

[38] A. Rizzi and L.E. Eriksson, "Computation of Flow around Wings Based on the Euler Equations," *Journal of Fluid Mechanics*, Vol.148, pp. 45-72, Nov. 1984.

[39] E.M. Murman, A. Rizzi, and K.G. Powell, "High Resolutions of the Euler Equations for Vortex Flows," in *Progress and Supercomputing in Computational Fluid Dynamics*, pp. 93-113, Birkhauser-Boston, 1985.

[40] R.W. Newsome, "A Comparison of Euler and Navier-Stokes Solutions for Supersonic Flow Over a Conical Delta Wing," AIAA Paper 85-0111, Jan. 1985.

[41] O.A. Kandil and A. Chuang, "Influence of Numerical Dissipation in Computing Supersonic Vortex-Dominated Flows," AIAA paper 86-1073, May 1986.

[42] R.W. Newsome and J.L. Thomas, "Computation of Leading-Edge Vortex Flows," CP2416, NASA, 1985.

[43] S.R. Chakravarthy and D.K. Ota, "Numerical Issues In Computing Inviscid Supersonic Flow Over Conical Delta Wings," AIAA paper 86-0440, Jan. 1986.

[44] F. Marconi, "The Spiral Singularity in the Supersonic Inviscid Flow over a Cone," AIAA paper 83-1665, Jul. 1983.

[45] Grossman, B., "A numerical Procedure for the Computation of Supersonic Conical Flows," *Journal AIAA*, Vol. 17, No. 8, pp. 828-837, Aug., 1979.

[46] G. Hu and B. Grossman, "A Numerical Method for Vortex Confinement in Compressible Flow," AIAA Paper 2000-0281, Jan. 2000, Reno, NV, USA.

[47] William B. Brower Jr., *Tables and Data for Compressible Flow*, Hemisphere Publishing Corporation, 1990.

[48] James J., Quirk and S. Karni, "On the Dynamics of a Shock-bubble Interaction," *J. Fluid Mech.* Vol.318, 1996, pp.139-163.

[49] D.A. Lyn and W. Rodi, "The Flapping Shear Layer by Flow Separation From the Forward Corner of a Square Cylinder," *J. Fluid Mech.*, Vol. 267, pp. 353-379, 1994.

[50] D.A. Lyn, S. Einav, W. Rodi and J.H. Park, "A Laser-Doppler Velocimetry Study of Ensemble-Averaged Characteristics of the Turbulent Near Wake of a Square Cylinder," *J. Fluid Mech.*, Vol. 304, pp. 285-319, 1995.

[51] G. Bosh, "Experimentelle und Theoretische Undersuchung der Instationaren Stromung Um /ylindrische Strukturen," Dissertation, University of Karlsruhe, 1995.

[52] Leonard, B. P., " A Stable and Accurate Convection Modeling Procedure Based on Quadratic Upstream Interpolation," Comput. Mech. Appl. Mech. Engrg., 19, pp. 59-98, 1973.

[53] Joel H. Ferziger and Milovan Peric, *Computational Methods for Fluid Dynamics*, Second edition, Springer, pp. 71-76, 1999.

[54] S. Murakami, A. Mochida, "On Turbulent Vortex Shedding Flows Past 2D Square Cylinder Predicted by CFD," *J. Wind Eng. and Ind. Aerodyn.*, **54/55**, pp. 91-211, 1995.

[55] SangSan Lee, "Unsteady Aerodynamic Force Prediction on a Square Cylinder Using $k-\varepsilon$ Turbulence Models," *J. Wind Eng. and Ind. Aerodyn*., **67/68**, pp. 79-90, 1997.

[56] P.W. Bearman, E.D. Obasaju, "An Experimental Study of Pressure Fluctuations on Fixed and Oscillating Square-section Cylinders," *J. Fluid Mec*h., **119** (1982), pp. 297 –313.

[57] Kishan B. Shah, Joel H. Ferziger, "A Fluid Mechanician's View of Wind Engineering: Large Eddy Simulation of Flow Past a Cubic Obstacle," *J. Wind Eng. And Ind. Aerodyn*., **67/68**, 1997, pp. 211-224.

[58] H. Werner and Wengle, "Large-Eddy Simulation of Turbulent Flow over and Around a Cube in a Plate Channel," in *Turbulent Shear Flows*, **8**, Selected Papers From Eighth International Symposium on Turbulent Shear Flows, edited by F. Durst *e* R. Friedrich, B.E. Launder, F.W. Schmidt, U. Schumann, J.H. Whitelaw, 1991, pp.156-168.

[59] S.Z. Yu, A.D. Kowalski, and R.L. Peskin, "An Investigation of Parallel Iterative Algorithms for CFD, " in *Parallel Computational Fluid Dynamics*, edited by Horst, D. Simon, the MIT Press, Cambridge, Massachusettes, London, England, 1992, pp. 215 - 232.

[60] V. Naik, N. Naik, and M. Nicoules, "Implicit CFD Applications on Message Passing Multiprocessors Systems," in *Parallel Computational Fluid Dynamics*, edited by Horst, D. Simon, the MIT Press, Cambridge, Massachusettes, London, England, 1992, pp. 97 – 135.

[61] MPI reference: http://www-unix.mcs.anl.gov/mpi/

[62] A. Dadone, G. Hu and B. Grossman, " Towards a Better Understanding of Vorticity Confinement methods in Compressible Flow," AIAA paper 2001-2639, Reno, USA, 2001.

# Appendix A

# Characteristic Matrix and Dissipation Models

The characteristic matrix $\hat{A}$ can be written as follows:

$$\hat{A}=\begin{pmatrix} \hat{n}_t & \hat{n}_x & \hat{n}_y & \hat{n}_z & 0 \\ -u\hat{V}+\hat{n}_x\Phi^2 & \hat{n}_t+\hat{V}-\gamma_2\hat{n}_x u & u\hat{n}_y-\gamma_1 v\hat{n}_x & u\hat{n}_z-\gamma_1 w\hat{n}_x & \gamma_1\hat{n}_x \\ -v\hat{V}+\hat{n}_y\Phi^2 & v\hat{n}_x-\gamma_1 u\hat{n}_y & \hat{n}_t+\hat{V}-\gamma_2\hat{n}_y v & v\hat{n}_z-\gamma_1 w\hat{n}_y & \gamma_1 n_y \\ -w\hat{V}+\hat{n}_z\Phi^2 & w\hat{n}_x-\gamma_1 u\hat{n}_z & w\hat{n}_y-\gamma_1 v\hat{n}_z & \hat{n}_t+\hat{V}-\gamma_2\hat{n}_z w & \gamma_1 n_z \\ -h_0\hat{V}+\hat{V}\Phi^2 & h_0\hat{n}_x-\gamma_1 u\hat{V} & h_0\hat{n}_y-\gamma_1 v\hat{V} & h_0\hat{n}_z-\gamma_1 w\hat{V} & \hat{n}_t+\gamma\hat{V} \end{pmatrix}, \qquad \text{(A.1)}$$

where $h_0$ is the total enthalpy in unit mass, $(\hat{n}_x,\hat{n}_y,\hat{n}_z)$ is the unit normal vector of the grid cell face, and $\hat{n}_t$ is zero for a fixed grid.

$$\left.\begin{aligned} &\hat{V}=\hat{n}_x u+\hat{n}_y v+\hat{n}_z w,\\ &h_0=e_0+p/\rho,\\ &\Phi^2=\frac{\gamma-1}{2}(u^2+v^2+w^2),\\ &\gamma_1=\gamma-1,\\ &\gamma_2=\gamma-2. \end{aligned}\right\} \qquad \text{(A.2)}$$

The eigenvalues of matrix $\hat{A}$ are denoted by $\lambda_1,\lambda_1,\lambda_1,\lambda_2,\lambda_3$ and are listed as follows:

$$\left.\begin{aligned}\lambda_1 &= \hat{n}_t + \hat{V},\\ \lambda_2 &= \hat{n}_t + \hat{V} + c,\\ \lambda_3 &= \hat{n}_t + \hat{V} - c,\end{aligned}\right\} \tag{A.3}$$

where c is speed of sound. Decomposing $\hat{A}$, we have

$$\hat{A} = R^{-1}\Lambda R, \tag{A.4}$$

where $\Lambda = diag[\lambda_1, \lambda_1, \lambda_1, \lambda_2, \lambda_3]$; R is the left eigenvector matrix of $\hat{A}$; $R^{-1}$ is the right eigenvector matrix of $\hat{A}$, they are given by

$$R = \frac{1}{c}\begin{pmatrix} \hat{n}_y & \hat{n}_z & \hat{n}_x & \beta & \beta \\ \hat{n}_y u + \hat{n}_z c & \hat{n}_z u - \hat{n}_y c & \hat{n}_x u & \beta(u + \hat{n}_x c) & \beta(u - \hat{n}_x c) \\ \hat{n}_y v & v n_z + \hat{n}_x c & \hat{n}_x v - \hat{n}_z c & \beta(v + \hat{n}_y c) & \beta(v - \hat{n}_y c) \\ \hat{n}_y w - \hat{n}_x c & w\hat{n}_z & w\hat{n}_x + \hat{n}_y c & \beta(w + \hat{n}_z c) & \beta(w - \hat{n}_z c) \\ b_{51} & b_{52} & b_{53} & b_{54} & b_{55} \end{pmatrix}, \tag{A.5}$$

$$R^{-1} = \frac{1}{c}\begin{pmatrix} a_{11} & \gamma_1\hat{n}_y u + n_z c & \gamma_1\hat{n}_y v & \gamma_1\hat{n}_y w - \hat{n}_x c & -\gamma_1\hat{n}_y \\ a_{21} & \gamma_1\hat{n}_z u - \hat{n}_y c & \gamma_1\hat{n}_z v + \hat{n}_x c & \gamma_1\hat{n}_z w & -\gamma_1\hat{n}_z \\ a_{31} & \gamma_1\hat{n}_x u & \gamma_1\hat{n}_x v - \hat{n}_z c & \gamma_1\hat{n}_x w + \hat{n}_y c & -\gamma_1\hat{n}_x \\ a_{41} & \beta(-\gamma_1 u - \hat{n}_x c) & \beta(-\gamma_1 v - \hat{n}_y c) & \beta(-\gamma_1 w - \hat{n}_z c) & \gamma_1\beta \\ a_{51} & \beta(-\gamma_1 u + \hat{n}_x c) & \beta(-\gamma_1 v + \hat{n}_y c) & \beta(-\gamma_1 w + \hat{n}_z c) & \gamma_1\beta \end{pmatrix},$$

where $\beta = \frac{1}{\sqrt{2}}$ and

$$\hat{V} = \hat{n}_x u + \hat{n}_y v + \hat{n}_z w, \tag{A.6}$$

$$
\left.
\begin{aligned}
b_{51} &= \hat{n}_y(h_0 - \frac{c^2}{\gamma_1}) + (\hat{n}_z u - \hat{n}_x w)c, \\
b_{52} &= \hat{n}_z(h_0 - \frac{c^2}{\gamma_1}) + (\hat{n}_x v - \hat{n}_y u)c, \\
b_{53} &= \hat{n}_x(h_0 - \frac{c^2}{\gamma_1}) + (\hat{n}_y w - \hat{n}_z v)c, \\
b_{54} &= \beta(\hat{V}c + h_0), \\
b_{55} &= \beta(-\hat{V}c + h_0),
\end{aligned}
\right\} \qquad \text{(A.7)}
$$

$$
\left.
\begin{aligned}
a_{11} &= -\hat{n}_y\Phi^2 + \hat{n}_y c^2 - \hat{n}_z uc + \hat{n}_x wc, \\
a_{21} &= -\hat{n}_z\Phi^2 + \hat{n}_z c^2 + \hat{n}_y uc - \hat{n}_x vc, \\
a_{31} &= -\hat{n}_x\Phi^2 + \hat{n}_x c^2 + \hat{n}_z vc - \hat{n}_y wc, \\
a_{41} &= \beta(\Phi^2 + \hat{V}c), \\
a_{51} &= \beta(\Phi^2 - \hat{V}c).
\end{aligned}
\right\} \qquad \text{(A.8)}
$$

Now let's turn to the matrix dissipation model $D$

$$
\begin{aligned}
D &= |A|d = R^{-1}|\Lambda|Rd \\
&= |\lambda_1|d + \frac{(|\lambda_2| - |\lambda_1|)}{2} l_1 \begin{pmatrix} 1 \\ \frac{u}{c} + \hat{n}_x \\ \frac{v}{c} + \hat{n}_y \\ \frac{w}{c} + \hat{n}_z \\ \frac{h_0}{c} + \hat{V} \end{pmatrix} + \frac{(|\lambda_3| - |\lambda_1|)}{2} l_2 \begin{pmatrix} 1 \\ \frac{u}{c} - \hat{n}_x \\ \frac{v}{c} - \hat{n}_y \\ \frac{w}{c} - \hat{n}_z \\ \frac{h_0}{c} - \hat{V} \end{pmatrix},
\end{aligned}
\qquad \text{(A.9)}
$$

where

$$h_0 = q^2 + \frac{c^2}{\gamma - 1}, \tag{A.10}$$

$$q^2 = \frac{u^2 + v^2 + w^2}{2}, \tag{A.11}$$

$$l_1 = (\frac{\gamma - 1}{c} q^2 - \hat{V}) d_1 + (-\frac{\gamma - 1}{c} u + \hat{n}_x) d_2 + (-\frac{\gamma - 1}{c} v + \hat{n}_y) d_3 + (-\frac{\gamma - 1}{c} w + \hat{n}_z) d_4 + \frac{\gamma - 1}{c} d_5, \tag{A.12}$$

$$l_2 = (\frac{\gamma - 1}{c} q^2 + \hat{V}) d_1 + (-\frac{\gamma - 1}{c} u - \hat{n}_x) d_2 + (-\frac{\gamma - 1}{c} v - \hat{n}_y) d_3 + (-\frac{\gamma - 1}{c} w - \hat{n}_z) d_4 + \frac{\gamma - 1}{c} d_5. \tag{A.13}$$

# Appendix B

# Cross-flow Vorticity and Governing Equations in Conical Coordinates

In this Appendix, we will give the details of the derivation of the cross-flow vorticity and governing equation in conical coordinates

Firstly, we introduce spherical coordinates, $r, \psi, \phi$ , such that

$$\left.\begin{aligned} x &= r\cos\psi, \\ y &= r\cos\phi\sin\psi, \\ z &= r\sin\phi\cos\psi. \end{aligned}\right\} \tag{B.1}$$

or equivalently

$$\left.\begin{aligned} r^2 &= x^2 + y^2 + z^2, \\ \tan\phi &= z/y, \\ \sin^2\psi &= (y^2 + z^2)/r^2. \end{aligned}\right\} \tag{B.2}$$

Now we introduce conical coordinates:

$$\left.\begin{aligned} r^2 &= x^2 + y^2 + z^2, \\ \xi &= y/x, \\ \eta &= z/x. \end{aligned}\right\} \tag{B.3}$$

Now we get the derivatives

$$\left.\begin{aligned} x_r &= \frac{1}{\sqrt{1+\xi^2+\eta^2}}, \\ y_r &= \frac{\xi}{\sqrt{1+\xi^2+\eta^2}}, \\ z_r &= \frac{\eta}{\sqrt{1+\xi^2+\eta^2}}, \end{aligned}\right\} \tag{B.4}$$

$$\left.\begin{aligned} x_\xi &= \frac{-r\xi}{\sqrt{(1+\xi^2+\eta^2)^3}}, \\ y_\xi &= \frac{r}{\sqrt{1+\xi^2+\eta^2}} - \frac{r\xi^2}{\sqrt{(1+\xi^2+\eta^2)^3}}, \\ z_\xi &= \frac{-r\eta\xi}{\sqrt{(1+\xi^2+\eta^2)^3}}, \end{aligned}\right\} \tag{B.5}$$

$$\left.\begin{aligned} x_\eta &= \frac{-r\eta}{\sqrt{(1+\xi^2+\eta^2)^3}}, \\ y_\eta &= \frac{-r\xi\eta}{\sqrt{1+\xi^2+\eta^2}}, \\ z_\eta &= \frac{r(1+\xi^2)}{\sqrt{(1+\xi^2+\eta^2)^3}}. \end{aligned}\right\} \tag{B.6}$$

Also, we know that the metric terms $h_r{}^2 = x_r{}^2 + y_r{}^2 + z_r{}^2$ , $h_\xi{}^2 = x_\xi{}^2 + y_\xi{}^2 + z_\xi{}^2$ and $h_\eta{}^2 = x_\eta{}^2 + y_\eta{}^2 + z_\eta{}^2$. After some algebraic work, we get:

$$\left.\begin{aligned} h_r &= 1, \\ h_\xi &= r\frac{(1+\eta^2)^{\frac{1}{2}}}{1+\xi^2+\eta^2}, \\ h_\eta &= r\frac{(1+\xi^2)^{\frac{1}{2}}}{1+\xi^2+\eta^2}. \end{aligned}\right\} \tag{B.7}$$

The unit vectors along the conical axes can be expressed in Cartesian coordinates as follows:

$$\left.\begin{aligned} \hat{i}_r &= \frac{1}{h_r}\frac{\partial \vec{r}}{\partial r} = \frac{1}{(1+\xi^2+\eta^2)^{1/2}}(\hat{i}+\xi\hat{j}+\eta\hat{k}), \\ \hat{i}_\xi &= \frac{1}{h_\xi}\frac{\partial \vec{r}}{\partial \xi} = \frac{1}{(1+\eta^2)^{1/2}(1+\xi^2+\eta^2)^{1/2}}(-\xi\hat{i}+(1+\eta^2)\hat{j}-\xi\eta\hat{k}), \\ \hat{i}_\eta &= \frac{1}{h_\eta}\frac{\partial \vec{r}}{\partial \eta} = \frac{1}{(1+\xi^2)^{1/2}(1+\xi^2+\eta^2)^{1/2}}(-\eta\hat{i}-\xi\eta\hat{j}+(1+\xi^2)\hat{k}). \end{aligned}\right\} \tag{B.8}$$

After checking $\hat{i}_r \cdot \hat{i}_\xi = 0$ and $\hat{i}_r \cdot \hat{i}_\eta = 0$, but $\hat{i}_\xi \cdot \hat{i}_\eta \neq 0$, we know that conical coordinates are not orthogonal. The vorticity vector is defined as follows:

$$\vec{\omega} = \nabla \times \vec{V} = \begin{pmatrix} \hat{i} & \hat{j} & \hat{k} \\ \frac{\partial}{\partial x} & \frac{\partial}{\partial y} & \frac{\partial}{\partial z} \\ u & v & w \end{pmatrix} = \omega_x \hat{i} + \omega_y \hat{j} + \omega_z \hat{k}, \tag{B.9}$$

where

$$\left.\begin{aligned} \omega_x &= w_y - v_z, \\ \omega_y &= u_z - w_x, \\ \omega_z &= v_x - u_y. \end{aligned}\right\} \tag{B.10}$$

According to chain rule

$$\left.\begin{aligned}\frac{\partial}{\partial x}&=\frac{\partial}{\partial r}\frac{\partial r}{\partial x}+\frac{\partial}{\partial \xi}\frac{\partial \xi}{\partial x}+\frac{\partial}{\partial \eta}\frac{\partial \eta}{\partial x},\\ \frac{\partial}{\partial y}&=\frac{\partial}{\partial r}\frac{\partial r}{\partial y}+\frac{\partial}{\partial \xi}\frac{\partial \xi}{\partial y}+\frac{\partial}{\partial \eta}\frac{\partial \eta}{\partial y},\\ \frac{\partial}{\partial z}&=\frac{\partial}{\partial r}\frac{\partial r}{\partial z}+\frac{\partial}{\partial \xi}\frac{\partial \xi}{\partial z}+\frac{\partial}{\partial \eta}\frac{\partial \eta}{\partial z},\end{aligned}\right\} \tag{B.11}$$

and

$$\left.\begin{aligned}\frac{\partial r}{\partial x}&=\frac{1}{\sqrt{1+\xi^2+\eta^2}},\\ \frac{\partial r}{\partial y}&=\frac{\xi}{\sqrt{1+\xi^2+\eta^2}},\\ \frac{\partial r}{\partial z}&=\frac{\eta}{\sqrt{1+\xi^2+\eta^2}},\end{aligned}\right\} \tag{B.12}$$

$$\left.\begin{aligned}\frac{\partial \xi}{\partial x}&=\frac{-\xi\sqrt{(1+\xi^2+\eta^2)}}{r},\\ \frac{\partial \xi}{\partial y}&=\frac{\sqrt{(1+\xi^2+\eta^2)}}{r},\\ \frac{\partial \xi}{\partial z}&=0,\end{aligned}\right\} \tag{B.13}$$

$$\left.\begin{aligned}\frac{\partial \eta}{\partial x}&=\frac{-\eta\sqrt{(1+\xi^2+\eta^2)}}{r},\\ \frac{\partial \eta}{\partial y}&=0,\\ \frac{\partial \eta}{\partial z}&=\frac{\sqrt{(1+\xi^2+\eta^2)}}{r},\end{aligned}\right\} \tag{B.14}$$

substituting Eqs. (B.11)-(B.14) into Eq. (B.10), we have:

$$\left.\begin{aligned}\omega_x &= \sqrt{(1+\xi^2+\eta^2)}(w_\xi - v_\eta)/r,\\ \omega_y &= \sqrt{(1+\xi^2+\eta^2)}(u_\eta + \xi w_\xi + \eta w_\eta)/r,\\ \omega_z &= \sqrt{(1+\xi^2+\eta^2)}(u_\xi + \xi v_\xi + \eta v_\eta)/r.\end{aligned}\right\} \tag{B.15}$$

Finally, we get the three components of vorticity vector in conical Coordinates:

$$\left.\begin{aligned}\omega_r &= (\omega_x + \xi\omega_x + \eta\omega_z)/\sqrt{(1+\xi^2+\eta^2)},\\ \omega_\xi &= (1+\eta^2)^{1/2}(-\xi\omega_x + \omega_y)/\sqrt{(1+\xi^2+\eta^2)},\\ \omega_\eta &= (1+\xi^2)^{1/2}(-\eta\omega_x + \omega_z)/\sqrt{(1+\xi^2+\eta^2)}.\end{aligned}\right\} \tag{B.16}$$

Substituting Eq. (B.15) into $\omega_r$ in Eq. (B.16), we get the expression of cross-flow vorticity in conical coordinates:

$$\omega_r = \frac{1}{r}(w_\xi - v_\eta + \xi(u_\eta + \xi w_\xi + \eta w_\eta) - \eta(u_\xi + \xi v_\xi + \eta v_\eta)). \tag{B.17}$$

We will take the cross-flow vorticity as the vorticity to be used to construct the vorticity confinement. Now let's derive the governing equation in conical coordinates. For convenience, the governing equations in Cartesian coordinates are rewritten here:

$$\frac{\partial Q}{\partial t} + \frac{\partial F}{\partial x} + \frac{\partial G}{\partial y} + \frac{\partial G}{\partial z} = S\,, \tag{B.18}$$

where

$$Q=\begin{pmatrix}\rho\\ \rho u\\ \rho v\\ \rho w\\ \rho e_O\end{pmatrix},F=\begin{pmatrix}\rho u\\ \rho u^2+p\\ \rho uv\\ \rho uw\\ \rho uh_0\end{pmatrix},G=\begin{pmatrix}\rho v\\ \rho vu\\ \rho v^2+p\\ \rho vw\\ \rho vh_0\end{pmatrix},H=\begin{pmatrix}\rho w\\ \rho uw\\ \rho vw\\ \rho w^2+p\\ \rho wh_0\end{pmatrix}, \tag{B.19}$$

where $h_0$ is the stagnation enthalpy, p is the pressure, S is the vorticity confinement term. They are defined as follows:

$$\left.\begin{aligned} &h_0=e_0+p/\rho,\\ &p=(\gamma-1)\rho[e_0-(u^2+v^2+w^2)/2],\\ &S=\begin{pmatrix}0\\ \rho\vec{f}_b\cdot\hat{i}\\ \rho\vec{f}_b\cdot\hat{j}\\ \rho\vec{f}_b\cdot\hat{k}\\ \rho\vec{f}_b\cdot\vec{V}\end{pmatrix}, \end{aligned}\right\} \tag{B.20}$$

where $\vec{f}_b$ is the "body force" defined in Chapter 2. Substituting Eqs. (B.11)-(B.14) and applying to F, G and H, we have:

$$\left.\begin{aligned} &\frac{\partial F}{\partial x}=\frac{1}{\kappa}\frac{\partial F}{\partial r}-\frac{\kappa\xi}{r}\frac{\partial F}{\partial\xi}-\frac{\kappa\eta}{r}\frac{\partial F}{\partial\eta},\\ &\frac{\partial G}{\partial y}=\frac{\xi}{\kappa}\frac{\partial G}{\partial r}+\frac{\kappa}{r}\frac{\partial G}{\partial\xi},\\ &\frac{\partial H}{\partial z}=\frac{\eta}{\kappa}\frac{\partial H}{\partial r}+\frac{\kappa}{r}\frac{\partial H}{\partial\eta}. \end{aligned}\right\} \tag{B.21}$$

Substituting Eq. (B.21) into Eq. (B. 18) and simplifying it we have:

$$\frac{r}{\kappa}\frac{\partial Q}{\partial t}+\frac{r}{\kappa^2}\frac{\partial}{\partial r}(F+\xi G+\eta H)+\frac{\partial}{\partial\xi}(G-\xi F)+\frac{\partial}{\partial\eta}(H-\eta F)+2F=\frac{r}{\kappa}S, \tag{B.22}$$

where $\kappa=\sqrt{1+\xi^2+\eta^2}$ . Let's take:

$$\left.\begin{aligned}\tilde{F} &= F + \xi G + \eta H,)\\ \tilde{G} &= G - \xi F,\\ \tilde{H} &= H - \eta F.\end{aligned}\right\} \tag{B.23}$$

Eq. (B.22) can be rewritten as follows:

$$\frac{r}{\kappa}\frac{\partial Q}{\partial t} + \frac{r}{\kappa^2}\frac{\partial \tilde{F}}{\partial r} + \frac{\partial \tilde{G}}{\partial \xi} + \frac{\partial \tilde{H}}{\partial \eta} + 2F = \frac{r}{\kappa}S. \tag{B.24}$$

Applying conical assumption $\frac{\partial}{\partial r} = 0$ to Eq. (B.24), we have:

$$\frac{r}{\kappa}\frac{\partial Q}{\partial t} + \frac{\partial \tilde{G}}{\partial \xi} + \frac{\partial \tilde{H}}{\partial \eta} + 2F = \frac{r}{\kappa}S\,. \tag{B.25}$$

Eq. (B.25) is called governing equations in Conical coordinates, where $\tilde{F}, \tilde{G}, \tilde{H}, F$ are defined as follows:

$$\left.\begin{aligned}\tilde{U} &= u + \xi v + \eta w,\\ \tilde{V} &= v - \xi u,\\ \tilde{W} &= w - \eta u,\end{aligned}\right\} \tag{B.26}$$

$$\tilde{F} = \begin{pmatrix} \rho\tilde{U} \\ \rho u\tilde{U} + p \\ \rho v\tilde{U} + \xi p \\ \rho w\tilde{U} + \eta p \\ \rho\tilde{U}h_0 \end{pmatrix}, \tilde{G} = \begin{pmatrix} \rho\tilde{V} \\ \rho u\tilde{V} - \xi p \\ \rho v\tilde{V} + p \\ \rho w\tilde{V} \\ \rho\tilde{V}h_0 \end{pmatrix}, \tilde{H} = \begin{pmatrix} \rho\tilde{W} \\ \rho u\tilde{W} - \eta p \\ \rho v\tilde{W} \\ \rho w\tilde{W} + p \\ \rho\tilde{W}h_0 \end{pmatrix}, F = \begin{pmatrix} \rho u \\ \rho u^2 + p \\ \rho uv \\ \rho uw \\ \rho uh_0 \end{pmatrix}, \tag{B.27}$$

where the u, v and w are the three components of velocity vector in Cartesian coordinates.

# Appendix C

# Analytical Solution and Initial Condition of a Compressible Moving Vortex with a Uniform Stream

The equation solved in the present study is the unsteady inviscid compressible Euler equations that can be written as follows:

$$\frac{D\vec{V}}{Dt} = -\nabla p / \rho \,, \tag{C.1}$$

where $\rho$ is density, $\vec{V}$ is the velocity vector, and $p$ is pressure. We can develop an equation for vorticity transport by taking the curl of Eq. (C.1) and applying various vector identities. The result is the well-known vorticity transport equation:

$$\frac{D}{Dt}(\frac{\vec{\omega}}{\rho}) = (\frac{\vec{\omega}}{\rho} \cdot \nabla)\vec{V} \,. \tag{C.2}$$

This is a general expression that the quantity $\frac{\vec{\omega}}{\rho}$ is transported along material lines for a compressible isentropic flow.

Next we consider a vortex in a uniform free stream $U_\infty$. Consider an inertial frame with a Cartesian coordinate system $\hat{i}, \hat{j}$ and a cylindrical frame fixed to the vortex core $\hat{i}_r, \hat{i}_\theta$. We expect the vortex to move through the flow at a constant speed $U_\infty$ or

$$\vec{V} = U_\infty \hat{i} + u_\theta \hat{i}_\theta \tag{C.3}$$

and that

$$u_r = 0\,. \tag{C.4}$$

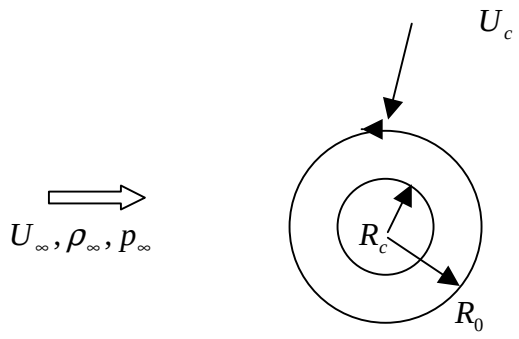


Figure C.1: A compressible vortex moving with a uniform free stream.

We will further model $u_\theta(r)$ as done by Povitsky and Ofengeim [8] as

$$u_\theta(r) = \begin{cases} \tilde{\tilde{U}}_c r / R_c, 0 \le r < R_c \\ \tilde{C}\left(\dfrac{R_0}{r} - \dfrac{r}{R_0}\right), R_c \le r \le R_0 \end{cases}, \tag{C.5}$$

where

$$\left.\begin{aligned} \tilde{\tilde{U}}_c &= U_c / a_\infty \\ \tilde{C} &= \frac{\tilde{\tilde{U}}_c R_0 R_c}{(R_0^2 - R_c^2)} \end{aligned}\right\}, \tag{C.6}$$

where $a_\infty$ is the speed of sound in the free stream. We can determine the appropriate distribution of *p* and $\rho$ as follows:

The momentum equation in $(r,\theta)$ may be written as follows:

$$\left.\begin{aligned}\rho\left(\frac{\partial u_r}{\partial t}+u_r\frac{\partial u_r}{\partial r}+\frac{u_\theta}{r}\frac{\partial u_r}{\partial \theta}-\frac{u_\theta^{\,2}}{r}\right)&=-\frac{\partial p}{\partial r}\\ \rho\left(\frac{\partial u_\theta}{\partial t}+u_r\frac{\partial u_\theta}{\partial r}+\frac{u_\theta}{r}\frac{\partial u_\theta}{\partial \theta}+\frac{u_r u_\theta}{r}\right)&=-\frac{1}{r}\frac{\partial p}{\partial \theta}\end{aligned}\right\}. \tag{C.7}$$

Since $u_r = 0$ and $u_\theta = u_\theta(r)$ we have

$$\left.\begin{aligned}\frac{\partial p}{\partial r}&=\rho\frac{u_\theta^{\,2}}{r}\\ \frac{\partial p}{\partial \theta}&=0\end{aligned}\right\}. \tag{C.8}$$

So $p = p(r)$ and

$$\frac{dp}{dr}=\rho\frac{u_\theta^{\,2}}{r}. \tag{C.9}$$

Since the flow is assumed to be isentropic, $p = c\rho^\gamma$, where c may be evaluated as $p_\infty / \rho_\infty^\gamma = \frac{a_\infty^2}{\gamma\rho_\infty^{\gamma-1}}$, then

$$\frac{dp}{dr}=c\gamma\rho^{\gamma-1}\frac{d\rho}{dr}, \tag{C.10}$$

which gives

$$c\gamma\rho^{\gamma-2}d\rho=\frac{u_\theta^2}{r}dr\,, \tag{C.11}$$

which, using (C.5), may be integrated to yield

$$\rho=\begin{cases}[\rho_{R_c}^{\gamma-1}-\dfrac{(\gamma-1)\tilde{U}_c^{\,2}}{2}(1-(\dfrac{r}{R_c})^2)]^{\frac{1}{\gamma-1}}, 0\le r<R_c\\ [1-(\gamma-1)\tilde{C}^{\frac{2}{\gamma-1}}\{\dfrac{1}{2}(1-(\dfrac{r}{R_0})^2)-2\ln(\dfrac{R_0}{r})-\dfrac{1}{2}(1-(\dfrac{R_0}{r})^2)\}]^{\frac{1}{\gamma-1}}, R_c\le r<R_0\\ 1, r\ge R_0\end{cases}, \tag{C.12}$$

and

$$p=\begin{cases}\dfrac{1}{\gamma}[\rho_{R_c}^{\gamma-1}-\dfrac{(\gamma-1)\tilde{U}_c^{\,2}}{2}(1-(\dfrac{r}{R_c})^2)]^{\frac{\gamma}{\gamma-1}}, 0\le r<R_c\\ \dfrac{1}{\gamma}[1-(\gamma-1)\tilde{C}^{\frac{2\gamma}{\gamma-1}}\{\dfrac{1}{2}(1-(\dfrac{r}{R_0})^2)-2\ln(\dfrac{R_0}{r})-\dfrac{1}{2}(1-(\dfrac{R_0}{r})^2)\}]^{\frac{\gamma}{\gamma-1}}, R_c\le r<R_0\\ \dfrac{1}{\gamma}, r\ge R_0\end{cases}. \tag{C.13}$$

Eqs. (C.5), (C.12) and (C.13) are taken as the initial conditions for the vortex moving in a stream problem. It can be shown that these conditions satisfy compressible continuity, momentum, and energy equations. Hence theses serve as “exact” solutions to the problem.

# Vita

The author, Guangchu Hu, was born on April 26, 1963 in Diang Jiang County, Chong Qing Si, P. R. China. He graduated with a Bachelor's Degree in Physics in 1984 and a Master's Degree in Fluid Mechanical Engineering in 1989 in P. R. China. He began his Ph.D. study at the Aerospace & Ocean Department of Virginia Tech in the fall of 1997. The next 4 years were spent in pursuit of a Doctorate in Aerospace Engineering.